UNIVERSITÀ DI PARMA

# Università degli Studi di Parma

Dottorato di Ricerca in Scienza e Tecnologia dei Materiali

XXXV Ciclo

# *Spectroscopic study of phase transitions and polymorphism in molecular crystals*

**Coordinatore**
Prof. Enrico Dalcanale

**Relatore**
Prof. Matteo Masino

**Dottoranda**
Elena Ferrari

Anni accademici 2019/20 - 2021/2022

# Contents

# Introduction

## 1 Molecular materials

In the last years the interest in molecular materials in the fields of electronics and optics has increased. Firstly, they display uncommon physical properties and exotic phase transitions related to their low dimensionality. Besides, the low temperature solution deposition and the possibility to realize flexible, light weight and potentially biocompatible electronic devices make them also attractive for technology. Nowadays, molecular semiconductors are widely used as light emitters in OLEDs and the research in organic transistors and solar cells is active. Many examples of organic metals, semiconductors and ferroelectrics are known.

However, the carrier mobility and thermal stability still need to be improved. In most systems, the intermolecular interactions are weak and anisotropic and the overlap between the adjacent molecular orbitals is disturbed by lattice vibrations. All these factors favor the localization of the charge carriers. Thus, the control of the crystal packing and the structural order are critical for the applications and are still open issues. Moreover, many organic compounds display polymorphism and the obtained phase and morphology are strongly dependent on the deposition conditions.

These problems can be approached by rational design of the constituent molecules. Indeed, an advantage of molecular systems is their flexibility, i. e. the possibility to tune the molecular shape, the directional interactions and the electron donor/acceptor strength by chemical substitution. By these means, it is often possible to obtain the desired crystal packing and increase the mobility and the stability of the material. To do this, a deep understanding of the effects of crystal packing on the physical properties of the material is required.

In this context, vibrational spectroscopic techniques, as IR and Raman, are powerful tools to characterize molecular materials, in many ways. Firstly, the intramolecular vibrations can be affected by intermolecular interactions. For instance, the charge transfer interaction shifts the vibrational frequencies by changing the bond orders or through the electron-molecular vibration coupling mechanism. Secondly, the lattice phonons are very sensitive to the crystal packing and the structural disorder. The IR and Raman spectra in the THz frequency range, are the fingerprint of a crystal phase and can be used to identify polymorphs and investigate phase transitions. Thirdly, if single crystals are available, different crystallographic planes can be probed separately. Measuring with polarized light, it is possible to distinguish modes having different symmetry. Finally, the combination of Raman and IR provides information on the unit cell symmetry, since the two spectroscopies have different selection rules.

In the present thesis two categories of materials have been investigated: charge transfer cocrystals (Chapters 1-4) and single component semiconductors (Chapters 5-6). The first two chapters expand the well known TTF-haloquinone series with two new systems containing fluoranil (FA) as an acceptor. Both compounds, showing the Neutral to Ionic phase Transition, were characterized at high pressure and low temperature. Chapter 3 presents a new series of CT crystals containing N,N,N',N'-Tetramethylbenzidine (N-TMB) as a donor. Chapter 4 is a detailed spectroscopic study of the analogue system N,N,N',N'-Tetramethylphenylenediamine-TCNQ (TMPD-TCNQ), aimed to clarify its stack symmetry. Chapter 5 is focused on the polymorphism of [6,6]-phenyl-$C_{61}$-butyric acid methyl ester (PCBM), a fullerene derivative widely used in organic photovoltaic cells. Chapter 6 describes the phase transition from crystal to liquid crystal of an high mobility semiconductor, 7-decyl- 2-phenyl[1]benzothieno[3,2-b][1]benzothiophene (Ph- BTBT-10)

# 2 Charge Transfer Cocrystals and the Neutral to Ionic Transition

Organic charge transfer (CT) cocrystals contain planar $\pi$-electron donor (D) and acceptor (A) molecules, arranged in 1D stacks due to the overlap between the frontier orbital of the molecules. This structural motif results in strongly anisotropic optical and electronic properties. For instance, these crystals show a low energy CT absorption polarized along the stack direction. Some typical D and A molecules are shown in Fig 1.

ionicity The most important physical parameter defining these materials is the ionicity $\rho$, that is the average charge localized on D and A molecules. Based on the ionicity value, CT crystals can be Neutral (N) if $\rho < 0.5$ or Ionic (I) otherwise. This depends on the balance between the D ionization energy, the A electron affinity and the Madelung energy due to the 3D Coulomb interactions present in the crystal. Another fundamental parameter is the hopping integral $t$, that reflects the overlap between the D and A frontier orbitals and allows the charge delocalization between the molecules, making intermediate $\rho < 0.5$ values possible. Without it, CT crystals would be either fully N or I.

Mixed or segregated Most CT cocrystals have 1:1 stoichiometry. In this case, the stack can be either segregated or mixed. In the segregated stacks D and A form separate columns, while in the mixed ones D and A molecules alternate along the same stack (Fig 2). This strongly affects their physical properties: while segregated stack crystals might show metallic conductivity [1], mixed stack ones are semiconductors or insulators. In addition, segregated stacks are ionic, while mixed stacks can be either neutral or ionic. Thus, both the ionicity and the preferred stack motif depend on the ionization energy and the symmetry of the frontier orbitals of D and A molecules [2].

Stack symmetry: regular vs dimerized CT crystals can also be classified based on the stack symmetry: the stack can be either regular or dimerized. In the former, the

D-A distances and CT integrals $t$ along the stack are the same, while in the latter two different D-A distances alternate along the stack. In this case D and A molecules no longer lie on symmetry centers. As will be described below, this fact has huge spectroscopic consequences.

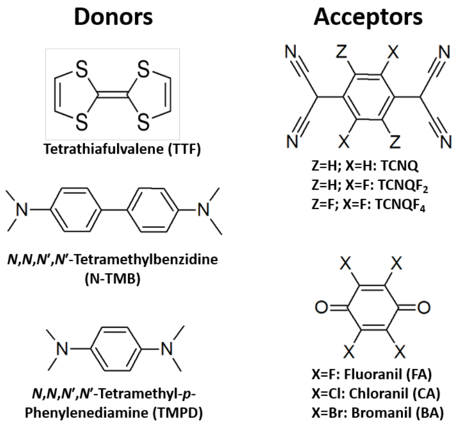

Figure 1: *Typical electron donor and acceptor molecules*

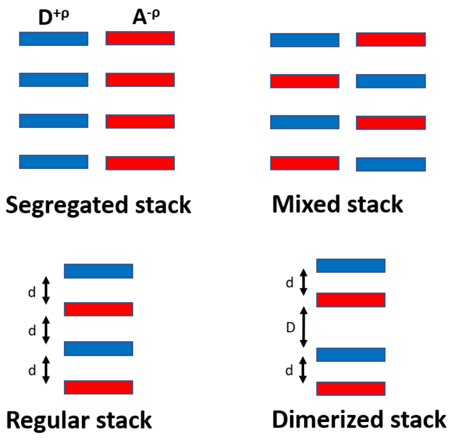

Figure 2: *Stack motifs in CT crystals with 1:1 stoichiometry*

Both the ionicity and the stack symmetry may change under external stimuli, as temperature or pressure. Due to their low dimensionality, CT crystal are affected by Peierls or Spin-Peierls instability, that may induce the dimerization of the stack on cooling down to a certain critical temperature.

A well known example of instability is the Neutral to Ionic phase Transition (NIT), occurring in few mixed stack crystals at high pressure or low temperature [3, 4]. In these conditions, the lattice contraction increases the strength of the 3D Coulomb interactions. This may drive the system from a N ground state to a I one, originating a collective CT called NIT [5]. Since I regular stacks are subject to Peierls instability due to electron-phonon coupling, the ionicity increase is always accompanied by the dimerization of the stack [6, 7]. Thus, the NIT is both a valence and structural instability (Fig 3).

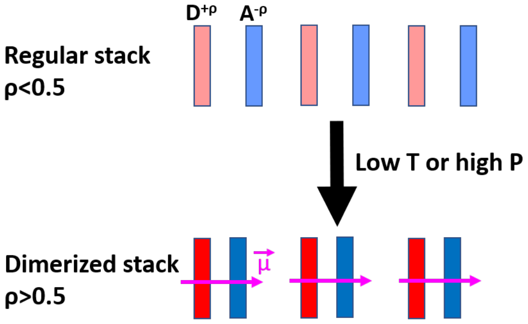

Figure 3: *Schematic representation of the Neutral to Ionic Transition*

The inversion symmetry breaking along the stack direction makes the I phase potentially ferroelectric, as in the case of the prototypical Tetrathiafulvalene-Chloranil (TTF-CA) [3, 4]. Besides, TTF-CA ferroelectricity has an electronic origin, since the polarization is mainly due to intermolecular charge transfer [8]. Further studies on TTF-CA revealed that the same transition can be also photoinduced [9, 10, 11]. Since the first discovery of the NIT [3], other exotic phenomena such as dielectric anomaly [12, 13, 14], soft modes [15, 16], quantum phase transitions [17, 18] have been observed in correspondence with it.

The NIT is characterized by the interplay between two instabilities having different origin: a charge one, due to 3D Coulomb interactions, and a structural one, due to electron-phonon coupling. While the former favors a discontinuous ionicity increase, the latter drives the stack to a continuous symmetry breaking [6, 7, 19]. Thus, depending on these parameters, the NIT can be first or second order. For example, in TTF-CA the electrostatic interactions prevail, leading the system to discontinuous NIT. Differently, in DMTTF-CA, having a bulkier donor, these interactions are weakened and the transition is continuous [20]. Other mixed stack CT crystals undergoing NIT fit well in this scenario [21].

Both the ionicity change and the symmetry breaking show typical spectroscopic signatures and thus can be investigated separately. Briefly, the former affects the vibrational frequencies of D and A, while the latter makes the Raman active totally symmetric modes also IR active. These effects are explained in the following.

Firstly, the ionicity increase makes the neutral D and A molecules similar to their radical ions (Fig 4). Since the partial ionization changes the bond orders, the vibrational modes involving these bonds undergo large frequency shifts. For this reason, they are known as 'charge sensitive modes' [22, 23]. If the frequency shift is linearly correlated to the ionicity, it can be used as a ionicity probe. The most reliable charge sensitive modes are non-totallysymmetric and IR active, polarized in the molecular plane. Thus, they are found in the IR spectra measured with the electric field vector perpendicular to the stack direction.

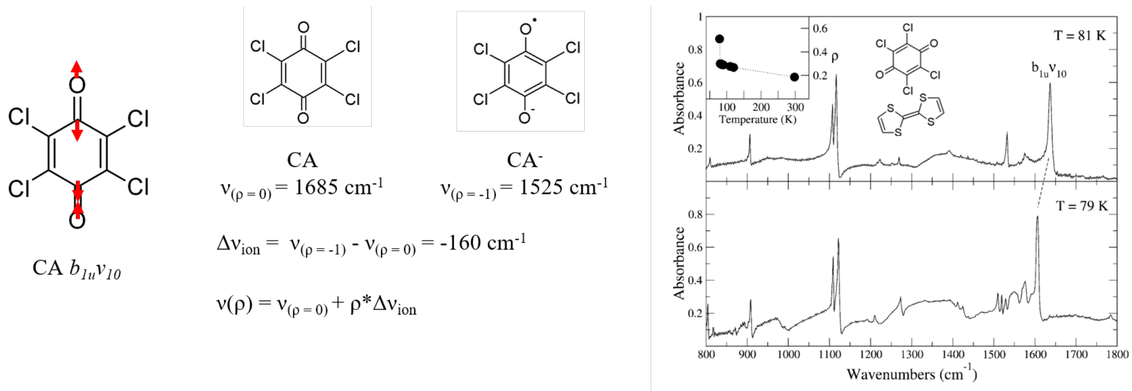

Figure 4: *Left: ionization frequency shift of the CA antisymmetric C=O stretching mode,* $b_{1u}\nu_{10}$. *Right: IR spectra of TTF-CA polarized perpendicular to the stack at 81 (N phase) and 78 K (I phase). Reproduced from [15].*

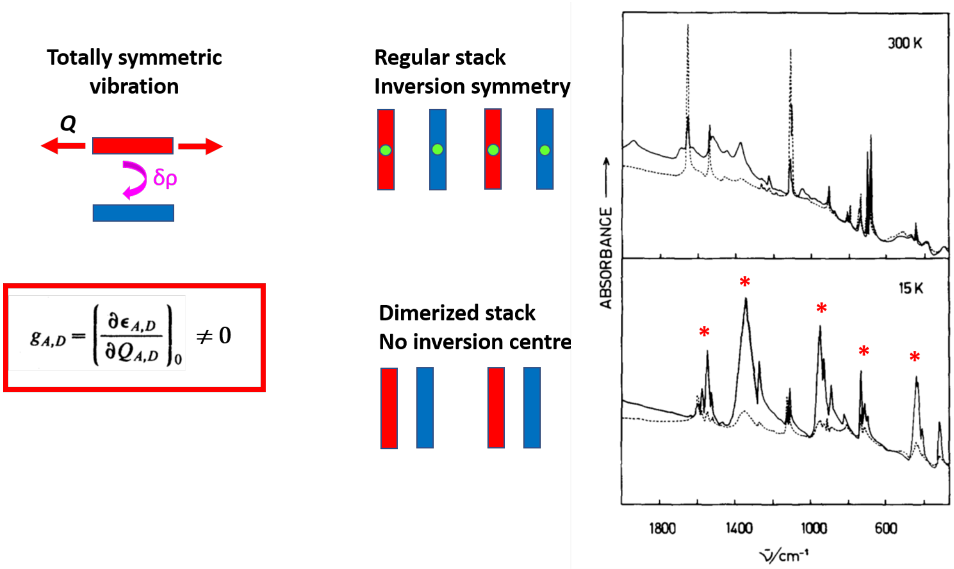

Figure 5: *Left: schematic representation of the e-mv coupling mechanism: the vibration along the normal coordinates* $Q_{A,D}$ *modulates the energies* $\epsilon_{A,D}$ *of the molecular orbitals, inducing charge flows along the stack.* $g_{A,D}$ *is the e-mv coupling constant. Right: polarized IR spectra of TTF-CA at 300 and 15 K. Continuous line: polarization along the stack. The strong bands occurring at low T indicate the stack dimerization in the I phase. Reproduced from [24].*

Also the stack dimerization has huge spectroscopic consequences, due to the coupling between the intramolecular vibrations and the CT electron (e-mv coupling) [25, 26, 27]. This means that certain vibrations, i.e. the totally symmetric ones, induce charge flows along the stack, modulating the energies of the frontier orbitals involved in the CT interaction (Fig 5). If the inversion symmetry of the stack is broken, these charge flows are associated with electric dipoles oscillating along the stack direction. Consequently, the totally symmetric modes, Raman active, become also IR active, with huge intensity and polarized along the stack. Thus, in dimerized stacks the IR and Raman spectra show the same peaks. Another effect of the e-mv coupling is the frequency lowering of the coupled modes. Therefore, the totally symmetric modes are not used as ionicity indicators.

But that is not all. Vibrational spectroscopy is also able to provide information on the symmetry and multiplicity of the unit cell and on the electron-lattice phonon coupling. These issues will be discussed in the following chapters, focused on the NIT.

# Chapter 1

# TTF-Fluoranil rediscovered: Temperature and Pressure Induced Neutral to Ionic Transition

## 1.1 Introduction

Tetrathiafulvalene-Fluoranil (TTF-FA) was synthesized for the first time in 1979 [2], together with TTF-CA, before the discovery of the NIT [3]. Since then, the effects of chemical substitution on the NIT have been extensively studied by modification of TTF and CA molecules [28, 29]. However, TTF-FA was missing in this TTF-Haloquinone series, having been elusive until now. Probably due to its instability, it has never been experimentally reproduced.

We firstly prepared TTF-FA as a powder by grinding the pure components. Then, thanks to a kinetic control of the crystal growth by a rapid evaporation of the solvent, we were able to obtain good quality TTF-FA single crystals. We found that TTF-FA presents both temperature [30] and pressure induced NIT. Both neutral and ionic phases were fully characterized by IR, Raman and X-ray diffraction. The transition is strongly first order, associated with a ionicity jump, the stack dimerization and the doubling of the unit cell in the ionic phase. The crystal breaking at the transition made the investigation difficult.

## 1.2 Experimental

### 1.2.1 Synthesis

TTF-FA powders were prepared by grinding 10.63 mg of TTF ($5.2*10^{-4}$ mol) and 9.37 mg of FA ($5.2*10^{-4}$ mol) in an agate mortar for 20 minutes. The powder turned to brown after grinding for 3 minutes.

The following attempts to crystallize TTF-FA with slow methods always yielded a red-brown amorphous product. Good quality single crystals were finally obtained by mixing saturated toluene solutions of the two components in 1:1 stochiometric ratio and rapidly evaporating the solvent. The solution mixing resulted in a color change from yellow to green due to the complex formation. The crystals, green and needle shaped, grew mainly at the edge of the evaporating solution. The crystals, unstable at room temperature due to FA sublimation, were stored at low temperature.

### 1.2.2 Structure determination

XRD measurements were performed in Parma by Prof Francesco Mezzadri. Single crystal X-rays diffraction was collected at RT by using graphite monochromatized Mo K$\alpha$ wavelength on a Bruker Smart diffractometer equipped with an APEX II CCD detector. Low temperature data were collected with a Bruker D8 Venture instrument, equipped with a Photon II CCD area detector and micro-focused Mo K$\alpha$ radiation source. Temperature control was achieved with an Oxford cryostream system working in nitrogen flux. Due to crystal breaking at the NIT transition, the low temperature data collection required the sample to be placed into a glass capillary filled with Fomblin®, a perfluorinated polymer that increases its viscosity as temperature is lowered. In such a way crystal cracking was avoided without inhibiting the transition. The single crystals data reduction was carried out by using the SADABS program [31] The software Shelxt was used for structures solution while refinement was carried out full-matrix by using the Shelxl program [32].

### 1.2.3 Spectroscopic measurements

The IR spectra were recorded with a Bruker IFS-66 FT-IR spectrometer coupled to a Hyperion 1000 IR microscope, on the *ac* and on the *ab* face with the electric field vector polarized parallel or perpendicular to the stack direction *a*. The crystal faces were previously indexed by XRD. The measurements were performed mainly in absorbance mode on the thinnest crystals, using KBr as a reference. Some spectra were measured in reflectance mode on thicker crystals having a good quality surface, using a metallic mirror as a reference.

The Raman spectra were recorded with a Renishaw 1000 spectrometer equipped with the appropriate edge filter and coupled to a Leica M microscope using the 568.2 nm line of a Lexel Kr laser. Low frequency spectra have been acquired using a Horiba LabRAM HR Evolution Raman spectrometer, equipped with a 633 nm HeNe laser and a ULF Bragg filter to reject the Rayleigh scattered radiation. The diffraction grating with 1800 grooves/mm allowed for a maximum spectral resolution of 0.3 cm$^{-1}$ and a lowest accessible frequency of 4 cm$^{-1}$ . The laser power was always set below 0.1 mW to avoid sample heating. Raman spectra were measured with the exciting and scattered light polarized parallel or perpendicular to the stack on both *ac* and *ab* crystal faces.

The crystals were cooled down to 80 K using a Linkam HFS 91 stage and were fixed to it to prevent sample disintegration during the phase transition. In the case of Raman measurements, the crystals were pasted to the stage with a conductive silver paste, while they were covered with a thin and flat KBr slide for transmission IR measurements.

For the high pressure measurements, the samples were placed in a diamond anvil cell (DAC), shown in Fig 1.1, using brass gasket to allow a finer pressure tuning in the range 0.1-1.5 GPa. The hole containing the sample was filled with Nujol oil, used as pressure transmitting medium. The DAC was fitted under both IR and Raman microscopes. In the case of Raman a 20x magnification objective was used, as its working distance was suitable to focus the laser beam on the sample inside the cell. The pressure was measured with the ruby fluorescence method (1.1) [33]. To increase the wavelength accuracy, the spectrum of a Ne calibration lamp was acquired together with the ruby fluorescence without moving the grating (pressure error 0.05 GPa). Measurements performed on rubies located in different positions of the hole confirmed the pressure homogeneity. Two different crystals were used: a thick sample was used mainly for Raman measurements while a thinner one was chosen for IR. Both crystals lie on the *ab* face.

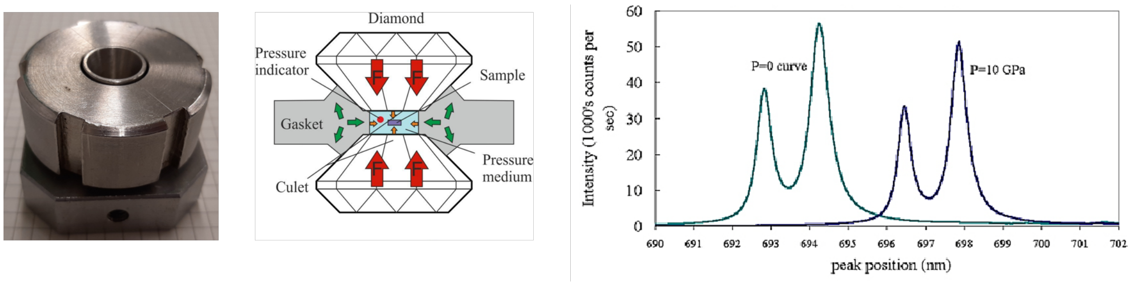

Figure 1.1: *Left: the cell used for the high pressure measurements. Center: scheme of the DAC. Right: pressure shift of the ruby fluorescence band.*

### 1.2.4 Calculations

Standard DFT computational methods (B3LYP, 6-31G(d)) were exploited for the calculation of equilibrium geometry and vibrational frequencies of the constituent molecules, in both the neutral and ionized state, using Gaussian 16 B.10 [34]. The frequencies higher than 1000 cm$^{-1}$ were scaled by the factor 0.9613, as suggested in [35]. First principles calculations following the approach described in [21] have been performed on the crystal structures to estimate the tendency towards valence instability.

## 1.3 Results

### 1.3.1 Crystal growth

At first, TTF-FA was obtained as powder by grinding the pure components. The identity of the product was later confirmed by IR spectroscopy: the spectra of the powdered TTF-FA crystals and the ground powder are the same (Fig 1.2). However,the brownish colour of the ground powder proves that it also contains the byproduct found in many crystal growth attempts.

The fact that TTF-FA crystals could be obtained only by rapid solvent evaporation and using saturated solutions indicates that the crystal growth is kinetically controlled. The key factors of this unusually fast growth method are the high solubility of both pure components ($\simeq 1M$) and CT complex. This allows to grow large crystals by dissolving a high amount of starting material without precipitation.

The green colour of the mother solution suggests that TTF-FA complex is formed firstly in solution. However, Raman measurements on the mixed toluene solution demonstrated that a large fraction of TTF and FA molecules were isolated. Thus, the CT complex must be very weak. It was not possible to measure the absorption spectrum of the mother solution due to the high concentration.

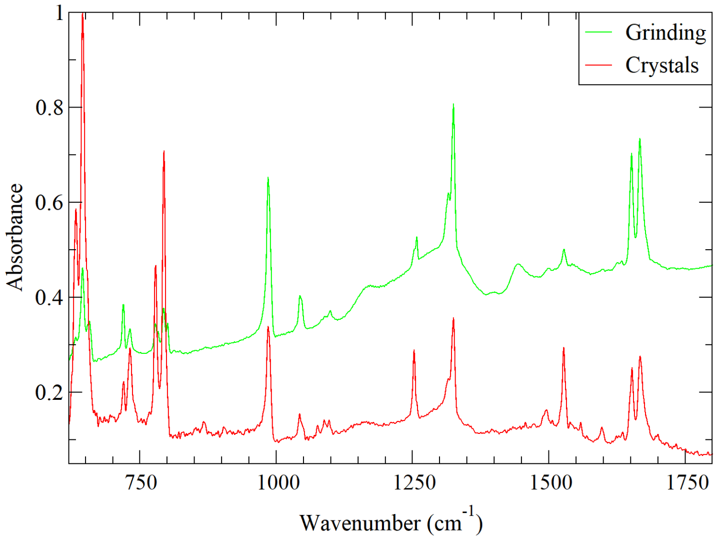

Figure 1.2: *IR spectrum of TTF-FA obtained by grinding (green line) and of powdered TTF-FA crystals (red line). The spectra are upshifted for clarity.*

## 1.3.2 Relationship between morphology and spectra

### The neutral phase

Single crystal XRD analysis confirmed the triclinic ($P-1$) structure found by Torrance et al. [2], characterized by a mixed regular stack, with TTF and FA molecules alternating along $a$ and laying on the inversion centers.

The green and needle-shaped TTF-FA crystals (Fig 1.3) are elongated in the stack direction and usually show two different faces, parallel to the $ac$ and $ab$ planes (Fig 1.4). The stack direction can be easily recognized by optical spectroscopy due to the presence of the CT excitation, occurring at around 6000 cm$^{-1}$ (Fig 1.5). The needle-like crystal shape reflects the strong and directional CT interaction, that is the main intermolecular force and drives a faster crystal growth along the stack direction. Also the out-of-plane antisymmetric modes of the two molecules are mainly polarized in this direction. Differently, the in-plane antisymmetric modes can be observed in the spectra polarized perpendicular to the stack. Since in a first approximation the $D_{2h}$ point group of the TTF and FA molecules is retained in the crystal, these vibrations, polarized along the two in-plane molecular axes, have $b_{1u}$ and $b_{2u}$ symmetry. While the spectra recorded on the $ab$ face are dominated by the FA $b_{2u}$ bands, the spectra recorded on the $ac$ face show mainly the $b_{1u}$ vibrations and a small projection of $b_{2u}$ ones (see Fig 1.4 and Fig 1.6). The complete assignment of the IR spectra is reported in Table 1.1.

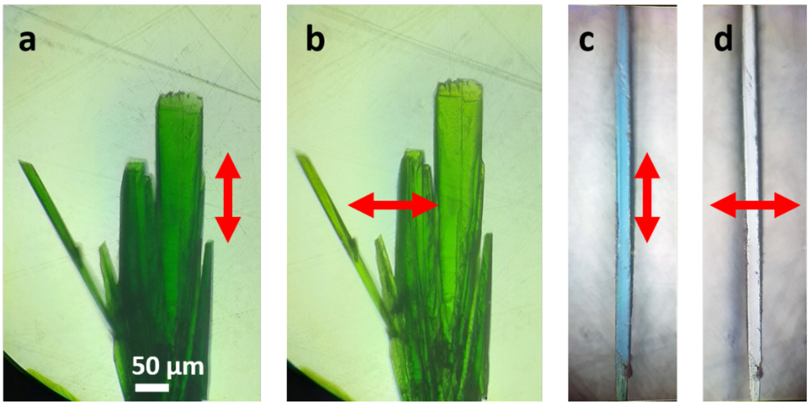

Figure 1.3: *Microscopic images of TTF-FA crystals (unknown face). Polarized transmitted light parallel (a) and perpendicular (b) to the stack axis. Polarized reflected light parallel (c) and perpendicular (d) to the stack axis.*

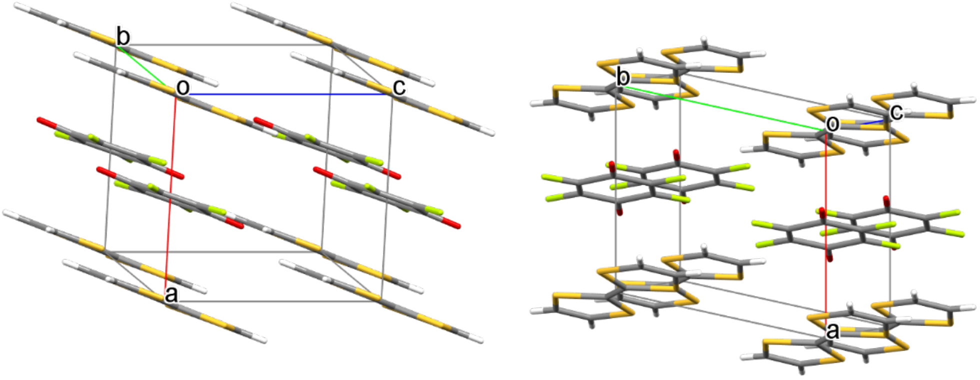

Figure 1.4: *Crystal structure of TTF-FA at room temperature, viewed along the [010] (left) and [001] (right) directions. The spectra have been recorded on these two faces. The C=O* $b_{1u}\nu_{10}$ *mode can be excited in the ac-face only.*

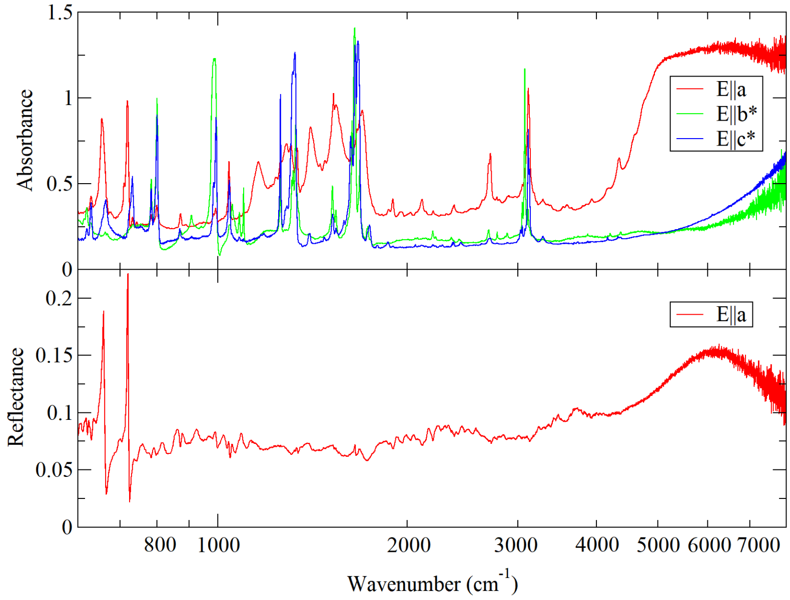

Figure 1.5: *Comparison between the polarized IR spectra of TTF-FA (red, green and blue) and the unpolarized spectra of thin films of TTF (orange) and FA (black).*

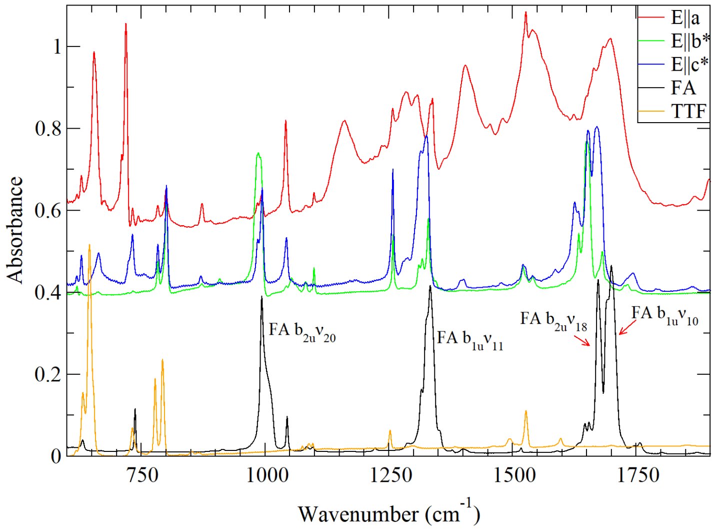

Figure 1.6: *Comparison between the polarized IR spectra of TTF-FA (red, green and blue) and the unpolarized spectra of TTF (orange) and FA (black).*

### The Phase Transition

TTF-FA crystals undergo a temperature induced first order NIT, associated with sudden sample breaking and colour change from green to brown. Fixing the crystal, we observed that the transition front propagates by jumps along the stack direction $a$, with the appearance of many parallel cracks.

During the first cooling the transition temperature is not well defined and varies in the range 120-160 K depending on the sample history and cooling rate. Also the substrates used for the measurements may affect the transition temperature or, sometimes, inhibit the transition. Indeed, the spectra recorded on different points of the same crystal sometimes reveal the coexistence of the two phases, as observed in other discontinuous NITs [36].

The transition is reversible with a large thermal hysteresis, with the ionic to neutral (I-N) transformation taking place at 200 K on heating and the N-I one at 170 K on cooling again, in a reproducible way. The optical axes and the polarization direction of the CT excitation are unchanged by the transition.

### 1.3.3 Ionicity

The NIT is characterized by two order parameters: the ionicity and the stack dimerization. The degree of charge transfer can be obtained from the frequency shifts of some selected "charge sensitive modes" [23] of the constituent molecules. The best choice are the FA C=O and C=C stretching bands, named $b_{1u}\nu_{10}$ and $b_{2u}\nu_{18}$ respectively, found in the IR spectra polarized perpendicular to the stack.

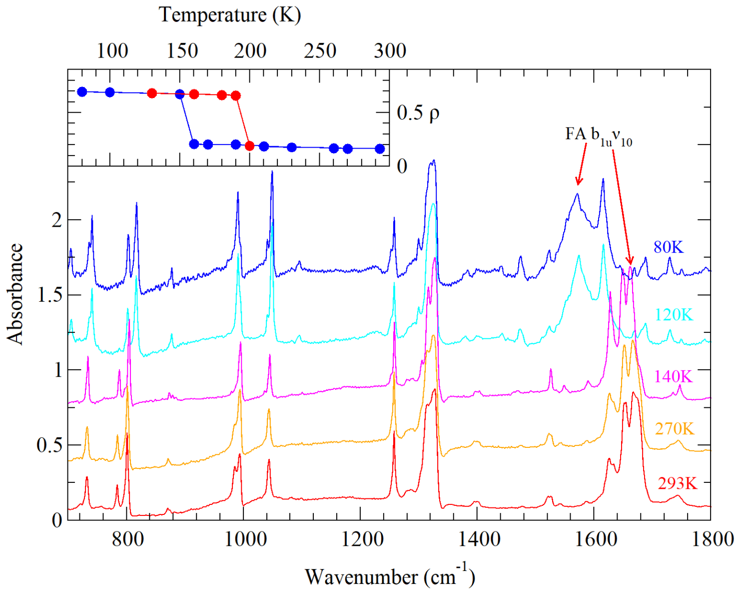

Figure 1.7: *Temperature evolution of the IR spectra of TTF-FA, recorded on ac face with the electric field polarized perpendicular to the stack. The spectra are upshifted for clarity. Inset: Ionicity changes of TTF-FA estimated from the FA* $b_{1u}\nu_{10}$ *frequency: first cooling (blue) and heating (red).*

In the spectrum of the high temperature phase these bands are redshifted compared to the same bands of the pure compound, as expected [37]. Indeed, passing

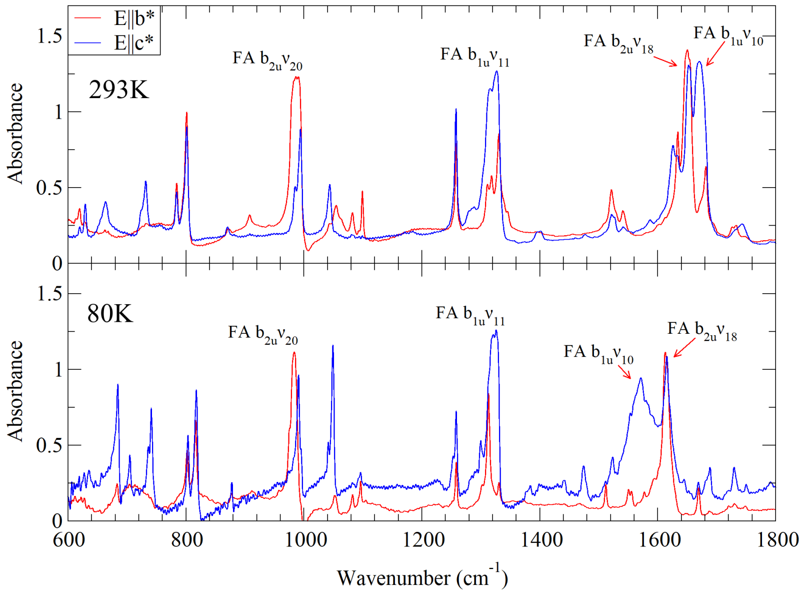

Figure 1.8: *IR spectra of the N (upper panel) and I phases (lower panel) of TTF-FA, measured on the ab and ac faces with the electric field polarized perpendicular to the stack direction a.*

from haloquinone neutral molecules to their radical anions, these double bonds acquire partially single bond character and for this reason their stretching frequencies are strongly lowered (see Introduction, Fig 4) [22]. Furthermore, their frequency shifts are known to show a linear behavior, making both modes good ionicity probes: $b_{1u}\nu_{10}$ in the whole ionicity range and $b_{2u}\nu_{18}$ for neutral ($\rho < 0.5$) compounds only [23]. In the case of FA the ionization frequency shifts were estimated through DFT calculations due to the lack of experimental data on FA anion. According to the calculations, $b_{1u}\nu_{10}$ and $b_{2u}\nu_{18}$ are redshifted 184 and 117 cm$^{-1}$ , respectively (Table 1.2). The $b_{1u}\nu_{10}$ full ionicity frequency shift is consistent with that of other haloquinones, which is 160 cm$^{-1}$ for both chloranil and bromanil [22]. At room temperature $b_{1u}\nu_{10}$ and $b_{2u}\nu_{18}$ occur at 1670 and 1651 cm$^{-1}$ , indicating that TTF-FA is on the neutral side with a degree of charge transfer of 0.15. Also the frequency shifts of other selected TTF charge sensitive modes [38], $b_{1u}\nu_{14}$, $b_{1u}\nu_{16}$ and $b_{3u}\nu_{34}$ (Table 1.3), yielding values in the range 0.1-0.3, confirm the above estimate.

After the phase transition all the charge sensitive bands of TTF and FA shift, showing a large ionicity increase (Fig 1.7). In particular, the two strong bands observed at 1572 and 1616 cm$^{-1}$ can be assigned to FA $b_{1u}\nu_{10}$ and $b_{2u}\nu_{18}$, respectively. Indeed, the former band is present only in the spectrum recorded on the *ac* face, while the latter is found in the spectra of both *ac* and *ab* faces, as for the high temperature phase (Fig 1.8). The $b_{1u}\nu_{10}$ frequency corresponds to a ionicity value of 0.7, showing that TTF-FA crosses the neutral-ionic borderline at the transition. The temperature evolution of $\rho$ estimated from the $b_{1u}\nu_{10}$ mode, shown in the inset of Fig 1.7, is strongly discontinuous in both phases, even close to the transition.

Table 1.1: *Band assignment of TTF-FA polarized IR spectra, at 293 and 80 K. Par is referred to a axis, parallel to the stack, while Perp is referred to b* and c*. All the frequencies are in* $cm^{-1}$ *.*

| Perp 293K | Perp 80K | Par 293K | Par 80K | Assignment |
|---|---|---|---|---|
| | 685 | 657 | 685 | TTF, $b_{3u}\nu_{34}$ |
| | | | 735 | TTF, $a_g\nu_5$ |
| | | 720 | 705 | FA, $b_{3u}\nu_{28}$ |
| 732 | 739 | 732 | | TTF, $b_{1u}\nu_{17}$ |
| 785 | 803 | 785 | 803 | TTF, $b_{1u}\nu_{16}$ |
| 801 | 817 | 801 | 817 | TTF, $b_{2u}\nu_{25}$ |
| 908 | | | | TTF, $b_{2u}\nu_{24}$ |
| 985 | 985 | | | FA, $b_{2u}\nu_{20}$ |
| 1045 | 1049 | 1042 | 1029 | FA, $b_{1u}\nu_{12}$ |
| 1099 | 1097 | 1099 | | TTF, $b_{1u}\nu_{15}$ |
| | | ≃1158 | | sideband |
| | | | 1180 | FA, $a_g\nu_3$ |
| 1258 | 1258 | | | TTF, $b_{2u}\nu_{23}$ |
| | | ≃1283 | | sideband |
| 1318 | 1311 | | | FA, $b_{2u}\nu_{19}$ |
| 1327 | 1325 | 1334 | | FA, $b_{1u}\nu_{11}$ |
| | | | 1390 | TTF, $a_g\nu_3$ |
| | | ≃1403 | | sideband |
| 1527 | 1478 | 1527 | 1478 | TTF, $b_{1u}\nu_{14}$ |
| | | | 1521 | TTF, $a_g\nu_2$? |
| | | ≃1542 | | sideband[1] |
| | | | 1550 | FA, $a_g\nu_1$ |
| | | | 1597 | FA, $a_g\nu_2$ |
| 1651 | 1616 | | | FA, $b_{2u}\nu_{18}$ |
| 1670 | 1572 | | | FA, $b_{1u}\nu_{10}$ |
| | | | 1666 | ? |
| | | | 1686 | ? |
| | | ≃1692 | | sideband |
| 3074 | | | | TTF, $b_{2u}\nu_{22}$ |
| 3114 | | 3114 | | TTF, $b_{1u}\nu_{13}$ |

[1] The band at 1542 $cm^{-1}$ is the right sideband of TTF $a_g\nu_3$ and hides the left sideband of FA $a_g\nu_1$. This band should be centered around 1575 $cm^{-1}$ , assuming the effective Peierls mode frequency to be 65 $cm^{-1}$ . The two sidebands separate on lowering temperature due to the softening of the Peierls mode (Fig 1.9).

In the case of TTF, the antisymmetric C=C stretching band is shifted to 1478 $cm^{-1}$ , as in the completely ionized molecules ($\rho = 1$). However, the other charge sensitive modes indicate a lower degree of charge transfer (0.6 for $b_{3u}\nu_{34}$ and 0.4 for $b_{1u}\nu_{16}$).

The frequency shifts of two Raman active TTF totally symmetric modes, $a_g\nu_2$ and

$\nu_3$, yield a ionicity value of 0.6-0.7, if the effects of e-mv coupling are considered [26, 5], assuming the CT transition frequency to be 6000 cm$^{-1}$ as in the neutral phase. The small discrepancies between the TTF IR bands are probably due to the deformation of the molecules in the ionic phase, as described in Section 1.3.6.

Table 1.2: *Assignment of some selected modes of FA in TTF-FA N and I phases. The frequencies are in cm$^{-1}$ and the calculated values have been scaled.*

| Mode | FA<br>expt (calc) | TTF-FA 293K | TTF-FA 80K | FA$^-$<br>(calc) |
|---|---|---|---|---|
| $a_g\nu_1$ | 1704 (1709) | 1642 | 1547 | (1545) |
| $a_g\nu_3$ | 1251 (1290) | 1233 | 1170 | (1269) |
| $b_{1u}\nu_{10}$ | 1700 (1704) | 1670 | 1572 | (1520) |
| $b_{2u}\nu_{18}$ | 1669 (1649) | 1651 | 1616 | (1532) |

Table 1.3: *Assignment of some selected modes of TTF in TTF-FA N and I phases. The frequencies are in cm$^{-1}$ and the calculated values have been scaled.*

| Mode | TTF<br>expt(calc) | TTF-FA 293K | TTF-FA 80K | TTF$^+$<br>expt(calc) |
|---|---|---|---|---|
| $a_g\nu_2$ | 1555(1582) | 1540 | 1522 | 1505(1511) |
| $a_g\nu_3$ | 1518(1538) | 1475 | 1384 | 1420(1393) |
| $b_{1u}\nu_{14}$ | 1530(1560) | 1527 | 1478 | 1478(1492) |
| $b_{1u}\nu_{16}$ | 781 (782) | 785 | 803 | 836 (831) |
| $b_{3u}\nu_{34}$ | 639 (654) | 657 | 680 | 705 (709) |

### 1.3.4 Stack dimerization

While the IR spectrum polarized perpendicular to the stack gives information on the ionicity, the parallel polarized one reflects the stack symmetry, being affected by vibronic effects [25, 26]. In the spectrum of the neutral phase (Fig 1.10, upper panel) the absence of vibronic activation of the totally symmetric modes demonstrates that the stack is regular, with both molecules laying on inversion centers. However, some strong and broad IR absorptions are found at the same distance, about 65 cm$^{-1}$ , from the most strongly coupled totally symmetric modes, i.e. TTF $a_g\nu_3$ and FA $a_g\nu_1$ and $\nu_2$. Similar features were observed in the IR spectra of the centrosymmetric neutral phase of TTF-CA [15]. They are the so-called sidebands, two phonon excitations due to sum and difference combinations between the totally symmetric intramolecular vibrations and an effective Peierls phonon, the lattice mode that drives the stack dimerization. Since such phonon is IR active and polarized along the stack, its combinations with the totally symmetric vibrations have the same polarization. As in the case of TTF-CA, all three pairs of sidebands shift towards the corresponding totally symmetric bands on lowering temperature (Fig 1.9). This evolution reflects the softening of the Peierls mode that remains incomplete, interrupted by the discontinuous transition.

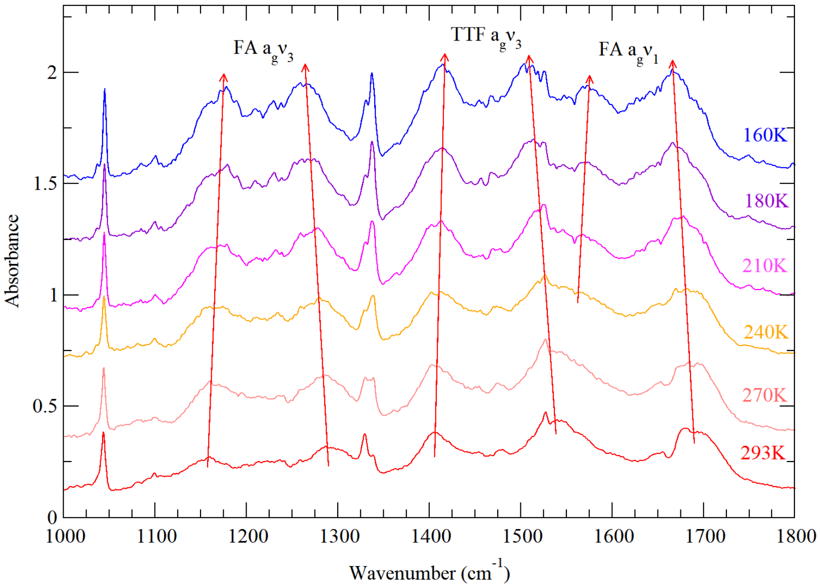

Figure 1.9: *Temperature evolution of the sidebands in the IR spectrum polarized parallel to the stack. The corresponding totally symmetric mode of each pair of sidebands is indicated at the top. The spectra are upshifted for clarity.*

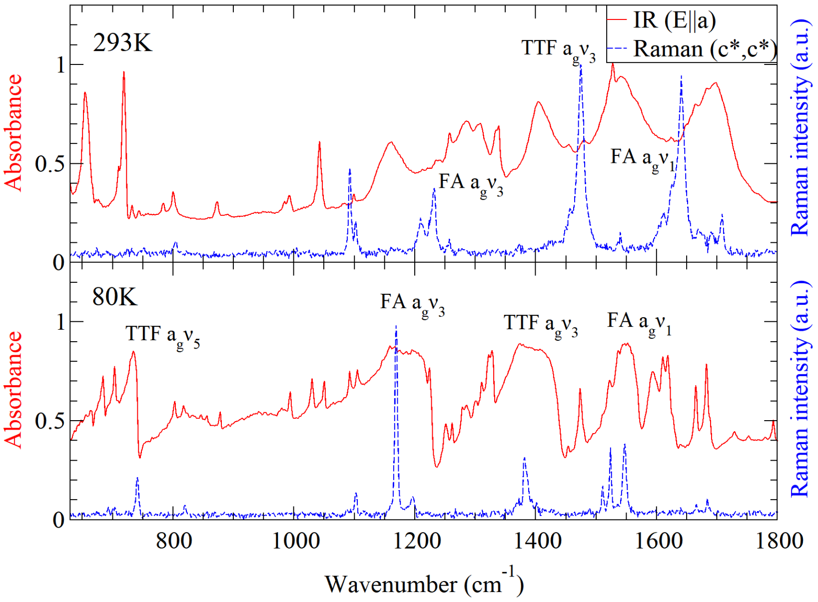

Figure 1.10: *Comparison of TTF-FA parallel polarized IR spectrum and Raman spectrum recorded on ac face with both exciting and scattered light polarized perpendicular to the stack, at 293 K (upper panel) and 80 K (lower panel).* $\lambda_{exc}$= *568.2 nm*

### 1.3.5 Lattice phonons

Some information on the stack symmetry and on specific lattice vibrations, such as the effective Peierls mode, have been obtained from the parallel polarized IR spectra in the range of the intramolecular vibrations thanks to vibronic effects. A deeper insight on lattice symmetry can be achieved by direct Raman observation of the lattice vibrations in the range 5-200 cm$^{-1}$ . These spectra are very sensitive to crystal packing and the number of Raman active intermolecular vibrations can provide information on the symmetry and multiplicity of the unit cell.

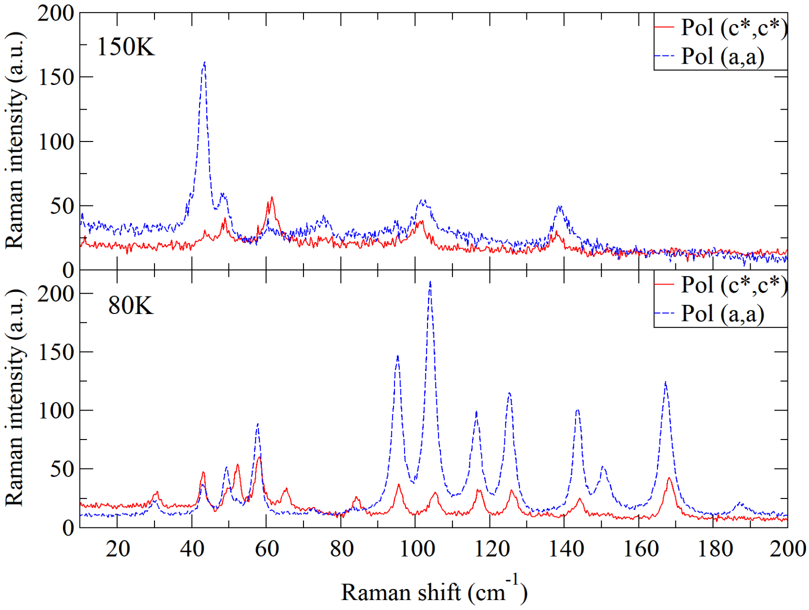

Figure 1.11: *Low frequency Raman spectra of TTF-FA N- (upper panel) and I- phases (lower panel), recorded on ac face. The polarization of exciting and scattered light is the same: perpendicular (red continuous line) or parallel (blue dashed line) to the stack. The relative magnitudes of all the spectra reflect the intensity of the light scattered by the sample (the parallel polarized* $(a, a)$ *spectrum of the I-phase has been scaled by a factor of 3 for clarity).* $\lambda_{exc}$= *633 nm*

In the case of the neutral phase, the $P-1$ unit cell contains one D-A pair and both molecules occupy sites with $C_i$ symmetry. Consequently, 9 optically active lattice phonons are expected. Since the mutual exclusion rule holds, the six rotations should be Raman active while the three translations IR active. In fact, the low frequency Raman spectra of the neutral phase show six bands (Fig 1.11, upper panel). Both the polarizations reported here (spectra recorded on *ac* face) share the same bands with different relative intensities. The other polarizations do not add relevant information.

The phase transition is revealed by the appearance of many new bands and by the intensity enhancement of the $(a; a)$ polarized spectrum, in particular in the range 80-170 cm$^{-1}$ (Fig 1.11, lower panel), due to the activation of translational modes coupled to the CT excitations. This spectrum shows 12 bands, most of which are in common with the $(c^*, c^*)$ polarization. Overall, 15 different bands can be distinguished in the spectral range 0-180 cm$^{-1}$ . Differently, in the $(b^*, b^*)$ polarization the majority of these bands are very weak (Fig 1.12), suggesting the occurrence of cell doubling along the $c$-axis. If a triclinic unit cell is doubled, the arrangement of the two adjacent dimerized stacks can be either ferrielectric, when the stacks are inequivalent, or antiferroelectric if the stacks are equivalent and related by inversion symmetry. In both cases 21 optically active phonons are expected, but the number of Raman active ones is different in each situation. In the former case all the phonons would be both IR and Raman active due to the lack of inversion symmetry. Differently, in the latter case, due to the presence of inversion center situated between the chains, the mutual exclusion rule would be still valid and only 12 Raman active phonons (6 rotations and 6 translations) are predicted.

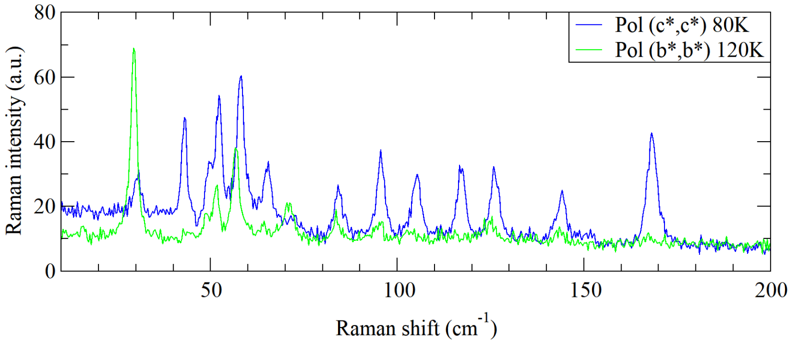

Figure 1.12: *Low frequency Raman spectra of TTF-FA ionic phase, recorded with both exciting and scattered light polarized perpendicular to the stack, on ac (blue) and ab (green) faces. Some bands are slightly shifted as the two spectra were recorded at different temperatures.* $\lambda_{exc}$= *633 nm*

Considering the fact that at 80 K the increased resolution due to band narrowing makes the weakest bands detectable, the ferrielectric arrangement is unlikely. In fact, both TTF and FA have low frequency intramolecular vibrations [37, 38]. All of them might be Raman active due to the symmetry lowering of the molecule in the crystal. In these circumstances, in absence of a symmetry center more than 21 Raman bands are expected, in disagreement with the 15 ones observed. Finally, also the absence of splitting of all the charge sensitive bands in the I phase indicates that the ionicity is the same for all the D and A molecules, suggesting the equivalence of the two stacks.

### 1.3.6 Crystal structure of the ionic phase

The X-ray investigation of the I phase was a difficult task due to the crystal cracking. Luckily, in this case immersing the crystal into viscous fluids did not inhibit the transition [39]. X-ray diffraction clearly indicates a change of the lattice parameters in the I phase(Table 1.4).

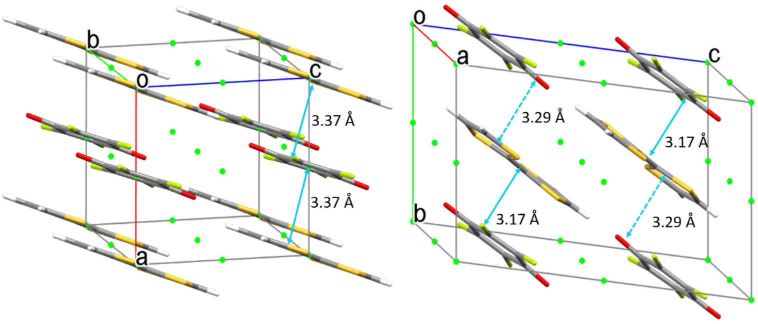

Figure 1.13: *Crystal structures of TTF-FA at 293 K (left) and 120 K (right), viewed perpendicular to ac plane (referred to the N phase). The inversion centers are marked in green. Intra- and inter-dimer D-A distances (molecular plane to centroid) are reported.*

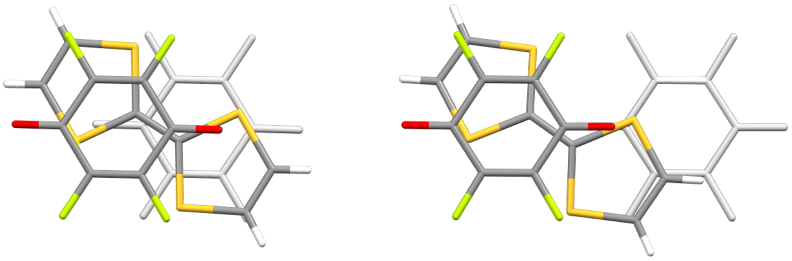

Figure 1.14: *D-A overlap in TTF-FA N (left) and I phases (right). The FA molecule in the background is colored in light grey. View perpendicular to FA molecular plane.*

Table 1.4: *Structural parameters of N and I phases of TTF-FA. Respect to the spatial arrangement of the molecules, the a and b axes of the N phase respectively correspond to the b and a axes of the I phase, due to a crystallographic convention.*

| | Neutral phase (293K) | Ionic phase (120K) |
|---|---|---|
| Crystal system | Triclinic | Triclinic |
| Space group | $P-1$ | $P-1$ |
| $a$ (Å) | 7.054(5) | 7.2023(2) |
| $b$ (Å) | 7.304(6) | 7.8625(3) |
| $c$ (Å) | 7.359(5) | 12.6272(4) |
| $\alpha$(deg) | 106.150(12) | 83.040(2) |
| $\beta$(deg) | 93.101(14) | 73.7170(10) |
| $\gamma$(deg) | 102.419(14) | 77.224(2) |
| Z | 1 | 2 |
| V (Å$^3$) | 353.0(5) | 668.04(4) |
| R1 | 0.040 | 0.033 |

Structure refinement in $P-1$ space group gave R1 agreement factor of 0.033. No relevant improvement was observed in the $P1$ symmetry, despite doubling of the parameters. As a consequence, the centrosymmetric solution was chosen. Respect to the spatial arrangement of the molecules, the $a$ and $b$ axes of the neutral phase approximately correspond to the $b$ and $a$ axes of the ionic phase, respectively, while the $c$ direction is unchanged. In the following, all the axis labels are referred to the neutral phase.

The ionic phase is characterized by the doubling of the unit cell along the $c$-axis, with two equivalent stacks, strongly dimerized and related by inversion symmetry in an antiferroelectric arrangement (Fig 1.13, right). The intradimer and interdimer distances (plane-centroid) are 3.17 and 3.29 Å, respectively. The intradimer relative orientation of TTF and FA is similar to that observed in the neutral phase. Differently, the interdimer interaction is reduced as the dimers are shifted respect to each other approximately along the $c$-axis, as shown in Fig 1.14.

Therefore, the interdimer and intradimer charge transfer integrals ($t_1$ and $t_2$) become 0.41 and 0.16 eV respectively, starting from $t$=0.32 eV in the N phase. Thus, the dimerization degree, calculated as $(t_1 - t_2)/(t_1 + t_2)$, is 0.44, much higher than the 0.24 value found in the TTF-CA I phase. These values have been calculated using the corresponding DA pairs extracted from the corresponding crystal structures [40, 21].

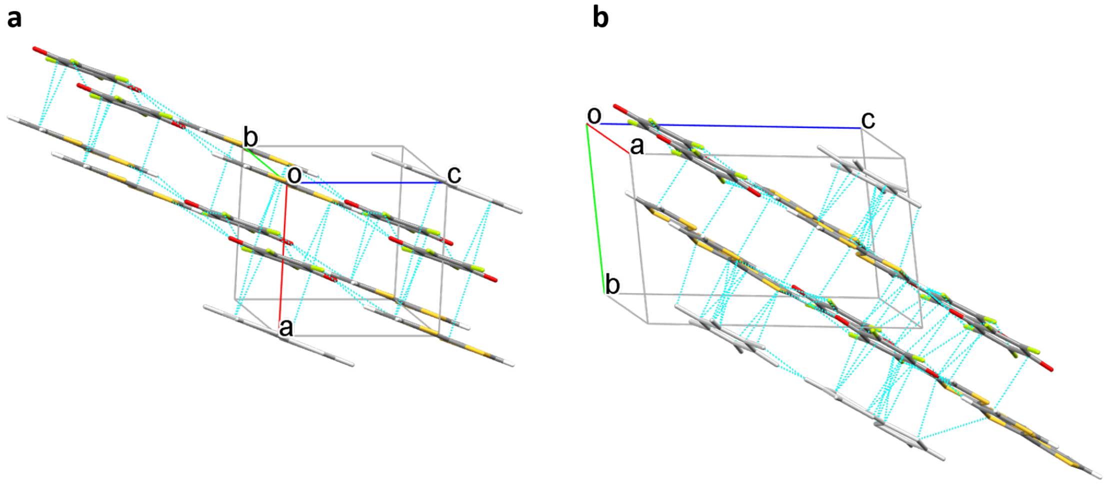

Figure 1.15: *TTF-FA structure viewed perpendicular to bc plane (referred to the N phase): a) N phase and b) I phase. The distances shorter than the sum of VdW radii of the atoms of different molecules are marked in light blue. In both structures the same group of molecules is colored while the other surrounding molecules are grey.*

The shift of the dimers respect to each other also increases the angle between the stack axis and the FA molecular planes from 18.3° to 35.3° For the same reason the $\beta$ angle changes from 93.1° to 83.0° and the $a$ parameter increases by 11%, from 7.054 to 7.863 Å(Table 1.4). This expansion is likely responsible for the crystal cracking at the transition. Indeed, the cracks are nearly perpendicular to the stack direction $a$.

The antiferroelectric arrangement of the ionic phase might be a consequence of the interchain interactions that are also present in the neutral phase (Fig **??** and 1.16).

This motif is maintained in the ionic phase.

Finally, the TTF molecules, no longer laying on the inversion centers, are not planar, being twisted around the central C=C bond. This is likely a consequence of the double bond weakening due to ionization.

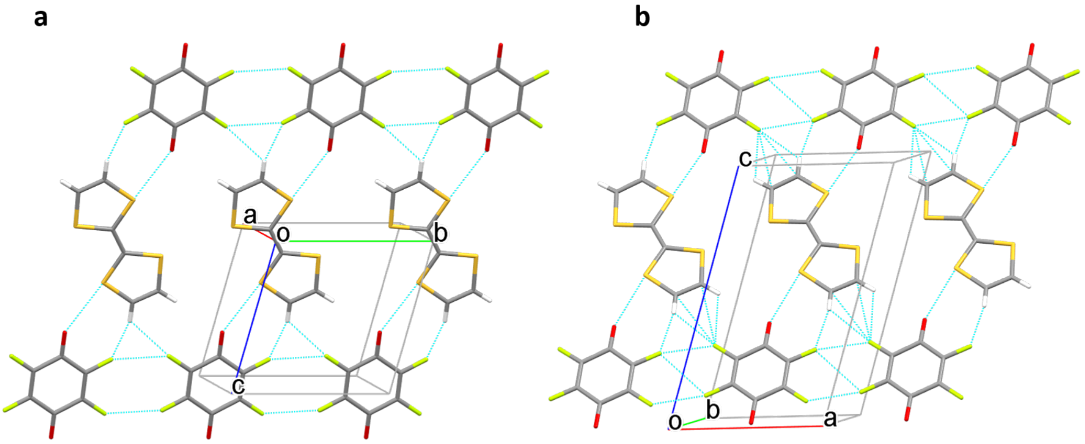

Figure 1.16: *TTF-FA structure viewed perpendicular to bc plane (referred to the N phase): a) N phase and b) I phase. The distances shorter than the sum of VdW radii of the atoms of different molecules are marked in light blue. Only one layer of molecules is shown for clarity.*

### 1.3.7 Calculation of the microscopic parameters

The knowledge of the TTF-FA microscopic parameters is needed to understand its behavior in the context of ms CT systems and to predict its tendency towards valence instability. This can be done following the approach of Refs. [21] and [41], that combines the Modified Hubbard Model and DFT calculations.

The model parameters $z$ (half the energy required to ionize a DA pair) and $t$ (the hopping integral) are obtained from DFT calculations ($\omega$B97XD/6-31+G*) performed on a CT dimer extracted from the crystal structure. It is known that both the electrostatic intermolecular interactions and the electron-molecular vibration coupling, favoring an uneven distribution of the CT electron on the molecular sites, may induce discontinuous valence instabilities [7, 19, 6]. Thus, the most important parameter involved is $\epsilon_T = \epsilon_c + \epsilon_v$ : $\epsilon_c = V - 2M$ accounts for the Coulomb interactions, while $\epsilon_v$ is the vibrational relaxation energy of D and A molecules. Regarding $\epsilon_c$, $V$ is the nearest neighbor Coulomb interaction energy and M is the Madelung energy of the crystal.

The $(\rho - z/t)$ curve of TTF-FA predicts the occurrence of valence instabilities. It is obtained from the universal ($\rho$-$z_{eff}/t$) curve [7], as $z = z_{eff}$+ $\epsilon_T$ $*\rho$ - $\epsilon_v$ . The ground state ionicities are found using the $z^*/t$ value as abscissa, where $z^*/t = z - 0.2$ eV [21].

Since $\epsilon_T/t \gg 1.8$, the curve is S-shaped, indicating a large charge instability range (Table 1.5 and Fig 1.17). In addition, according to the calculations, the room temperature phase is neutral while the low temperature one is ionic. Although the ionicity difference between the two phases is overestimated, these results correctly predict a strongly discontinuous phase transition. The computed model parameters allow the comparison between TTF-FA and other ms CT systems. In this way TTF-FA is close to TTF-CA: despite the differences in crystal packing and D-A overlap [2], the two systems share similar microscopic parameters leading to a discontinuous behavior.

Table 1.5: *Comparison between the estimated Modified Hubbard Model parameters of TTF-FA and TTF-CA. In the case of the I phase, the* $t$ *and* $z$ *values of the two non-equivalent DA pairs are averaged.*

| System | $z$ (eV) | $t$ (eV) | $\epsilon_v$ (eV) | $\epsilon_c$ (eV) | $\epsilon_T$ (eV) | $\epsilon_T/t$ | $z^*/t$ |
|---|---|---|---|---|---|---|---|
| TTF-FA (N) | 0.45 | 0.32 | 0.61 | 0.88 | 1.49 | 4.81 | 0.81 |
| TTF-FA (I) | 0.30 | 0.28 | 0.61 | 1.02 | 1.63 | 5.82 | 0.36 |
| TTF-CA (N) | 0.44 | 0.22 | 0.47 | 0.89 | 1.36 | 6.18 | 1.09 |
| TTF-CA (I) | 0.28 | 0.21 | 0.47 | 1.02 | 1.49 | 7.10 | 0.38 |

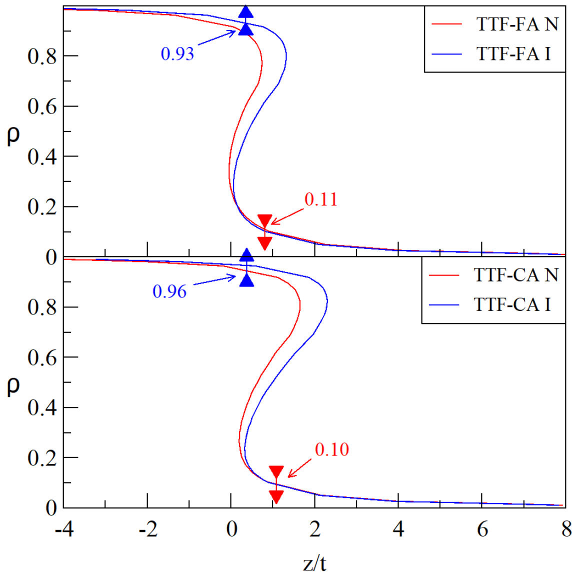

Figure 1.17: *Comparison between the* $(\rho - z/t)$ *curves of the neutral (black line) and ionic (red line) phases of TTF-CA (upper panel) and TTF-FA (lower panel). The triangles indicate the calculated ionicities of both phases, with the corresponding error bar [21]*

### 1.3.8 High pressure

TTF-FA undergoes a first order phase transition around 0.45 GPa, with color change from green to brown, as at low temperature (Fig 1.18). Similarly, the coexistence of both phases can be observed near the critical pressure, suggesting the presence of metastable phases. The transition is reversible without any detectable hysteresis (pressure accuracy 0.05 GPa), but the crystals cracks with cycling the transition.

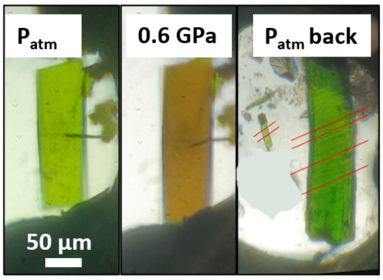

Figure 1.18: *TTF-FA crystal inside the DAC, at 0.2 (left panel) and 0.8 GPa (middle panel). Right panel: crystal cracking after cycling the transition.*

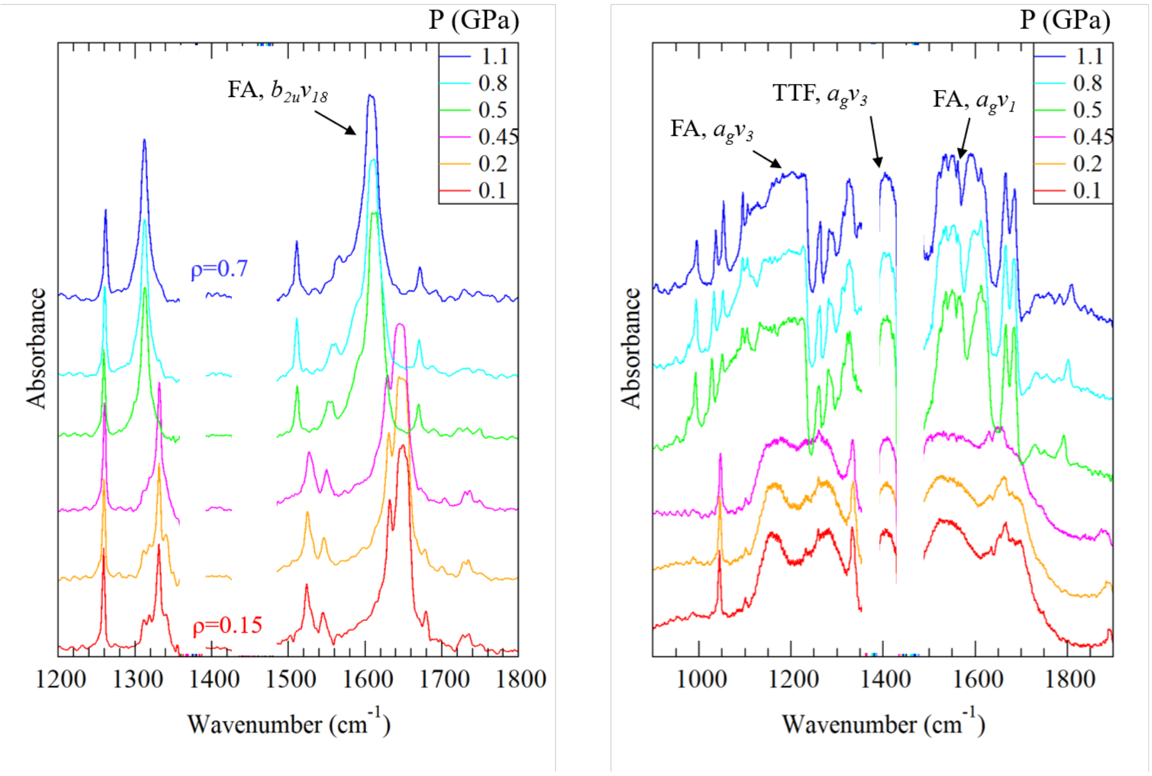

Figure 1.19: *Pressure dependent IR spectra of TTF-FA, measured on the ab face, polarized perpendicular (left panel) and parallel to the stack (right panel). Some spectral ranges are not accessible due to the absorptions of the pressure medium. The spectra are offset for clarity.*

On increasing the applied pressure the IR spectra (Fig 1.19) show the same evolution observed on lowering temperature. The charge sensitive bands of TTF and FA shift, indicating a ionicity increase. In these measurements the FA C=O antisymmetric stretching ($b_{1u}\nu_{10}$) was not accessible as the only crystals available presented an extended *ab* face (Fig 1.4). The band can be seen only as a small projection in the parallel polarized spectra of the neutral phase (Fig 1.19, right panel), since the molecular planes are inclined respect to the stack direction. At 0.4 GPa this band is shifted from 1670 to 1656 cm$^{-1}$ , indicating a ionicity increase from 0.15 to 0.25. At higher pressures it is no longer visible, hidden by the strong vibronic absorptions appearing at the transition. Anyway, the frequency shifts of all the other charge sensitive bands are similar at high pressure and low temperature. Thus, the transition takes place at the same ionicity value and the associated ionicity jump is probably the same, in both conditions.

Also the sidebands, visible in the parallel polarization, display the same evolution observed on cooling. Although these bands are partially covered by the absorptions of the pressure medium, the pair related to FA $a_g\nu_3$ is completely visible. The two bands become closer and broader on increasing pressure. Their distance decreases from 140 cm$^{-1}$ at atmospheric pressure to 90 cm$^{-1}$ at 0.45 GPa. At this pressure the transition suddenly takes place, with the appearance of the totally symmetric bands, that saturate the spectrum. Thus, the stack is dimerized in the high pressure ionic phase.

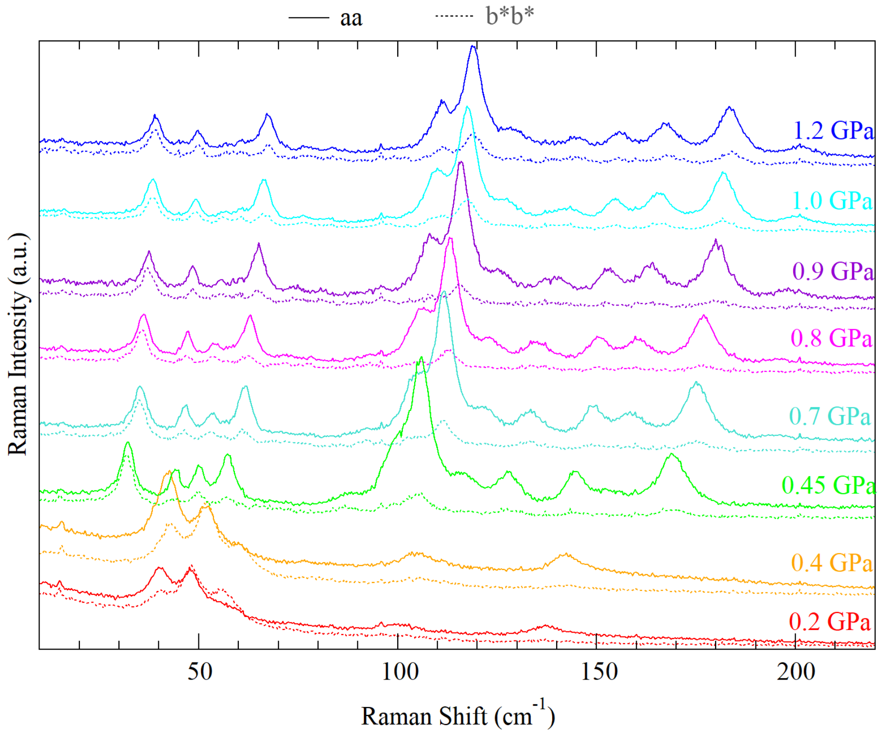

Figure 1.20: *Low frequency polarized Raman spectra of TTF-FA. The spectra are offset for clarity.*

The doubling of the unit cell is evident from the sudden appearance of many phonon bands in the Raman spectra (Fig 1.20). Their pattern and relative intensities in both polarizations (*aa* and *bb*) correspond to the low temperature spectra recorded on the *ab* face (Fig 1.8). The different bandwidth is just a thermal effect. All the phonon bands display a linear frequency hardening on increasing pressure (Fig 1.20). As expected, the hardening is larger than at low T, as the lattice contraction is much larger with increasing pressure (Fig 1.21). The relative intensities are constant in the whole pressure range, except for the bands at 50 and 150 cm$^{-1}$ , that show an opposite behavior on increasing pressure. The same trends were observed on cooling, to a lesser extent.

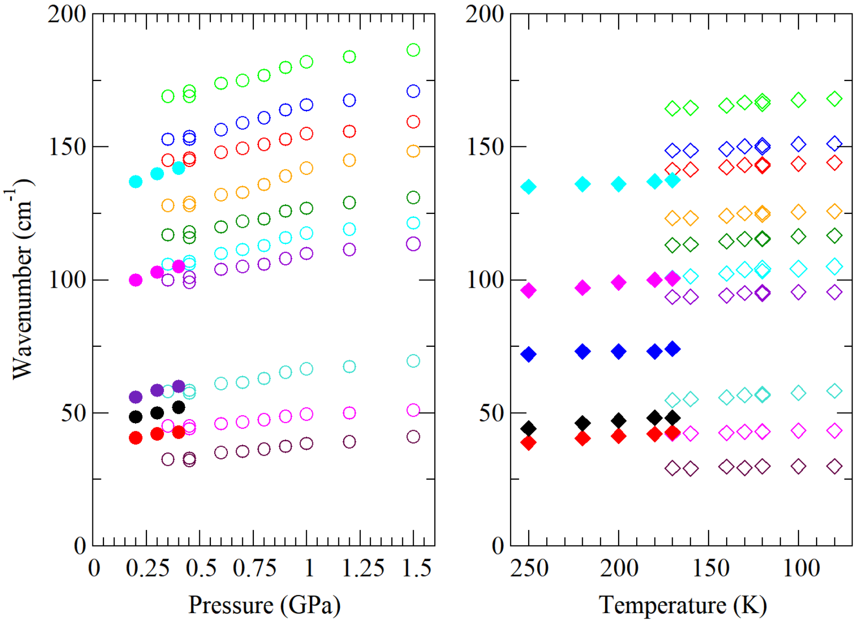

Figure 1.21: *Comparison between the frequency shifts of some low frequency Raman active phonons at high pressure (left panel) and low temperature (right panels). The phonons have the same symbol color in both graphs. The filled symbols correspond to the neutral phase.*

While the applied pressure has a strong effect on the lattice phonons, the frequency shift of the intramolecular modes that are not charge sensitive is lower than the instrumental resolution (2 cm$^{-1}$ ). These pressures are too low to affect the intramolecular vibrations directly by lattice contraction.

Overall, there is clear evidence that the high pressure and low temperature phases are the same ionic phase (Fig 1.22). Also the transition mechanism is probably the same in both conditions. The IR and Raman spectra recorded near the critical pressure are very similar (ionicity, IR sideband distance. . . ) to the corresponding spectra recorded near the critical temperature. The evolution of the spectra never anticipates the transition.

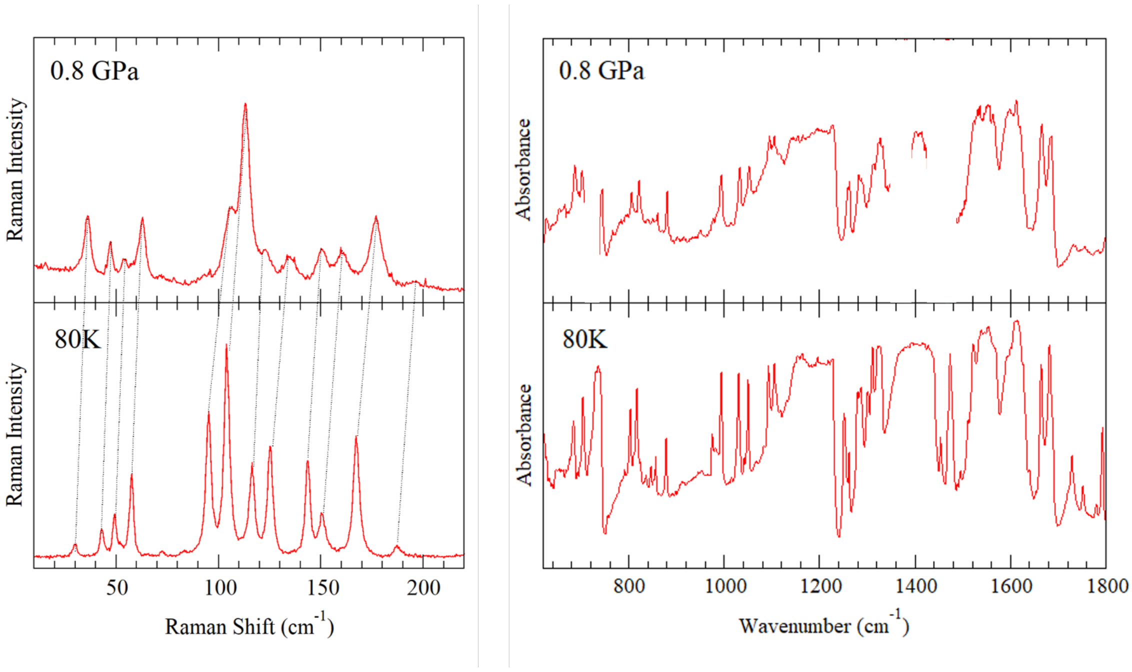

Figure 1.22: *Comparison between Raman spectra with aa polarization (left) and IR spectra polarized along the stack (right), at high P (upper panels) and low T (lower panels).*

## 1.4 Discussion and conclusions

In this study, the Neutral to Ionic phase transition of TTF-FA has been investigated for the first time, both at low temperature and high pressure. The phenomena associated with the transition and the resulting I phase are the same in both conditions. The transition is first order, with a large ionicity jump ($\Delta\rho \simeq 0.5$), stack dimerization and doubling of the unit cell, taking place suddenly and simultaneously, together with sample cracking. In each phase the evolution of the spectra is strongly discontinuous and does not anticipate the corresponding spectra of the other phase approaching the transition.

The same behavior is common with the first order T induced NITs observed in TTF-CA and TMB-TCNQ. However, the space groups of the three CT systems are different: in both TTF-CA and TMB-TCNQ the N-phase is monoclinic $P_{21}/n$, with already two stacks in the unit cell that dimerize at the transition in the polar $Pn$ space group [40, 39]. On the contrary, TTF-FA N-phase is triclinic with one D-A pair in the unit cell. At the transition the stacks dimerize in antiphase resulting in an antiferroelectric order, associated with the doubling of the unit cell. From this perspective TTF-FA broken symmetry is analogous to that of dimethyl-TTF-CA [20]. However, in the latter system the phase transition is close to second order and probably dominated by 1D stack dimerization over that of charge instability. In fact, the softening of the effective Peierls mode is almost complete and the ionicity of the low temperature phase remains below 0.5 [20].

The presence of metastable phases and the large thermal hysteresis suggest a high activation energy, probably due to the drastic structural rearrangement during the transition. The same phenomena were observed in the case of TMB-TCNQ [36, 39]. As in TTF-FA, in the low temperature phase the tilt angle of molecular planes respect to the stack direction increases, with an abrupt variation in the lattice parameters. Thus, the crystal cracks, being unable to relax the resulting elastic stress. Differently, the TTF-CA NIT is purely displacive and occurs with a small hysteresis and no crystal breaking.

Since many simultaneous processes usually play a role in the NIT, the mechanism is often difficult to identify in detail. However, a quite plausible scenario can be put forward on the basis of the general understanding gained through the analysis of the extended Peierls-Hubbard model [6, 42]. NIT is in fact characterized by the interplay between the Peierls electron-phonon coupling, yielding the continuous dimerization of the stack, and the Madelung energy which favors a discontinuous $\rho$ increase. In this case it is clear that the Madelung energy increase following thermal lattice contraction prevails, inducing the observed discontinuous ionicity variation. Furthermore, the low steric hindrance of FA, the smallest haloquinone, reduces the D-A intermolecular distances increasing 3D interactions and the Madelung energy. This is the most likely explanation for the relatively high transition temperature of TTF-FA, compared to other TTF-haloquinone complexes [28, 29]. Also, the sizeable interstack interactions between TTF and FA certainly play an important role in the doubling of the unit cell, leading to an antiferroelectric ordering.

Finally, the modest critical pressure (0.5 GPa) is in agreement with the relatively high critical temperature (160 K). This fact further supports a Madelung energy driven NIT, with an increased chemical pressure effect due to the small acceptor dimensions [29]. In this situation even a small lattice contraction would drive the system to instability.

Interestingly, systems showing discontinuous NIT with a high activation barrier might be subject to photoinduced NIT as well. This means that a pulsed excitation can potentially generate a long-lived metastable phase, as in the case of TTF-CA [10].

# Chapter 2

# The strange case of DMTTF-Fluoranil

## 2.1 Introduction

Among the TTF-haloquinone systems, the TTF-FA first order NIT occurs at a relatively high temperature (170 K at atmospheric pressure) and at a modest pressure (0.5 GPa at room temperature). This behavior was ascribed to the increased Coulomb interactions due to the small acceptor dimensions. It is known that the introduction of bulky substituents on the donor or acceptor molecules weakens these interactions by expanding the crystal lattice, acting as a negative pressure. This results in an increased critical pressure [29]. Thus, we attempted to do the same with TTF-FA, through the substitution of TTF with the bulkier DimethylTTF (DMTTF) donor. Indeed, DMTTF-FA has never been reported.

Following the same methodology of TTF-FA, we were able to grow DMTTF-FA single crystals, that were characterized both at low temperature and high pressure. The results were surprising: while DMTTF-FA does not display T induced NIT, it undergoes the transition at the same modest pressure of TTF-FA.

## 2.2 Experimental

### 2.2.1 Crystal growth

DMTTF-FA single crystals were grown according to the same method used for TTF-FA (see Subsection 1.2.1) As the DMTTF used contained a brown insoluble impurity, DMTTF was recrystallized from a filtered toluene solution before use.

The crystals were green and needle shaped, very similar to TTF-FA (Fig 2.1). The best substrate for the growth was a watch glass, as the crystals grew orderly from the edge of the evaporating solution towards the center of the glass. As in the case of TTF-FA, slower growth methods or solvents different from toluene yielded a brown amorphous substance. The crystals were stored at low temperature to prevent decomposition.

### 2.2.2 Structure determination

Single crystal XRD measurements were performed at 150 K.

### 2.2.3 Spectroscopic measurements

The spectroscopic characterization was performed in the same way described in Section 1.2.3.

For the high pressure measurements, Nujol or perfluorocarbons were used as pressure transmitting medium, to measure the whole mid-IR spectral range.

## 2.3 Results

### 2.3.1 Morphology and structure

The green DMTTF-FA crystals grow as elongated platelets, i. e. the same colour and morphology of other known neutral TTF-haloquinone compounds, as TTF-CA [36], DMTTF-CA and TTF-FA. The extinction directions are parallel and perpendicular to the elongation direction of the crystals. Again, the parallel direction coincides with the stack direction, as the CT excitation is completely polarized along it.

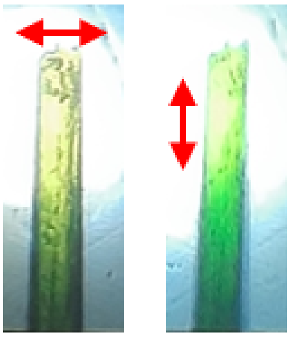

Figure 2.1: *A DMTTF-FA crystal observed with polarized transmitted light.*

XRD confirmed the expected mixed regular stack structure, with 1:1 stoichiometry (Fig 2.2). DMTTF-FA is isomorphous with DMTTF-CA, but the latter has larger lattice parameters due to the bulky Cl atoms. The main difference is along the $b$ direction (corresponding to the $c$ one in DMTTF-FA). The interchain interaction pattern and the DA overlap are the same in the two crystals (Fig 2.3). In both crystals the quinone O-O axis is nearly perpendicular to the long TTF axis, differently from TTF-FA.

In addition, X-ray analysis found that the structure is partially disordered (Fig 2.4). All the molecules have a 10% probability to be slightly rotated with respect to the equilibrium position of the ordered structure, as shown in Fig 2.2.

Such disorder is more likely due to the presence of a fraction of *cis* DMTTF molecules, that can arrange themselves differently in the lattice. Indeed, the starting

DMTTF is probably a mixture of the two isomers and the purification by recrystallization cannot separate them. Moreover, the two isomers cannot even be distinguished by IR spectroscopy, according to DFT calculations performed on both molecules. Thus, we cannot estimate the *cis* DMTTF fraction in the starting reagent or in the cocrystal. Another possible explanation for the disorder is a random arrangement of the DMTTF molecules in the crystal lattice. Due to the 2,5 substitution, DMTTF has two equivalent orientations, related by a rotation of 180° around the long molecular axis. The very rapid growth, required to prevent side reactions, can favor this kind of disorder.

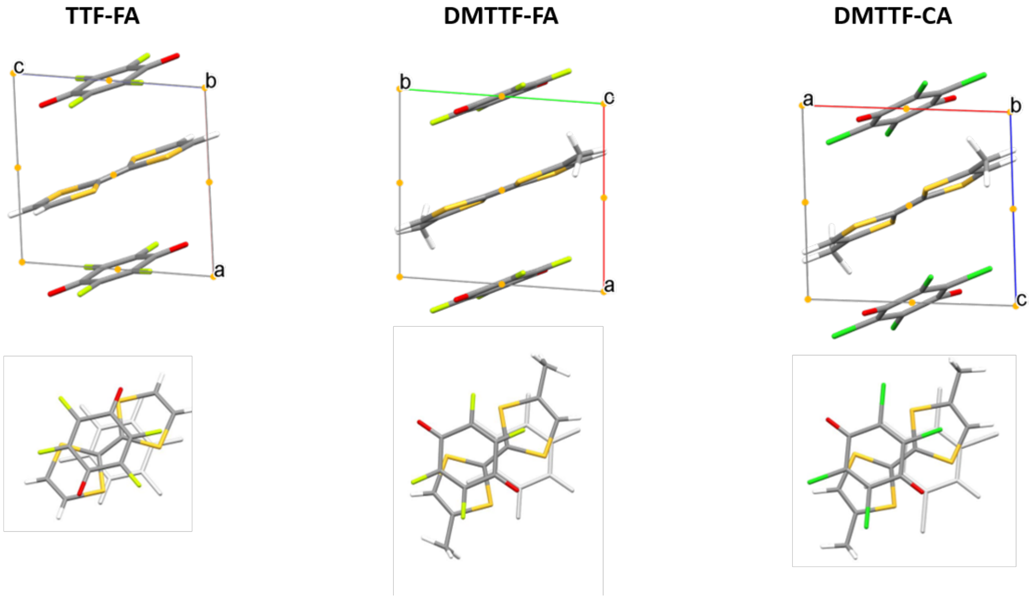

Figure 2.2: *Comparison between the unit cells and DA overlaps in TTF-FA, DMTTF-FA and DMTTF-CA*

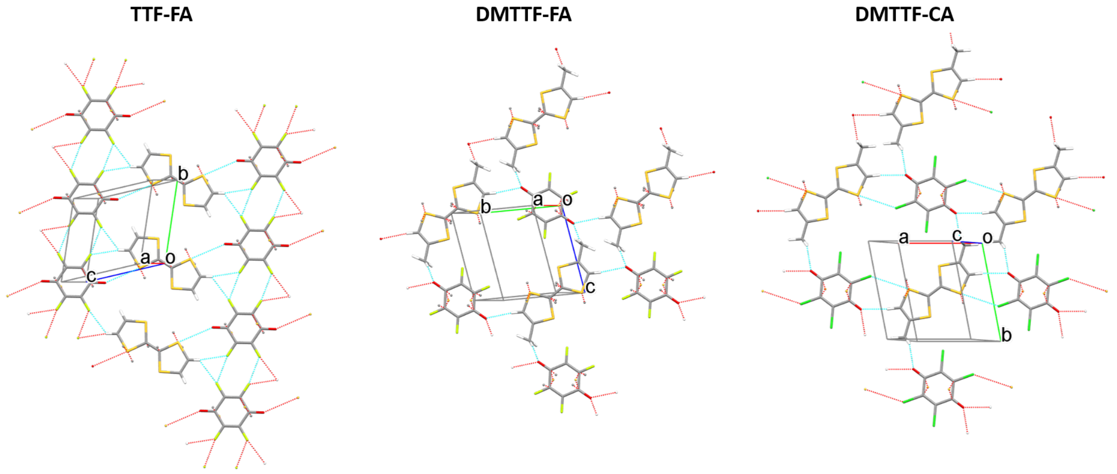

Figure 2.3: *Comparison between the packing motifs of TTF-FA, DMTTF-FA and DMTTF-CA. View perpendicular to the haloquinone molecular planes.*

Table 2.1: *Comparison between the structural parameters of TTF-FA, DMTTF-FA and DMTTF-CA*

| | TTF-FA | DMTTF-FA[1] | DMTTF-CA |
|---|---|---|---|
| Space group | $P-1$ | $P-1$ | $P-1$ |
| $a$ (Å) Å | 7.054[2] | 6.9278 | 7.7 |
| $b$ (Å) | 7.304 | 7.6275 | 8.66 |
| $c$ (Å) | 7.359 | 7.6919 | 7.321 |
| $\alpha$(deg) | 106.15 | 97.581 | 104.94 |
| $\beta$(deg) | 93.101 | 97.447 | 91.84 |
| $\gamma$(deg) | 102.419 | 93.074 | 95.91 |
| V (Å$^3$) | 353.037 | 398.467 | 468.721 |
| $d_{DA}$ / Å | 3.365 | 3.234 | 3.428 |
| Z | 1 | 1 | 1 |

[1] Measured at 150 K.

[2] Stack direction

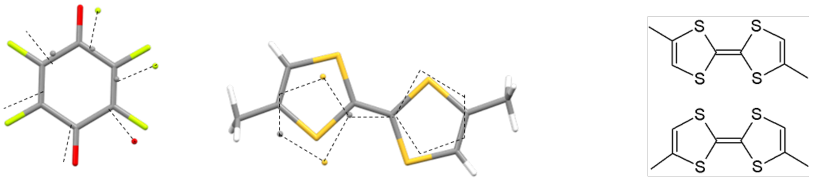

Figure 2.4: *Left: disorder in DMTTF and FA positions. The dashed lines indicate the molecular orientation of the minority component. Right: trans- and cis- DMTTF isomers*

## 2.3.2 Room temperature spectroscopic characterization

Due to the similarity between DMTTF-FA and TTF-FA, we present the DMTTF-FA spectra following the same approach described in Subsections 1.3.3 and 1.3.4, to discuss the ionicity and the stack symmetry. The ionicity determination requires the assignment of the charge sensitive modes, found in the IR spectra polarized perpendicular to the stack. Here we find the in-plane antisymmetric vibrations of DMTTF and FA (Fig 2.5 and Table 2.2). Among them, the strong and charge sensitive FA $b_{1u}\nu_{10}$ and $b_{2u}\nu_{18}$ [37, 22] are redshifted from 1700 and 1670 cm$^{-1}$ to 1672 and 1653 cm$^{-1}$ , respectively. According to the $b_{1u}\nu_{10}$ mode, whose calculated ionization frequency shift is 184 cm$^{-1}$ ( see Subsection 1.3.3), the ionicity is estimated to be 0.14, very close to the TTF-FA value. Also the $b_{2u}\nu_{18}$ shift is consistent with this value.

The DMTTF frequency shifts were not used to estimate the ionicity as they may show nonlinear behavior, as in the case of TTF. Moreover, in neutral DMTTF the antisymmetric C=C stretching (corresponding to $b_{1u}\nu_{14}$ of the TTF skeleton) is very weak. Although the experimental ionization frequency shifts of DMTTF are unknown, DFT calculations suggest a blueshift of the C-H out of plane bending and the C-S stretching bands (748, 774 and 803 cm$^{-1}$ in the neutral molecule). These modes are shifted to 764, 782 and 813 cm$^{-1}$ in DMTTF-FA.

The perpendicular polarized spectra recorded on different crystals are identical. This means that the extended face is parallel to the same crystallographic plane. The comparison between the spectra of single and powdered crystals demonstrates that all the bands are visible measuring on the extended crystal plane. Since the two in-plane molecular axes of DMTTF core and FA are not aligned to the $a$ or $b$ axes, we are unable to identify this plane.

Table 2.2: *Assignment of the polarized IR spectra of DMTTF-FA. The frequencies of the corresponding modes in the pure reagents are reported for comparison. The frequencies are in cm$^{-1}$ .*

| **Perp** | **Par** | **Assignment** | **DMTTF** | **FA** |
|---|---|---|---|---|
| 650 | | | 650 | |
| | 721 | FA $b_{3u}\nu_{28}$ | | 737 |
| | 764 | C-H bending | 748 | |
| 782 | 782 | C-S stretching | 774 | |
| 813 | 813 | C-S stretching | 803 | |
| 985 | 985 | FA $b_{2u}\nu_{20}$ | | 994 |
| 1043 | 1042 | FA $b_{1u}\nu_{12}$ | | 1046 |
| 1114 | 1112 | | 1109 | |
| | 1152 | sideband | | |
| | (1213 1235) | FA $a_g\nu_3$ | | |
| 1223 | | | 1220 | |
| 1279 | | | | |
| 1312 | | FA $b_{1u}\nu_{11}$ | | 1330 |
| 1378 | | | 1374 | |
| | 1402 | sideband | | |
| 1430 | 1430 | $CH_3$ bending | 1424 | |
| 1444 | 1444 | $CH_3$ bending | 1436 | |
| | 1483 | C=C sym stretching | 1374 | |
| | 1542 | sideband | | |
| 1558 | | C=C asym stretching | 1582 | |
| 1653 | 1650 | FA $b_{2u}\nu_{18}$ | | 1673 |
| 1672 | | FA $b_{1u}\nu_{10}$ | | 1700 |
| | 1700 | sideband | | |

The IR spectrum recorded with the electric field polarized along the stack is saturated above 4000 cm$^{-1}$ due to the strong charge transfer band, occurring at around 6000 cm$^{-1}$ . As expected, the out of plane modes of both molecules (721 and 764 cm$^{-1}$ ) are mainly polarized in this direction (Fig 2.5). However, also the in-plane bands have sizeable projections in this polarization, as the molecular planes are tilted respect to the stack direction.

Most important, also the vibronic features are polarized along the stack. The broad absorptions in correspondence with three Raman active totally symmetric modes (Fig 2.6) are easily recognized as sidebands [15] (see Subsection 1.3.4). In addition, some weaker peaks are found between the sidebands, at exactly the same frequencies of the totally symmetric modes. The band at 1483 cm$^{-1}$ , assigned to DMTTF symmetric C=C stretching (corresponding to TTF $a_g\nu_3$), cannot be accidental, being absent in the perpendicular polarization. If the mutual exclusion rule is not respected, the inversion symmetry of the molecular sites must be broken. The weak intensity of these vibronic peaks excludes a dimerized stack and agrees with the structural disorder found by XRD.

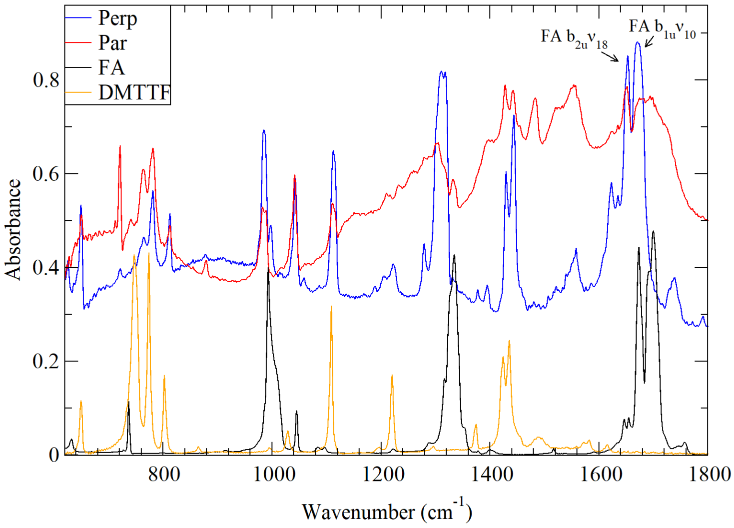

Figure 2.5: *Comparison between the polarized IR spectra of DMTTF-FA (red and blue) and the unpolarized spectra of thin films of DMTTF (orange) and FA (black). The DMTTF-FA spectra offset for clarity.*

Finally, the polarized Raman spectra in the intramolecular vibration range (Fig 2.7, lower panel) are very similar to the corresponding ones of the TTF-FA N phase, both in the relative intensities and the frequencies of the bands. The three most strongly coupled totally symmetric modes are redshifted in the same way by both charge transfer and e-mv coupling in the two compounds. This is consistent with the similar ionicity value and CT excitation frequency. At lower frequencies, in the range 0-200 cm$^{-1}$ , five broad phonon bands can be resolved below 200 cm$^{-1}$ (Fig 2.8, upper panel). Such band broadening gives further evidence of disorder, of static or dynamic nature.

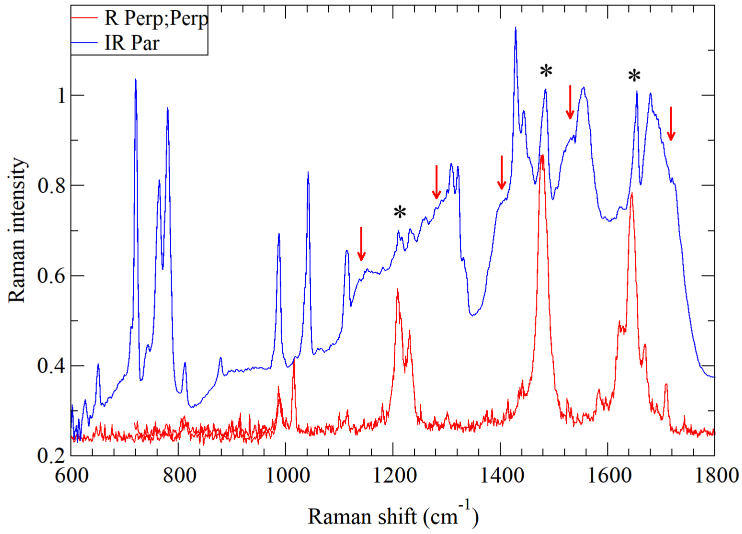

Figure 2.6: *Comparison between DMTTF-FA parallel polarized IR spectrum and Raman spectrum recorded with both exciting and scattered light polarized perpendicular to the stack. The asterisks indicate the probable vibronic bands while the red arrows indicate the sidebands*

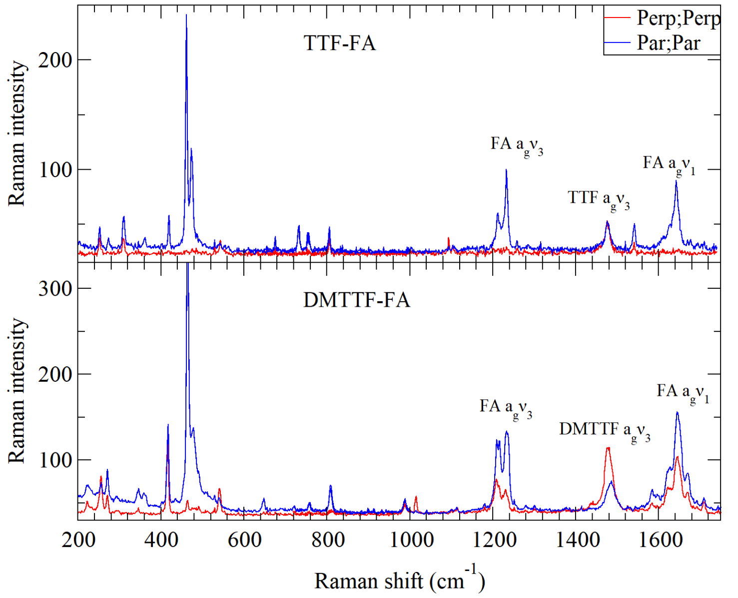

Figure 2.7: *Comparison between the polarized Raman spectra of TTF-FA (measured on face ab) and DMTTF-FA. The exciting and scattered light are polarized in the same direction, perpendicular or parallel to the stack.*

### 2.3.3 Low temperature behavior and disorder

Differently from TTF-FA, DMTTF-FA does not undergo any phase transition on cooling down to 20 K. The mid-IR spectra show minor changes. In the perpendicular polarization, the FA charge sensitive modes $b_{1u}\nu_{10}$ and $b_{2u}\nu_{18}$ are redshifted to 1663 and 1650 cm$^{-1}$ , indicating slight ionicity increase (Fig 2.9). In the parallel polarization, the sidebands are almost unchanged and the totally symmetric bands are still visible, with the same weak intensity as at RT.

In the Raman spectra the three most strongly coupled totally symmetric bands are split and display a continuous intensity redistribution towards the lower frequency components on cooling (Fig 2.10). This behavior, of unclear origin, has been frequently observed in the neutral phases of many TTF-haloquinone cocrystals on lowering temperature or increasing pressure.

The lattice phonons display a continuous frequency hardening on lowering temperature. The intensity decrease of the broad band at 25 cm$^{-1}$ is just a thermal effect (Fig 2.11). Indeed, at such low frequencies many levels are thermally populated at room temperature, resulting in an increased Raman intensity [43]. Despite the structural disorder detected by XRD, the phonon bands are much narrower at 80 K than at room temperature. This suggests that the room temperature bandwidth is mainly due to dynamic disorder, that might be enhanced by the static one. Finally, at low temperature six bands can be resolved, in agreement with the predictions based on the multiplicity of the unit cell, containing a DA pair.

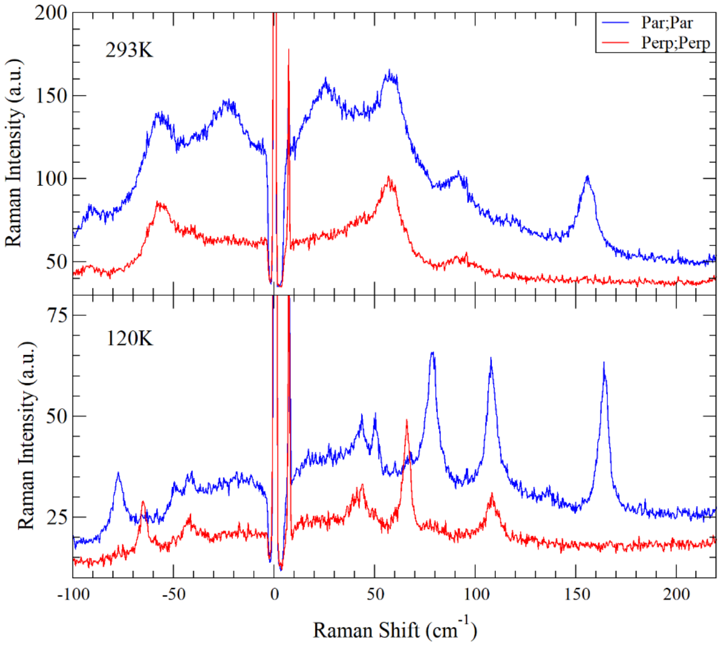

Figure 2.8: *Comparison between DMTTF-FA parallel polarized IR spectrum and Raman spectrum recorded with both exciting and scattered light polarized perpendicular to the stack, at 293 and 82K. The corresponding perpendicular polarized spectra (dashed blue line) are also shown to distinguish the projections of IR active modes from the totally symmetric ones.*

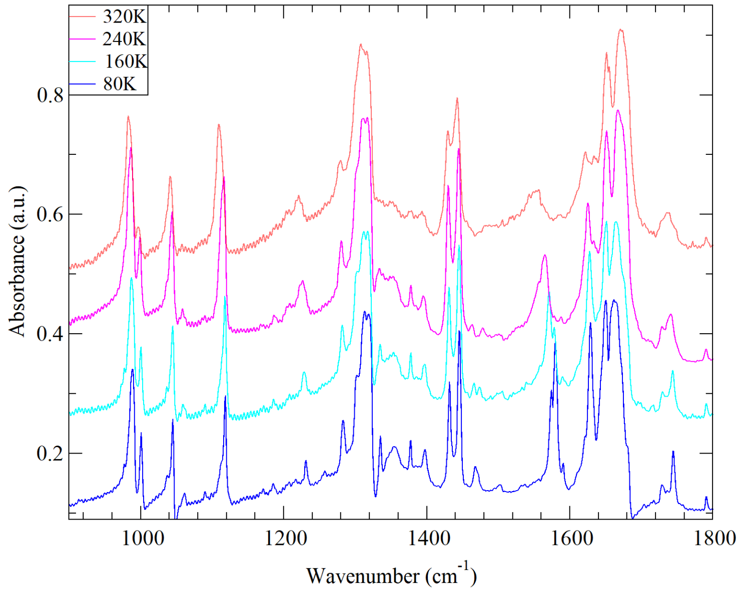

Figure 2.9: *Perpendicular polarized IR spectra of DMTTF-FA recorded at different temperatures. The spectra are offset for clarity.*

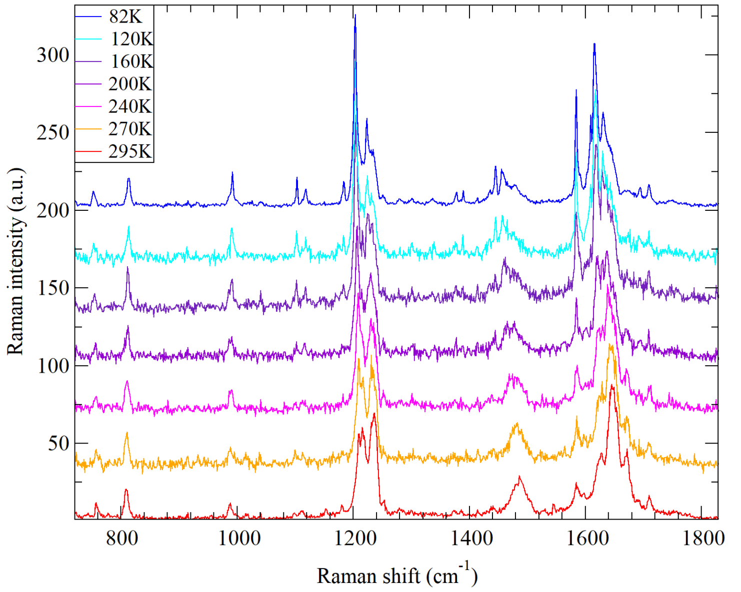

Figure 2.10: *Temperature evolution of the DMTTF-FA Raman spectra, recorded with both exciting and scattered light polarized parallel to the stack. The spectra are offset for clarity.*

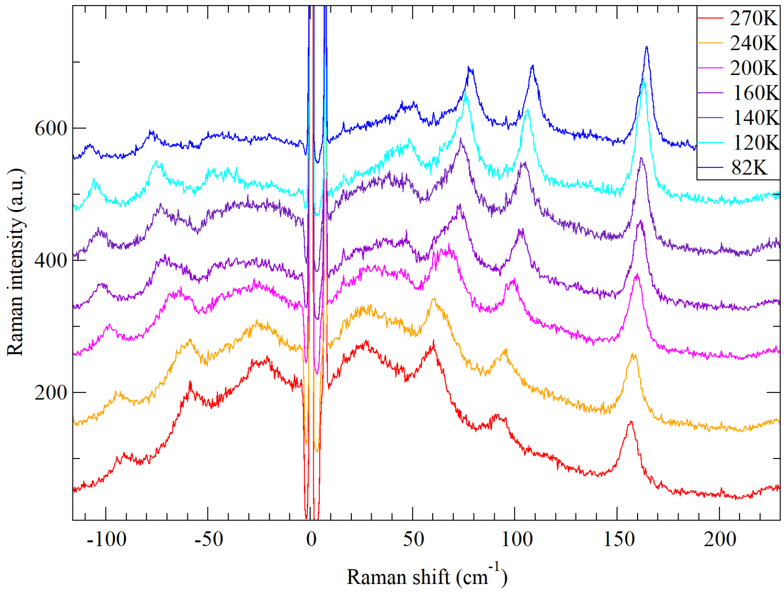

Figure 2.11: *Temperature evolution of the DMTTF-FA Raman spectra in the low frequency range, recorded with both exciting and scattered light polarized parallel to the stack. The spectra are upshifted for clarity.*

### 2.3.4 The phase transition

DMTTF-FA undergoes a first order phase transition at 0.5 GPa associated with a sudden color change from green to brown (Fig 2.12). The transition is reversible without any detectable hysteresis, but with crystal damage. Many parallel cracks appear if the process is cycled (Fig 2.12 c).

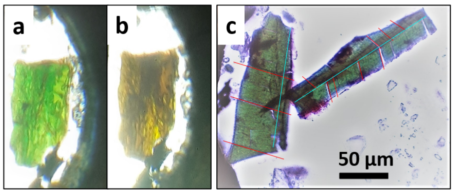

Figure 2.12: *A DMTTF-FA crystal observed with polarized transmitted light, at 0.2 (a) and 0.6 (b) GPa. (c) Crystal cracking after the transition (red lines). The blue lines indicate the stack direction. The crystal on the right is twinned.*

### 2.3.5 Ionicity change

The IR spectra polarized perpendicular to the stack show a strongly discontinuous evolution on increasing pressure. The ionicity is estimated using the frequency shift of the FA C=O antisymmetric stretching mode $b_{1u}\nu_{10}$. In the green phase this band is well resolved from the close C=c antisymmetric stretching mode $b_{2u}\nu_{18}$. Differently, in the brown phase a single strong and broad band centered at 1620 cm$^{-1}$ with a shoulder around 1600 cm$^{-1}$ is detected (Fig 2.13). These two band can be assigned to FA $b_{1u}\nu_{10}$ and $b_{2u}\nu_{18}$, respectively. According to the $b_{1u}\nu_{10}$ shift, the ionicity jumps from 0.15 to 0.45 at the transition. In both phases these two bands are almost unshifted on approaching the transition. As in the case of TTF-FA, the ionicity does not increase above the critical pressure (Fig 2.13, inset). Differently, the Neutral-Ionic borderline $\rho = 0.5$ is not crossed at the transition, that therefore can be defined a valence instability rather than a true NIT.

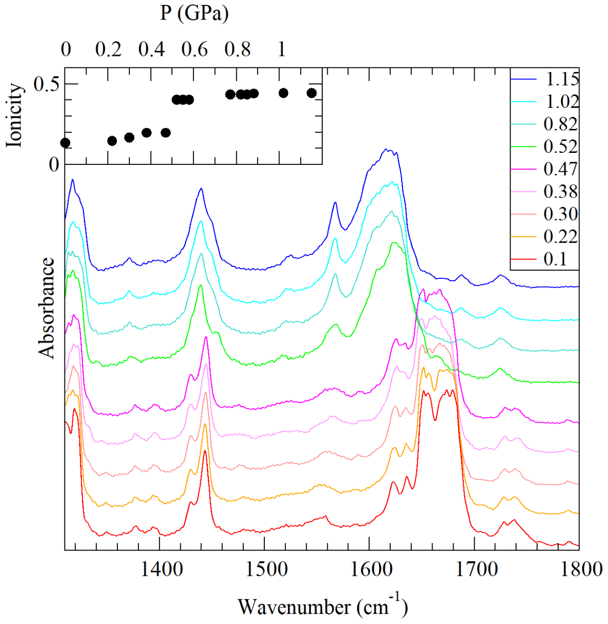

Figure 2.13: *Pressure evolution of the DMTTF-FA IR spectra polarized perpendicular to the stack. The spectra are offset for clarity. Inset: Ionicity changes of TTF-FA estimated from the FA* $b_{1u}\nu_{10}$ *frequency.*

### 2.3.6 Symmetry breaking

At the transition, three strong absorptions appear in the IR spectrum polarized parallel to the stack, corresponding to the totally symmetric modes found in the Raman spectra. This clearly indicates the dimerization of the stack (Fig 2.14).

The Raman bands are much broader than in TTF-FA, in the whole frequency range. For this reason, some bands are difficult to study. For example, DMTTF $a_g\nu_3$ cannot be separated from the broad Nujol band around 1400 cm$^{-1}$ and is easily hidden by weak ruby fluorescence. At low frequency, the transition is associated with the appearance of many new bands and the intensity enhancement of the (Par;Par) polarized phonons (Fig 2.15). In the green phase the phonon band intensity is weak, comparable with the low frequency signal due to the pressure medium. Differently, in the brown phase all the bands are clearly visible.

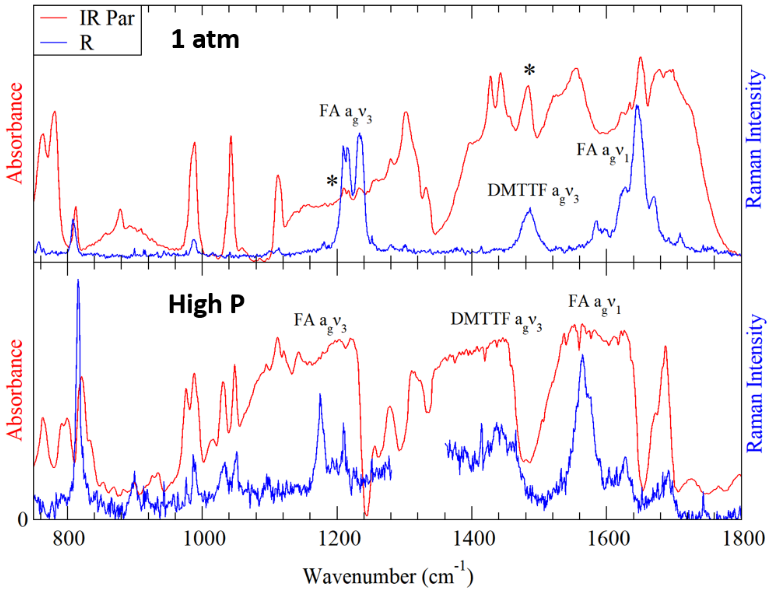

Figure 2.14: *IR spectra polarized parallel to the stack, at atmospheric pressure (upper panel) and 0.9 GPa (lower panel). In the latter two different spectra recorded at the same pressure in PFC (above 1340 cm$^{-1}$ ) and in Nujol (below 1340 cm$^{-1}$ ) were merged.*

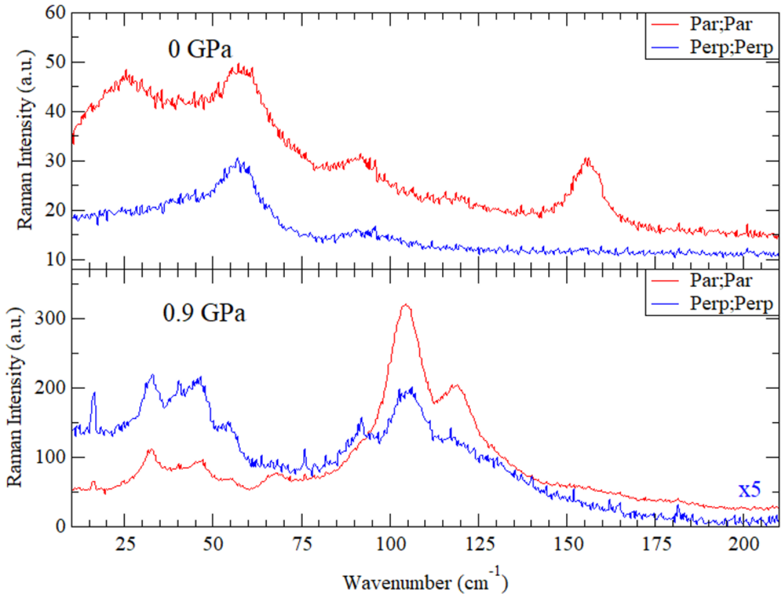

Figure 2.15: *Polarized low frequency Raman spectra recorded at atmospheric pressure (upper panel) and 0.9 GPa (lower panel).*

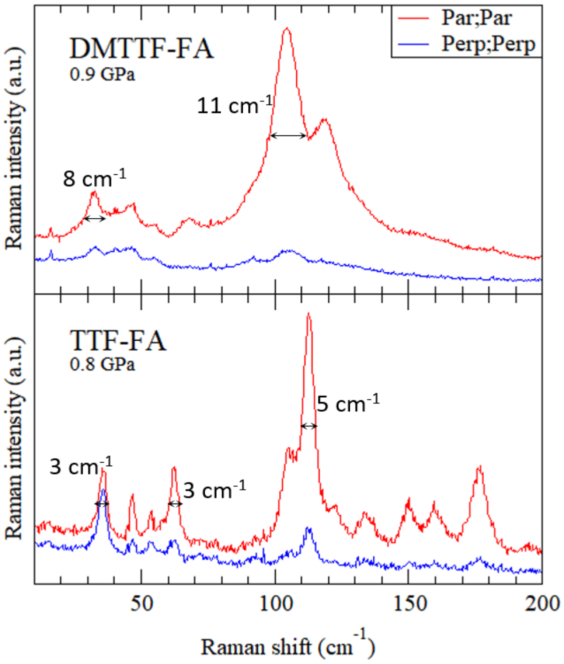

Figure 2.16: *Comparison between the low frequency Raman spectra of the high pressure phases of DMTTF-FA (upper panel) and TTF-FA (lower panel).*

Overall, in the spectra of the brown phase eight bands can be resolved, but more weaker bands might be present. The exact number is uncertain due to the superimposition of broad bands. The phonon bands are much broader in DMTTF-FA than in TTF-FA at similar pressures (Fig 2.16). This means that the DMTTF-FA structural disorder is maintained in the high pressure brown phase. Anyway, the number of bands suggests the doubling of the unit cell in the brown phase. The absence of new bands with crossed polarization would be consistent with a triclinic symmetry, as in the green phase. Finally, the pressure evolution of the lattice phonons never anticipates the transition, as in TTF-FA. In both phases the bands display a linear frequency hardening on increasing pressure.

## 2.4 Discussion and conclusions

The charge transfer crystal DMTTF-FA has been prepared and characterized for the first time, revealing a first order valence instability induced by pressure. Despite the relatively low critical pressure (0.5 GPa), the phase transition does not occur at low temperature.

This behavior is unexpected. Kaźmierczak et al. reported that applying pressure between 0.2 and 0.5 GPa causes the same volume variation as cooling from 300 to 100 K [44]. This p-T correspondence is respected in the case of TTF-FA, whose transition occurs at a pressure of 0.5 GPa at 300 K or on cooling to 170 K at atmospheric pressure. Surprisingly, the phonon frequency hardening of the green DMTTF-FA phase seems to obey the rule. Indeed, a pressure of 0.45 GPa and a temperature of

200 K result in the same phonon frequency shift (Fig 2.17). However, at this point the pressure increase induces the transition, while the temperature decrease does not. Further cooling results in larger frequency hardening.

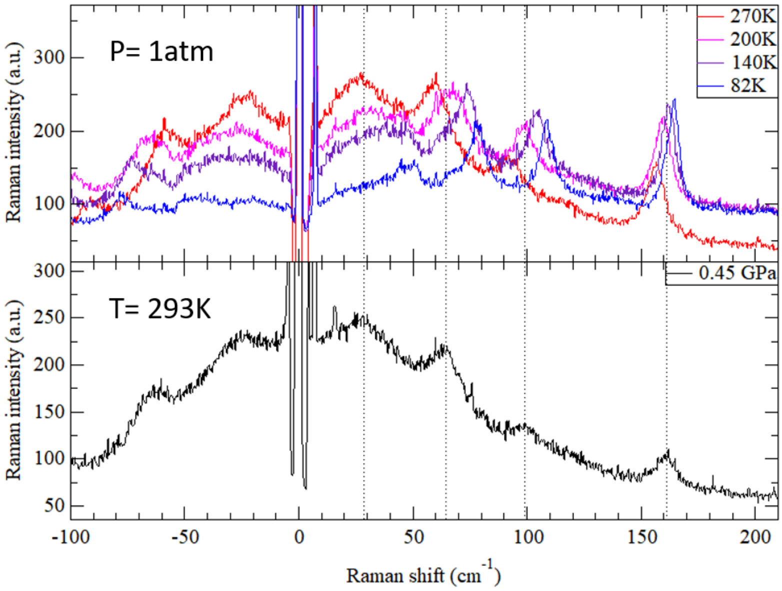

Figure 2.17: *Comparison between the temperature dependent low frequency Raman spectra and the corresponding spectrum measured at a pressure of 0.45 GPa. Both exciting and scattered light are polarized along the stack.*

The pressure induced phase transition is very similar in TTF-FA and DMTTF-FA: it is strongly first order, associated with ionicity jump, stack dimerization and doubling of the unit cell. But DMTTF-FA presents a smaller ionicity jump (0.3). Also the calculations based on the Modified Hubbard Model (see Subsection 1.3.7) gave very similar microscopic parameters in the two crystals, despite the different packing motifs (Table 2.3 and Fig 2.18). Since $\epsilon_T/t \gg 1.8$, DMTTF-FA shows bistability in a wide ionicity range. Thus, it should be subject to valence instability as well.

Also the comparison with the isomorphous DMTTF-CA suggests that DMTTF-FA should display both temperature and pressure induced valence instability. Since the DMTTF-CA critical pressure and critical temperature are respectively 1.2 GPa and 65 K, the DMTTF-FA critical temperature would be expected above 65 K at atmospheric pressure. Concerning the calculated $\rho - z/t$ curves, the s-shape is more pronounced in DMTTF-CA than in DMTTF-FA, due to a smaller $t$ value 2.5. Apparently, these results disagree with the experimentally observed behavior of the two crystals. However, the model can only predict the occurrence of valence instabilities, but cannot estimate the critical temperatures or pressures, dependent on thermal expansion and compressibility.

Table 2.3: *Comparison between the estimated Modified Hubbard Model parameters of TTF-FA, and DMTTF-FA. The DMTTF-CA parameters are reported from [21] for comparison.*

| System | $z$ (eV) | $t$ (eV) | V (eV) | M (eV) | $\epsilon_v$ (eV) | $\epsilon_c$ (eV) | $\epsilon_T$ (eV) | $\epsilon_T/t$ | $z^*/t$ |
|---|---|---|---|---|---|---|---|---|---|
| TTF-FA | 0.45 | 0.32 | -2.55 | -1.72 | 0.88 | 0.61 | 1.49 | 4.68 | 0.78 |
| DMTTF-FA | 0.42 | 0.32 | -2.45 | -1.65 | 0.85 | 0.62 | 1.47 | 4.56 | 0.69 |
| DMTTF-CA | 0.4 | 0.21 | -2.41 | -1.6 | 0.79 | 0.49 | 1.28 | 6.10 | 1.09 |

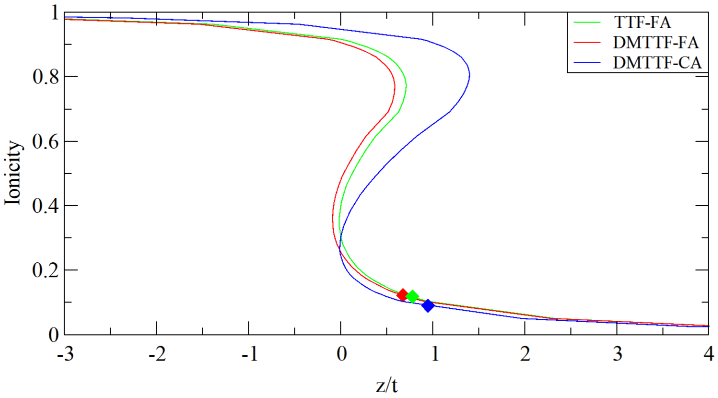

Figure 2.18: *Comparison between the ($\rho - z/t$) curves of the neutral phase of TTF-FA, DMTTF-FA and DMTTF-CA. The triangles indicate the calculated ionicities of both phases. The DMTTF-CA parameters are reported from [21].*

The most likely explanation for the DMTTF-FA discrepancy is that the green phase might be metastable at low temperature. This means that the transition is associated with a high activation barrier due to a significant structural rearrangement. Such hypothesis is consistent with the extensive crystal cracking observed with cycling the transition (Fig 2.12c). Sample damage occurred also in the case of TTF-FA, whose transition is associated with a drastic rearrangement (see Subsection 1.3.6). In the case of DMTTF-FA the activation barrier might be either intrinsically higher than in TTF-FA or increased by the structural disorder.

A more unlikely explanation is that the different high pressure and low temperature behavior could be an intrinsic DMTTF-FA property. For instance, in the case of the isomorphous system DMTTF-CA the low temperature phase and the high pressure one are not the same [45]. Furthermore, in crystals the thermal expansion coefficient and the compressibility are tensors and might be different in the two environmental conditions [44].

The role of disorder can be clarified by growing new crystals, after a careful DMTTF purification. This is a hard task, still in progress. Another interesting issue is the structure determination of the high pressure phase, not possible with the cell available in our laboratory.

# Chapter 3

# N,N,N',N'-Tetramethylbenzidine-TCNQF$_x$ series

## 3.1 Introduction

The control of the crystal packing is a crucial issue in the design of functional molecular materials. It depends on many factors, mainly the strength and the directionality of the intermolecular interactions and the molecular shape. These features can be tuned by chemical modification of the constituent molecules. Consequently, the crystal packing can be controlled through chemical substitution.

Here we pair the strong electron donor N,N,N',N'- Tetramethylbenzidine (N-TMB) with three acceptors of increasing electron affinity: TCNQ, TCNQF$_2$ and TCNQF$_4$ (Fig 3.1). These acceptors have been recently paired with 3,3',5,5'- Tetramethylbenzidine (TMB), a regio-isomer of N-TMB with similar ionization potential and frontier orbitals [46]. The difference between the two isomers is the position of the bulky methyl groups, located on the terminal N atoms in the case of N-TMB and on the aromatic rings in the case of TMB. As a consequence, the N-TMB molecule is longer and narrower and, most important, is not a hydrogen bond donor.

The final aim of this work is the comparison between the crystals within the N-TMB-TCNQF$_x$ series and with the TMB-TCNQF$_x$, to investigate separately the effects of acceptor strength, steric hindrance and H bond. The comparison is based on the morphology and the polarized IR and Raman spectra, since the XRD structure determination is still in progress at the time of writing. Surprisingly, in the case of N-TMB-TCNQF$_4$ two polymorphs were found.

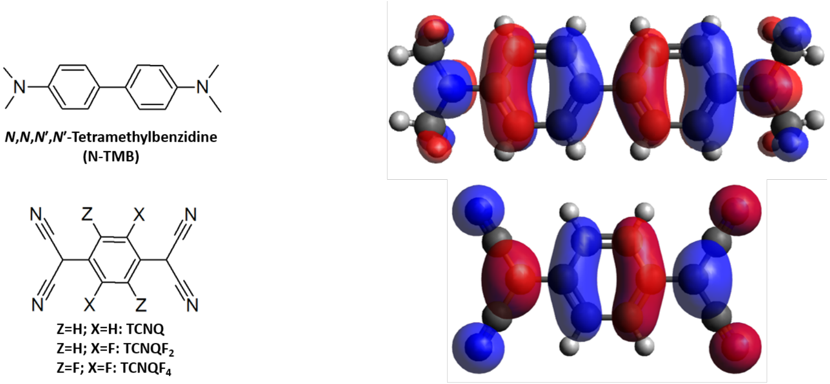

Figure 3.1: *Molecular structures and frontier orbitals of the donor and the acceptors. The overlap between the donor LUMO and the acceptor HOMO is optimized if their long molecular axes are aligned.*

## 3.2 Experimental

### 3.2.1 Crystal growth

#### N-TMB-TCNQ and N-TMB-TCNQF$_2$

The crystals were grown by slowly cooling hot acetonitrile or toluene solutions of the two components, in 1:1 stoichiometric ratio. Since the CT compounds precipitate at room temperature in both solvents, the solutions of the two components were mixed at 80 °C and placed in a dewar filled with hot water. In both compounds the crystals grew as bundles of dark needles in few days Their typical dimensions 5 x 0.05 x 0.01 mm$^3$, shown in Fig 3.2, upper part. Neither of the two compounds showed polymorphism and the needle-like morphology was independent of the solvent used.

#### N-TMB-TCNQF$_4$

In this case, the crystals were grown by both solution and sublimation, obtaining two different polymorphs. The first one, named Phase I, was grown from hot acetonitrile, as in the case of N-TMB-TCNQ and N-TMB-TCNQF$_2$. Due to the strong tendency to precipitate, the starting solutions (60 $\mu$L, $c = 10^{-2} M$) were added to 10 mL of hot solvent. The obtained crystals are very small needles (typical dimensions 0.5 x 0.02 x 0.01 mm$^3$), showing two lateral faces of different colors, purple and blue (Fig 3.11). Toluene solutions yielded instead blue flaky precipitate. The same compound, named Phase II, was obtained as single crystals by physical vapor transport. The two pure components were placed in an open quartz tube under nitrogen flow, as described in Ref [47]. After one day, many thin blue platelets (typical size 1 x 1 x 0.002 mm$^3$) were found in the colder zone of the tube (Fig 3.2).

### 3.2.2 Spectroscopic characterization

The IR spectra were measured in reflectance or absorbance mode according to the procedure described in Section sec:TTFFAmeasurements.

All the Raman spectra were recorded exciting at 632.8 nm, with the Horiba LabRAM HR Evolution spectrometer. The exciting and scattered light were polarized parallel or perpendicular to the stack axis (see next section).

## 3.3 Results and discussion

All the N-TMB-TCNQF$_x$ crytals display strongly anisotropic morphologies and optical properties, with a charge transfer band in the NIR, completely polarized along an extinction direction. Thus, the crystals are positioned in a reference system where the $y$ axis coincides with the polarization direction of the CT excitation, identified as the stack direction. The $xy$ plane is parallel to the largest face, while the $yz$ one is perpendicular to it.

The reflectance spectra recorded with the light polarized along the stack direction are shown in Fig 3.3. The frequencies of the CT bands could not be estimated accurately as the spectral range is too restricted to perform a reliable Kramers-Krönig transformation of the data.

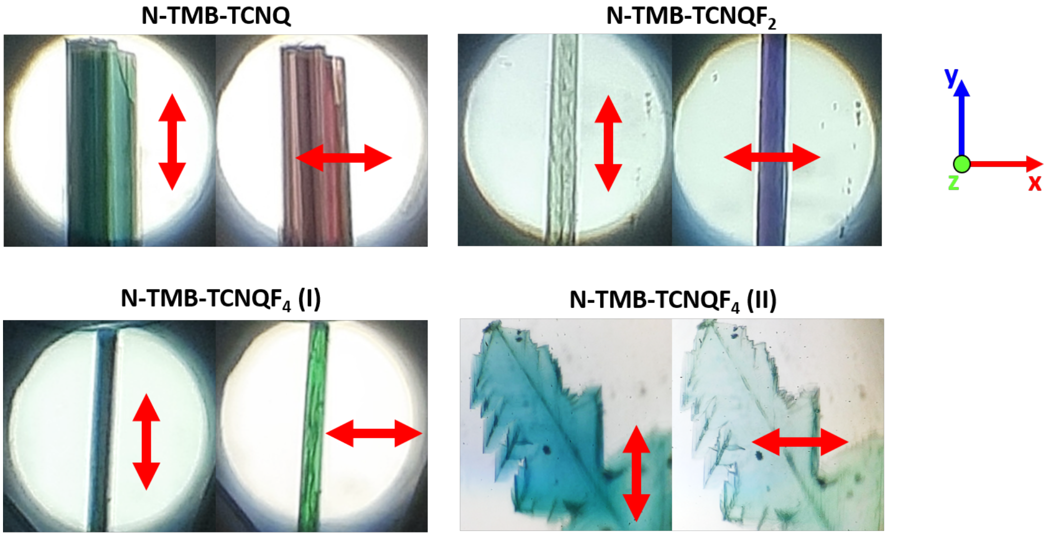
N-TMB-TCNQ

N-TMB-TCNQF$_2$

N-TMB-TCNQF$_4$ (I)

N-TMB-TCNQF$_4$ (II)

Figure 3.2: *Microscopic images of the four N-TMB based crystals. The red arrows indicate the polarization of the transmitted light. In the adopted reference system y is the stack direction.*

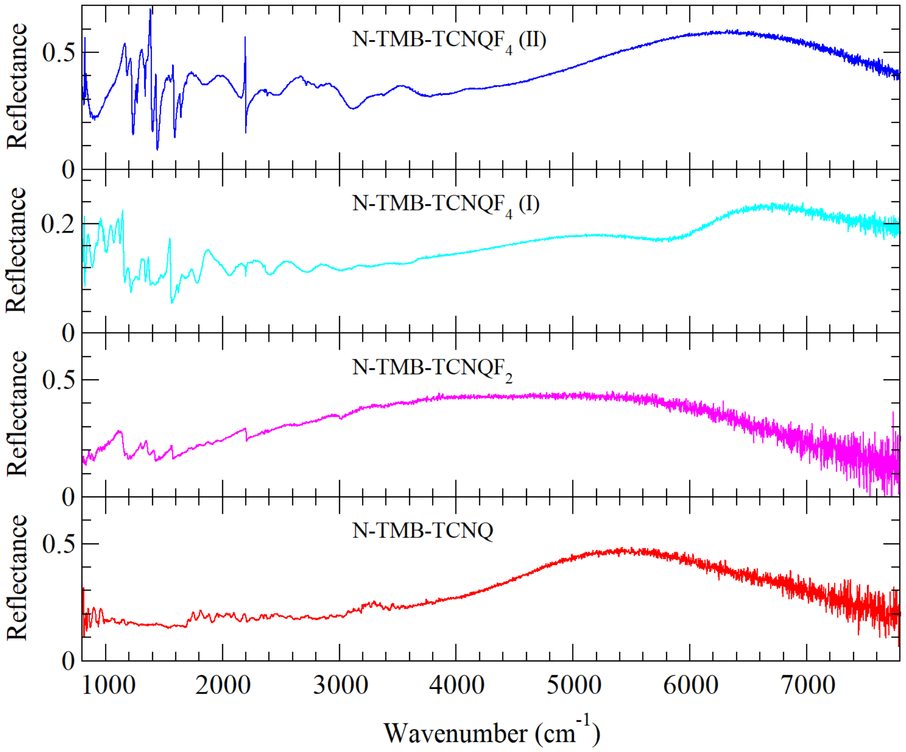

Figure 3.3: *Extended IR reflectivity spectra of the four crystals, polarized along the stack direction.*

### 3.3.1 N-TMB-TCNQ

The crystal morphology is needle-like, with the elongation direction parallel to the stack. Thus, the crystal growth is driven by the strongly directional CT interaction. Such intermolecular force is favoured by the effective overlap between the frontier orbitals of N-TMB and TCNQ, that have similar spatial extension and symmetry respect to the inversion centre (Fig 3.1). Moreover, the N-TMB and TCNQ molecules cannot form other intermolecular interactions of comparable strength.

The degree of charge transfer $\rho$ was estimated from the frequency shift of the charge sensitive C=C stretching band of TCNQ, $b_{1u}\nu_{20}$ [48], visible in the IR spectrum polarized perpendicular to the stack (Fig 3.4). This band is shifted from 1545 to 1533 cm$^{-1}$ , corresponding to a $\rho$ value of 0.29. Also the C≡N stretching band $b_{1u}\nu_{19}$, redshifted from 2228 to 2211 cm$^{-1}$ , gives a similar value of 0.36.

The C≡N stretching frequencies are also very sensitive to environmental effects and often give overestimated ionicity values [49]. In this case, the effect is very small, indicating that the C≡N are not involved in strong interactions, differently from TMB-TCNQ [50, 51]. To summarize, N-TMB-TCNQ is neutral and very similar to the analogue TMB-TCNQ, but with weaker interstack interactions [50].

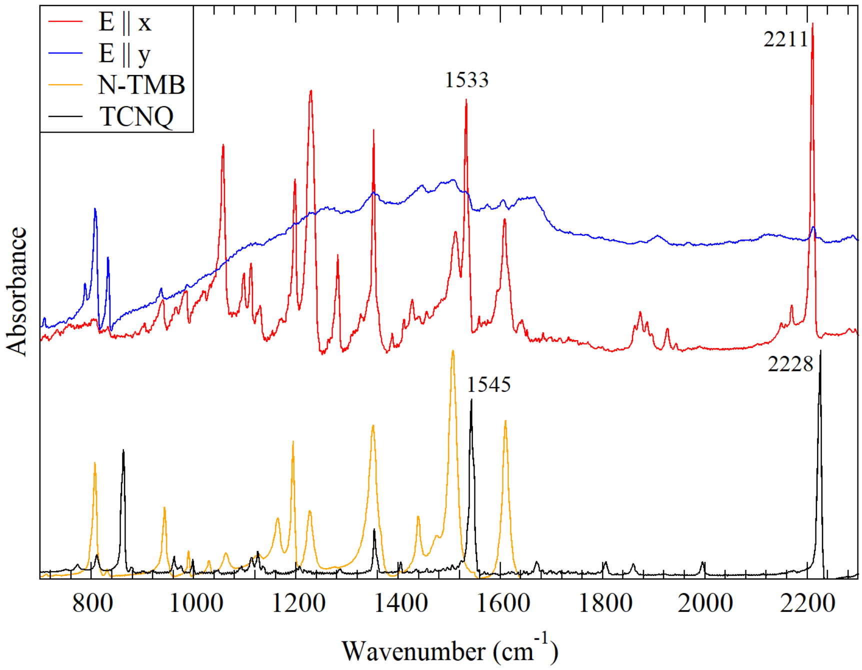

Figure 3.4: *Polarized IR spectra of N-TMB-TCNQ crystals. The spectra of the reagents are shown for comparison. The N-TMB-TCNQ spectra are offset for clarity.*

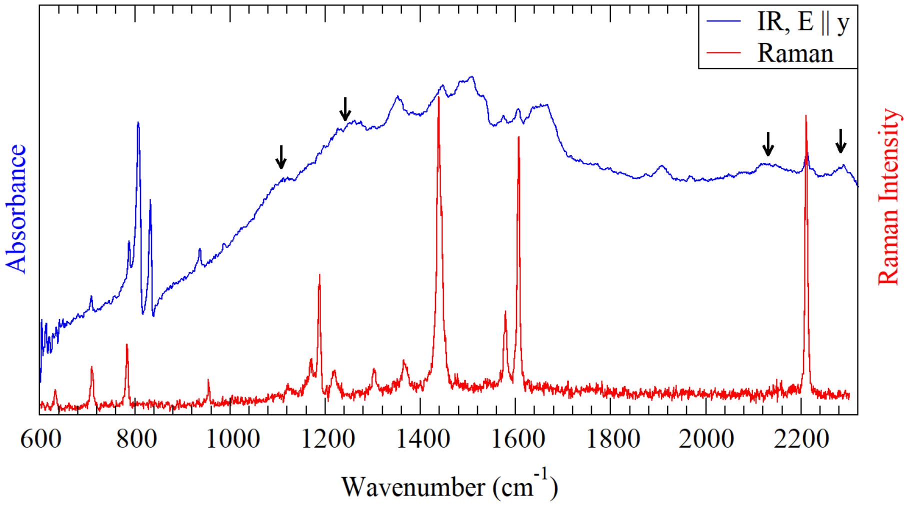

Figure 3.5: *Comparison between the N-TMB-TCNQF$_2$ IR spectrum polarized along the stack and the Raman spectrum, measured with both exciting and scattered light polarized perpendicular to the stack. The black arrows indicate two pairs of sidebands.*

As in the case of TMB-TCNQ, the main feature of the parallel polarized mid-IR spectrum is a very broad band with a complex shape and medium intensity. Since the totally symmetric modes of N-TMB and TCNQ, Raman active, are absent in this IR spectrum, the stack is regular, with the molecules located on the inversion centers. The broad band is likely due to the superimposition of many sidebands related to the totally symmetric modes. Two pairs of sidebands can be singled out, as shown in Fig 3.5. In the same spectrum the out-of plane modes of N-TMB and TCNQ are found around 800 cm$^{-1}$ . Differently from the TTF-quinone cocrystals, the projections of the in-plane modes are negligible. This suggests that the molecular planes lie perpendicular to the stack direction.

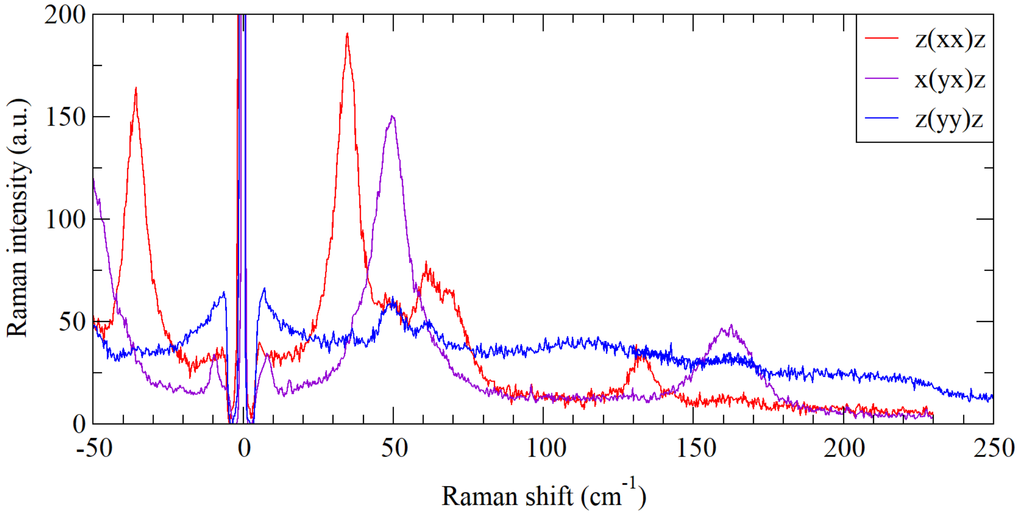

Figure 3.6: *Polarized low frequency Raman spectra of N-TMB-TCNQ.*

More structural information can be achieved from the low frequency Raman spectra, where the lattice vibrations are detected. Overall, 7 bands can be resolved (Fig 3.6). In the *xx* and *yx* polarizations the bands show medium or strong intensity and a typical Lorentzian shape. On the contrary, the *yy* polarized spectrum is very weak, with broad and overlapped features. They might be due to combination bands or disorder induced by the N-TMB methyl groups. The presence of new phonons with crossed polarization suggests that the extended crystal plane contains a symmetry element of order 2. Thus, a triclinic structure can be excluded.

N-TMB-TCNQ does not undergo any temperature or pressure induced phase transition, unlike TMB-TCNQ. Applying a pressure of 2 GPa caused only slight spectral changes. The most likely explanation is that the absence of strong electrostatic interactions inhibits the transition. Indeed, N-TMB-TCNQ and TMB-TCNQ are very similar, but N-TMB is unable to form strong H-bonds, differently from TMB. This further supports the role of 3D Coulomb interactions on valence instabilities.

### 3.3.2 N-TMB-TCNQF$_2$

The crystal morphology and optical properties are very close to those of N-TMB-TCNQ. Similarly, the CT band is completely polarized along the elongation direction of the crystals, that therefore corresponds to the stack axis. Thus, the discussion of the spectroscopic data follows the same lines of N-TMB-TCNQ.

In the IR spectra polarized perpendicular to the stack (Fig 3.7) three charge sensitive TCNQF$_2$ bands are easily identified at 1559, 1537 and 1381 cm$^{-1}$ [52]. Their frequency shifts respect to the neutral TCNQF$_2$ molecule, 17, 13 and 12 cm$^{-1}$ respectively, indicate a degree of charge transfer of 0.27, on average. Thus, N-TMB-TCNQF$_2$ is neutral, despite the higher electron affinity of TCNQF$_2$ with respect to TCNQ. This fact is even more unexpected, considering that the TMB-TCNQF$_2$ ionicity was 0.7 [46].

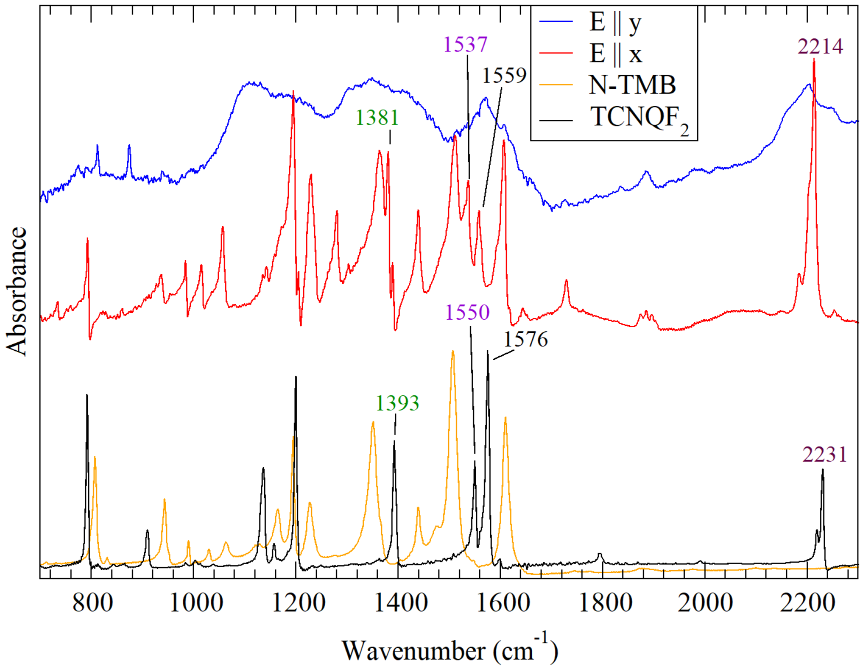

Figure 3.7: *Polarized IR spectra of N-TMB-TCNQF$_2$ crystals. The spectra of the reagents are shown for comparison. The N-TMB-TCNQF$_2$ spectra are offset for clarity.*

The parallel polarized spectrum is saturated by many intense absorptions in the mid-IR. These bands are accessible in reflectance mode. Their frequencies coincide with those of the main Raman bands, suggesting that the molecules do not lie on the inversion centers (Fig 3.8). However, CT crystals having both a low degree of charge transfer and a dimerized stack are uncommon. A possible explanation is that the electron-phonon coupling is strong enough to cause Peierls instability even on the neutral side [6]. The e-mv induced bands might also be due to static disorder along the stack, related to a random orientation of the TCNQF$_2$ molecules [53]. Due to the 2,5 substitution, two equivalent orientations are possible. However, such hypotheses would require a careful experimental verification.

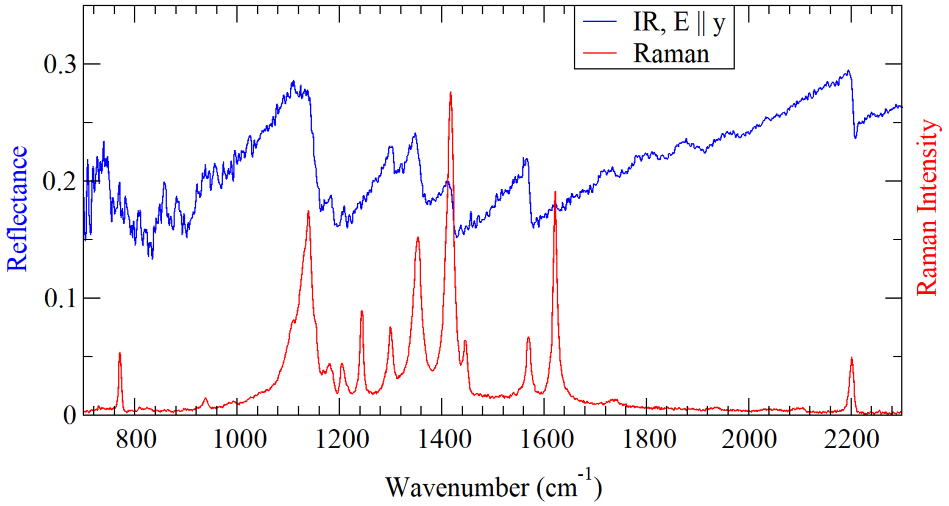

Figure 3.8: *Comparison between the N-TMB-TCNQF$_2$ IR spectrum polarized along the stack and the Raman spectrum, measured with both exciting and scattered light polarized perpendicular to the stack.*

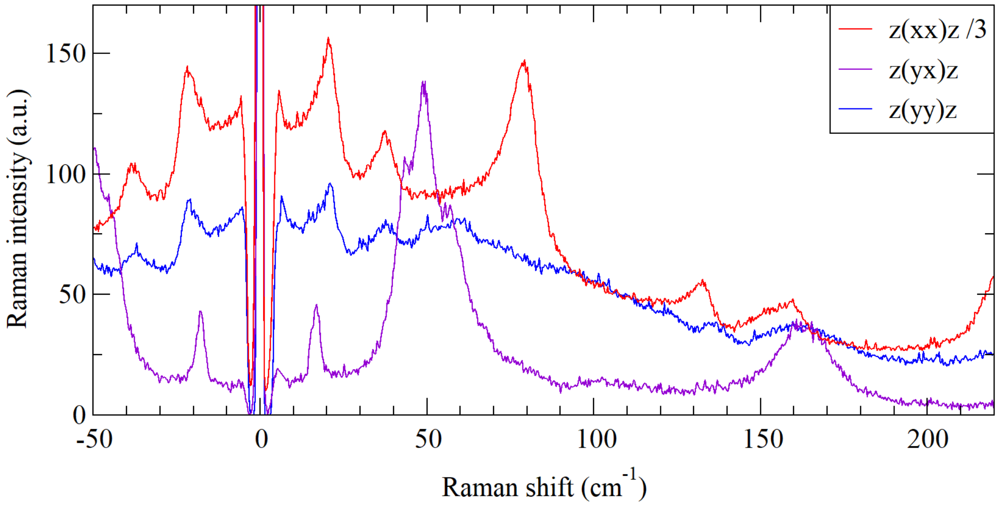

Figure 3.9: *Polarized low frequency Raman spectra of N-TMB-TCNQF$_2$. The xx spectrum has been divided by 3 for clarity.*

A clue leading to structural disorder along the stack is provided by the low frequency Raman spectra (Fig 3.9). The spectrum measured with both the exciting and scattered light polarized along the stack (*yy* polarization) shows a very broad feature. Differently, the bandwidth is smaller in the other two polarizations. Finally, the five phonons having crossed polarization, suggest the presence of a twofold symmetry element in the unit cell, as in the case of N-TMB-TCNQ.

### 3.3.3 N-TMB-TCNQF$_4$

As described in Sec 3.2, two crystal phases with different morphology were found: the Phase I needles and the Phase II platelets. Growing N-TMB-TCNQF$_4$ single crystals from solution is a hard task due to a very rapid precipitation. Anyway, it was possible to obtain Phase I crystals from acetonitrile with a very low concentration and a slow cooling rate. In this case, also a small fraction of Phase II platelets was observed within the batch. Differently, toluene solutions always yielded a flaky Phase II precipitate. Due to the complete insolubility of Phase II in organic solvents even at high temperature, the compound could not be recrystallized. Good quality Phase II single crystals suitable for polarized IR measurements were finally grown by sublimation.

The powder IR spectra of both phases display a CT band, demonstrating the CT nature of both compounds (Fig 3.10, right panel). This band is single in Phase II, while it contains two peaks in Phase I. Although Phase I could be obtained only from acetonitrile, the absence of the solvent C≡N bands at 2340 cm$^{-1}$ excludes a solvated phase (Fig 3.10, middle panel).

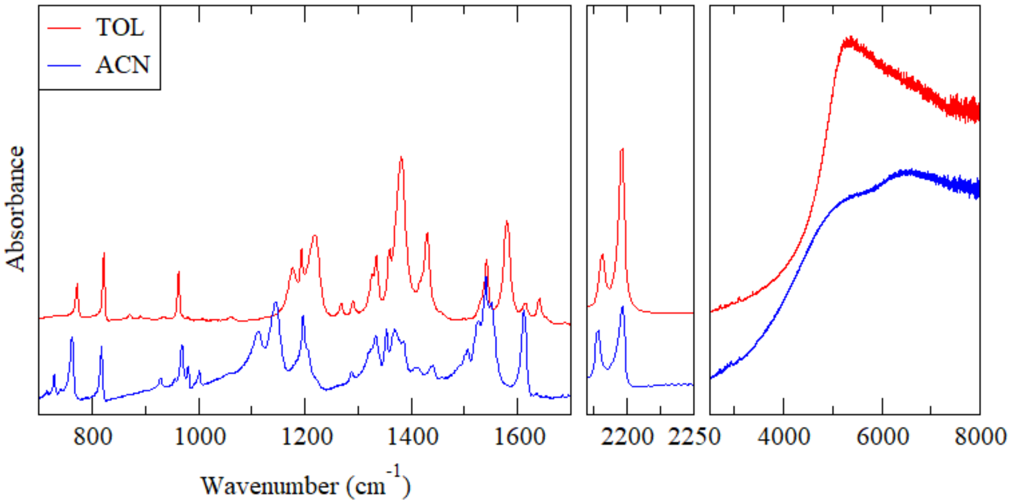

Figure 3.10: *IR spectra of the precipitates obtained by mixing acetonitrile or toluene solutions of N-TMB and TCNQF$_4$. The frequency ranges 1700-2100 cm$^{-1}$ and 2300-3400 cm$^{-1}$ have been omitted due to the absence of significant bands.*

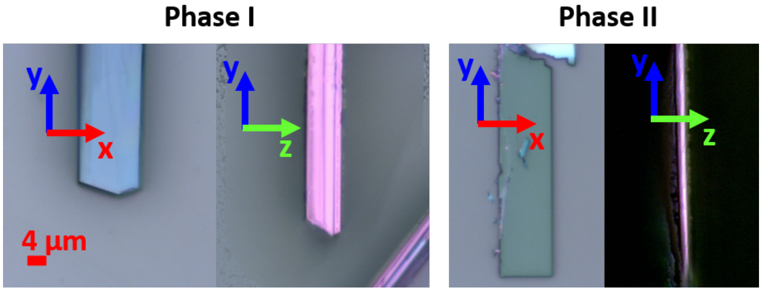

Figure 3.11: *Microscopic images of N-TMB-TCNQF$_4$ crystals, laying on the xy and yz planes. The reflected light is unpolarized. The different blue tone of the two phases only depends on the crystal thickness. The Phase II crystal is so thin as to be transparent.*

Despite the different morphology, the single crystals belonging to both phases share many common features. Firstly, they appear blue and purple when laying on the $xy$ and $yz$ planes, respectively (Fig 3.11). To compare the two polymorphs more accurately, we performed the spectroscopic measurements on both planes. Secondly, the polarized spectra measured on the corresponding planes show very similar patterns. For this reason the two phases are discussed together.

If the crystals lay on the $xy$ plane, in both phases the stack direction coincides with one of the two extinction directions. In Phase I needles the stack is parallel to the elongation direction, as in N-TMB-TCNQ and N-TMB-TCNQF$_2$. In Phase II rectangular platelets the stack is parallel to the longer side.

Viewed in transmission mode, the crystals appear blue when the light is polarized along the stack. If the polarizer is rotated by 90° the color becomes very pale (Fig 3.2). On the contrary, N-TMB-TCNQ and N-TMB-TCNQF$_2$ appeared darker with the transmitted light polarized perpendicular to the stack. This means that in N-TMB-TCNQF$_4$ the in-plane polarized intramolecular electronic transitions cannot be excited with this crystal orientation. Indeed, both phases show a high reflectivity when laying on the $xz$ plane only, indicating that the corresponding transition dipoles are $z$-aligned.

In Phase I the IR spectra polarized perpendicular to the stack measured on the two faces are different (Fig 3.12). In the $D_{2h}$ point group of the TCNQF$_4$ molecule the $b_{1u}$ and $b_{2u}$ modes have the same symmetry of the long and the short in-plane axes, respectively. Thus, from the relative intensities of these modes we can determine the molecular orientation respect to the $x$ and $z$ direction of the adopted reference system.

The spectrum measured with the light polarized along $x$ is dominated by the TCNQF$_4$ $b_{2u}$ modes, while the $z$ polarized spectrum displays the TCNQF$_4$ $b_{1u}$ modes, together with many N-TMB bands (Fig 3.12). Thus, the short and the long TCNQF$_4$ axes have a major projection along the $x$ and $z$ directions, respectively.

The charge sensitive TCNQF$_4$ ring C=C stretching vibration $b_{2u}\nu_{33}$ is redshifted to 1539 cm$^{-1}$ , indicating $\rho$=0.95. Also the frequency shifts of the two C≡N stretching bands $b_{2u}\nu_{32}$ and $b_{1u}\nu_{19}$, found at 2178 and 2196 cm$^{-1}$ respectively, correspond to a ionicity value of 0.86 and 0.94. This means that this compound is fully ionic.

In the case of the thin Phase II platelets, the IR measurements were possible on the extended $xy$ plane only. The $x$ polarized spectrum is very similar to the corresponding spectrum of Phase I. The strong $b_{2u}\nu_{32}$, $b_{2u}\nu_{33}$ and $\nu_{36}$ bands are clearly visible at 2181, 1541 and 962 cm$^{-1}$ [49]. Therefore, in Phase II also the short molecular axes are parallel to $x$. The $b_{2u}\nu_{33}$ frequency shift respect to the neutral TCNQF$_4$ molecule, -57 cm$^{-1}$ , corresponds to $\rho$=0.92. In addition, based on to the C≡N stretching bands $b_{2u}\nu_{32}$ and $b_{1u}\nu_{19}$, we find $\rho$=0.79 and 0.85 respectively. Thus, also N-TMB-TCNQF$_4$ Phase II is ionic. In both phases the charge sensitive bands are not split, meaning that the ionicity is the same for all the molecules. Thus, the stoichiometry is likely 1:1 in both compounds.

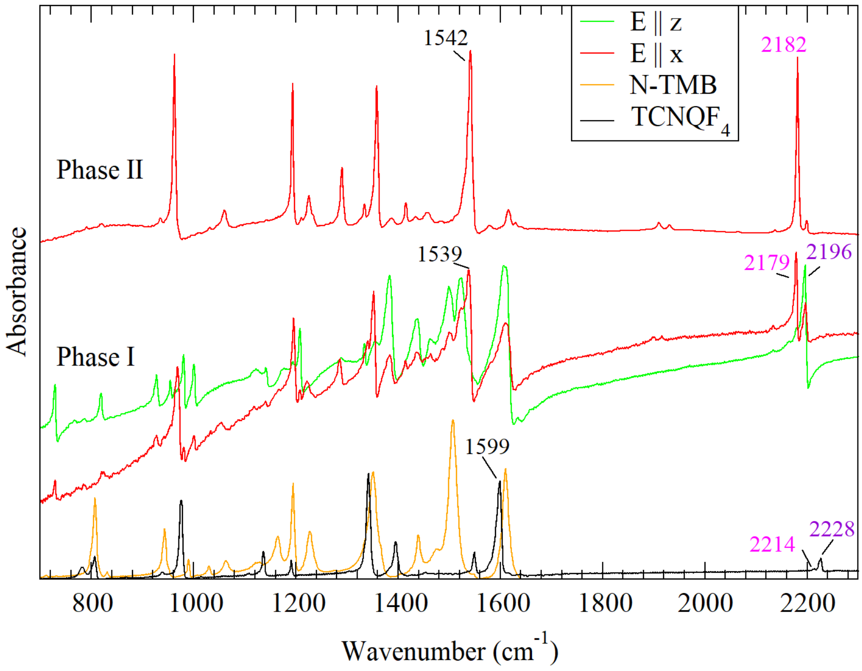

Figure 3.12: *IR spectra of the two N-TMB-TCNQF$_4$ phases, polarized perpendicular to the stack direction y. The spectra of the reagents are shown for comparison and the spectra of each phase are offset for clarity.*

The high ionicity values are consistent with the blue color of the crystals. Indeed, the lowest energy absorption of the TCNQF$_4^-$ radical ion lies between 650 and 900 nm [54]. The associated transition dipole moment, having $b_{1u}$ symmetry, is aligned to the long molecular axis. Also the N-TMB$^+$ cation shows an electronic transition in the same spectral range, polarized along its long molecular axis.

According to the molecular orientation inferred from the IR spectra, the projection of these dipoles would be zero along $x$ and maximum along $z$. This explains both the pale color observed in transmission mode with the light polarized along $x$ and the high reflectivity on the $xz$ plane. Finally, the blue color seen with the $y$ polarization suggests that the molecular planes are tilted respect to the stack direction.

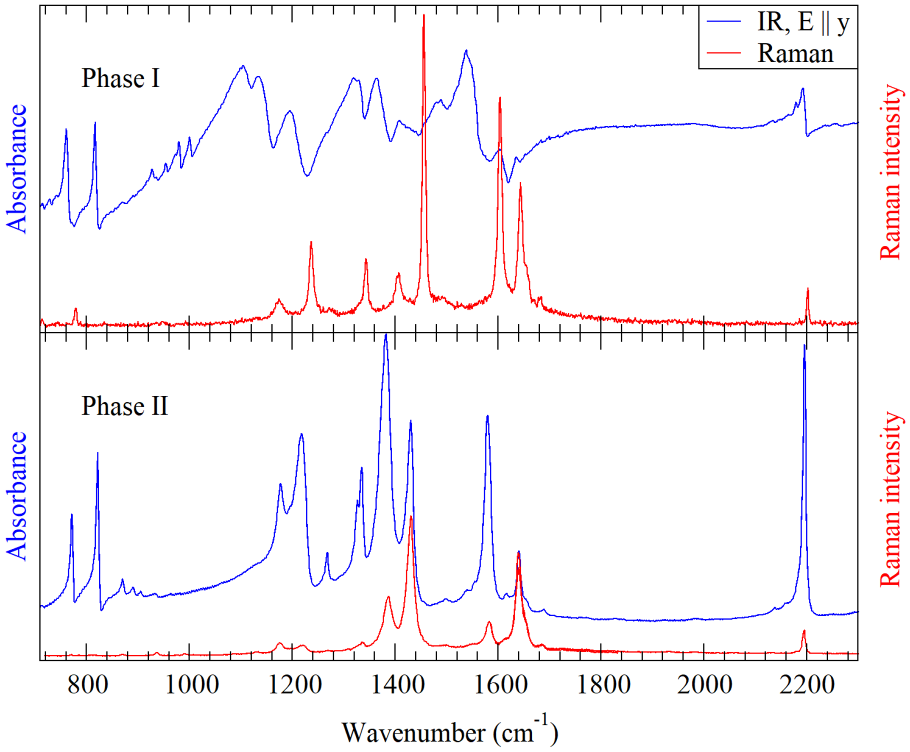

Figure 3.13: *Comparison between the IR spectra polarized along the stack and the Raman spectra: Phase I (upper panel) and Phase II (lower panel).*

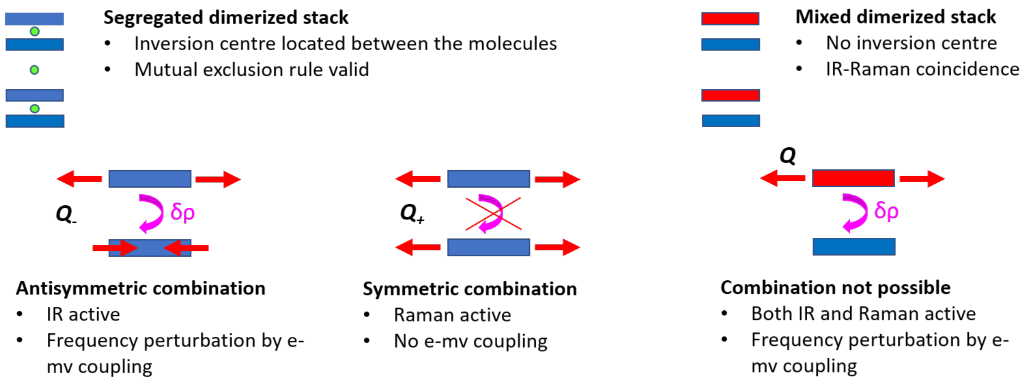

Figure 3.14: *e-mv coupling perturbation of the totally symmetric intramolecular vibrations in segregated and mixed dimerized stacks.*

The parallel polarized mid-IR spectrum of Phase I is dominated by strong absorptions (Fig 3.13, upper panel). However, the frequencies of these bands do not correspond to the Raman frequencies, but are lowered with respect to them. This would be consistent with a dimerized segregated stack.

Dimerized segregated stacks are composed of dimers of identical radical ions. Therefore, it is possible to define a symmetric (in phase) and an antisymmetric (out of phase) combination of the totally symmetric modes of the isolated ions. The antisymmetric one, having the same symmetry of the CT excitation, is coupled to it, while the symmetric one is not (Fig 3.14, left). As a result, the antisymmetric combination mode is IR active, with a frequency lowered respect to the symmetric counterpart, that is Raman active [26, 55]. Differently from mixed dimerized stacks, segregated dimerized stacks maintain the inversion centre, located between the ions. Consequently, the mutual exclusion rule is still valid.

On the contrary, in mixed stacks it is not possible to combine the totally symmetric vibrations of different molecules (Fig 3.14, right). For this reason these modes are both IR and Raman active, with the same frequency, lowered by the e-mv interaction. This is the case of case of Phase II: the IR spectra polarized along the stack display many strong bands (Fig 3.13, lower panel) at the same frequencies of the totally symmetric Raman bands.

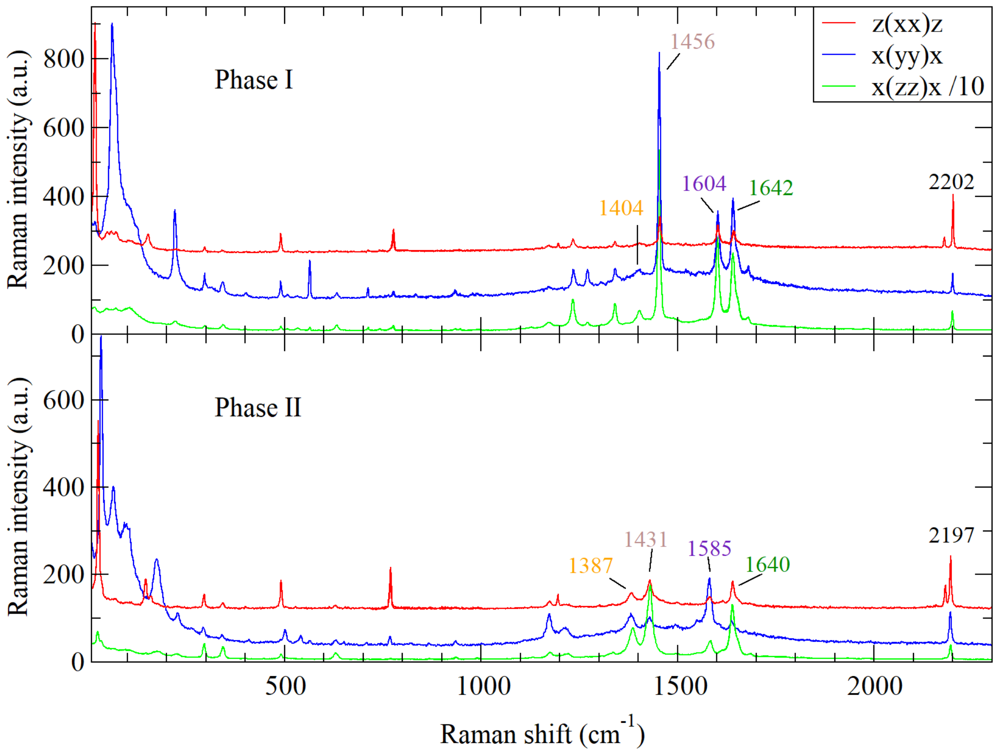

Figure 3.15: *Comparison between the polarized Raman spectra of the two N-TMB-TCNQF$_4$ crystal phases. For the sake of clarity, the three polarizations are offset and both the zz ones, enhanced by resonance, have been divided by 10.*

Furthermore, all the totally symmetric Raman bands are redshifted in Phase II with respect to the corresponding modes in Phase I (Fig 3.15). This effect is stronger for the most coupled bands, as TCNQF$_4$ $a_g\nu_3$, observed at 1456 and 1431 cm$^{-1}$ in Phases I and II. As in the case of the polarized IR spectra of the two phases, the Raman spectra follow the same pattern. The totally symmetric intramolecular vibrations are very weak with the $xx$ polarization and are amplified an order of magnitude with the $zz$ polarization. This is a clear resonance effect, since the 633 nm exciting line is close to the absorptions of both radical ions. Indeed, the same intensity enhancement was observed also in the case of the fully ionic analogue TMB-TCNQF$_4$. A more detailed comparison between the two compounds is presented in the Appendix, Section A.1. Differently, the $yy$ polarized spectra are amplified at low frequencies, as observed in most dimerized CT crystals.

As expected, the main differences between the spectra of the two polymorphs are observed in the lattice phonon range. In the case of Phase I, six phonons are found below 200 cm$^{-1}$ , active with both parallel and crossed polarization on both $yx$ and $yz$ planes. This suggests that the unit cell symmetry is triclinic. 11 phonons are present instead in the spectra of Phase II (Fig 3.16). Four of them are visible only in the $xy$ polarized spectrum and not on the $yz$ one. This would be consistent with a monoclinic unit cell, with the twofold axis parallel to $x$. Also the rectangular shape of the extended crystal face supports this hypothesis.

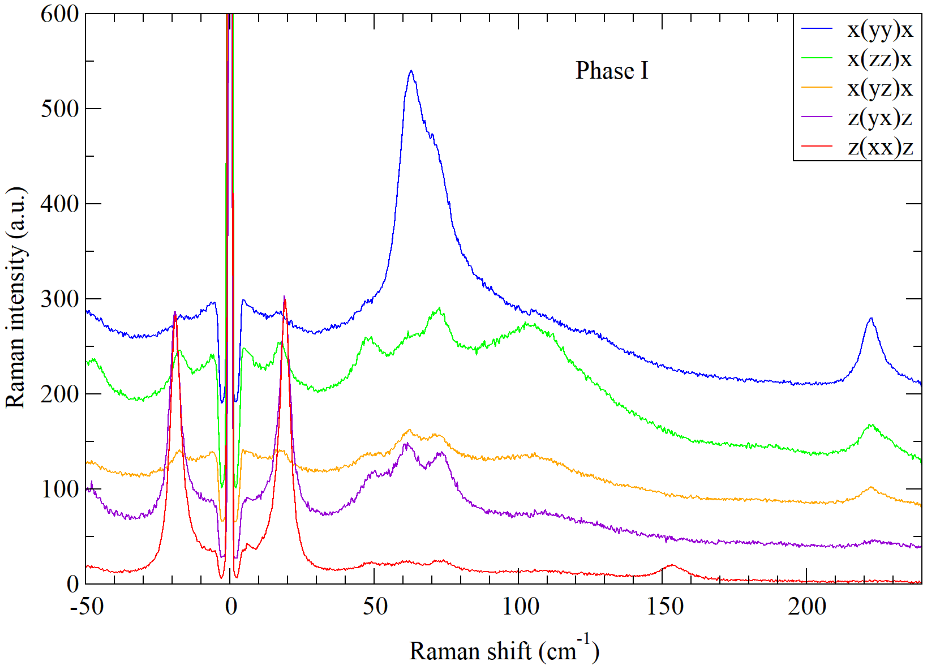

Figure 3.16: *Polarized low frequency Raman spectra of N-TMB-TCNQF*$_4$*, Phase I. The yz and zz polarized spectra are offset for clarity.*

However, some common features exist between the spectra of the two phases. The $xx$ polarized spectra display a single narrow band around 20 cm$^{-1}$ . Then, the $zz$

polarized ones are characterized by broad and overlapped bands, covering the whole 5-200 cm$^{-1}$ range, that indicate structural disorder present along the $z$ direction. The most likely explanation is that the N-TMB axial N-(CH$_3$)$_2$ groups cause disorder along the $z$ direction, selectively. The same spectral pattern was indeed found in the low frequency Raman spectra of the ionic mixed stack crystal TMPD-TCNQ (Fig 4.6), whose donor also presents axial N-(CH$_3$)$_2$ groups. To summarize, the intermolecular interactions have similar strength and directionality in the two N-TMB-TCNQF$_4$ polymorphs, despite their different stack motif.

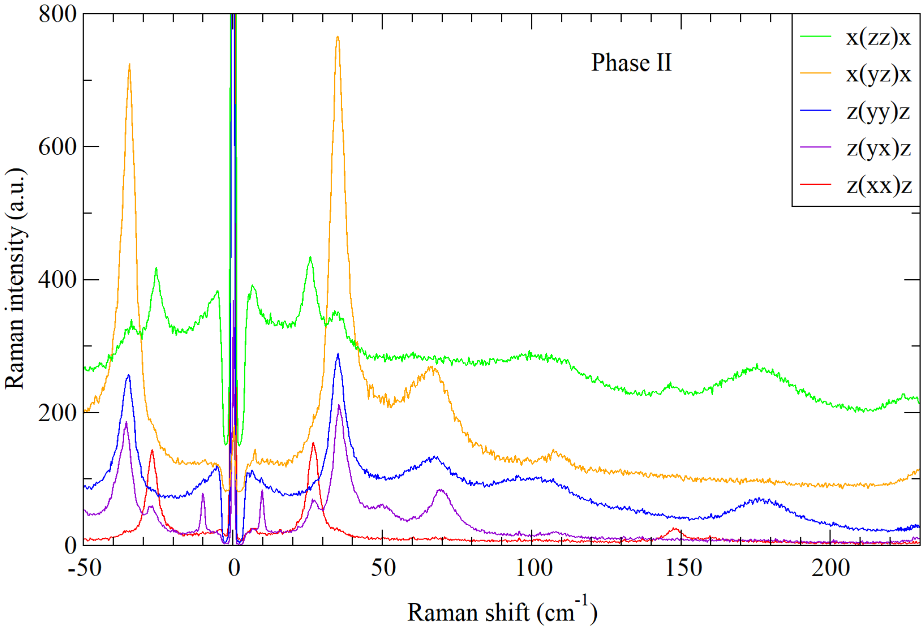

Figure 3.17: *Polarized low frequency Raman spectra of N-TMB-TCNQF$_4$, Phase II. The spectra are offset for clarity.*

Preliminary low temperature Raman measurements found that neither of the polymorphs undergoes apparent temperature induced phase transitions on cooling down to 80 K. Their temperature dependent low frequency spectra, $yy$ polarized, are shown in Fig 3.18. Both display a strong band narrowing and a slight frequency hardening on cooling. No new bands appear, even with the increased spectral resolution.

The two polymorphs have different thermal stabilities: decomposition occurs at around 390 K in Phase I and 440 K in Phase II. Interconversion between the two polymorphs was never observed, consistently with their proposed stack motifs. A phase transformation from a segregated to a mixed stack would indeed be very difficult.

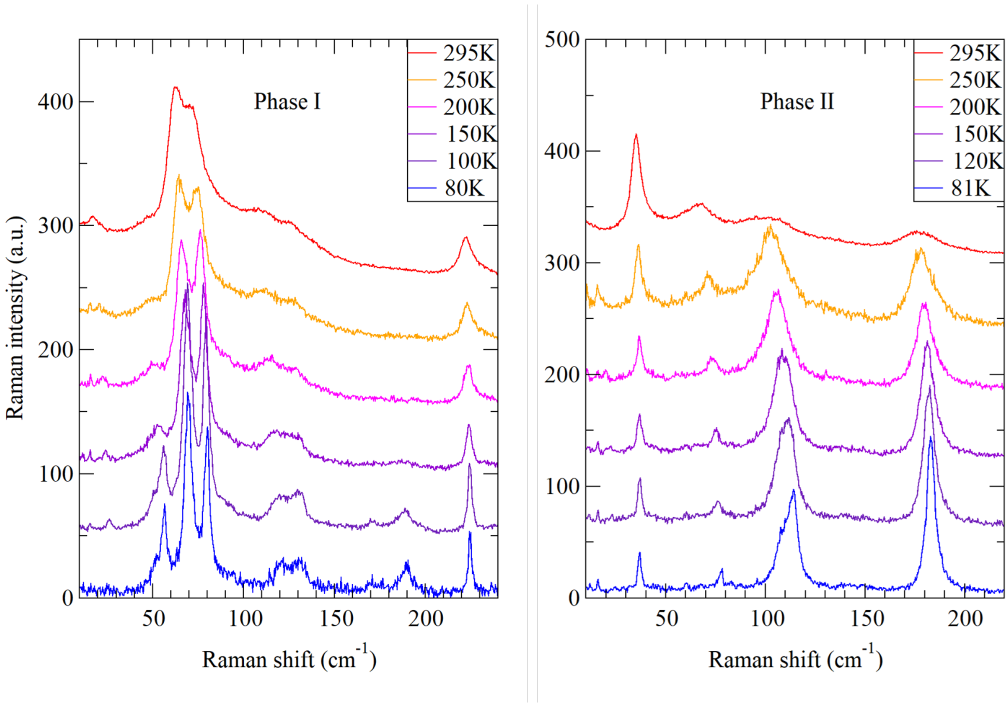

Figure 3.18: *Low temperature Raman spectra of N-TMB-TCNQF$_4$ in the lattice phonon range, Phase I (left) and Phase II (right). The exciting and scattered light are both polarized along the stack direction y. The spectra are offset for clarity.*

## 3.4 Conclusions

The N,N,N',N'-Tetramethylbenzidine-TCNQF$_x$ CT cocrystals have been synthesized for the first time and characterized by polarized optical spectroscopy on single crystals. According to the spectra, these crystals, having 1:1 stoichiometry, display different degrees of ionicity and stack symmetries, exploring a wide phase space among CT crystals.

N-TMB-TCNQ and N-TMB-TCNQF$_2$ are both neutral, with mixed stack motif. While in the former the stack is regular, in the latter the presence of weak vibronic IR bands suggests that the stack is dimerized or affected by disorder. Both the N-TMB-TCNQF$_4$ polymorphs are ionic and dimerized.

Interestingly, N-TMB-TCNQF$_4$ grows in two polymorph phases. Their spectroscopic data point towards two different stack motifs: segregated in Phase I and mixed in Phase II. This kind of polymorphism is rare: the only reported examples are TMTSF-TCNQ [56, 57], BEDT-TTF-TCNQ [58, 59] and TTF-CA [24, 60]. However, in both CT systems the two polymorph phases have also a different ionicity. While the segregated stack phases are ionic, the mixed stack ones are neutral, due to the inefficient overlap between the frontier orbitals of the two molecules. On the contrary, both phases are ionic in this case, with $\rho$=0.9. Indeed, the N-TMB HOMO and the TCNQF$_4$ LUMO have the same symmetry respect to the inversion centers of the corresponding molecules. Thus, the overlap would be effective with both stack motifs.

According to the previous studies, analogue ionic systems like TMPD-TCNQ [61], TMB-TCNQF$_4$ [62] and TMPD-TCNQF$_4$ [55] do not show such polymorphic behavior. The stack motif is mixed in the first two systems and segregated in the third one. Thus, also these systems might present different polymorph phases depending on the growth conditions[1].

The structural determination and the low temperature spectroscopic measurements, now in progress, will soon complete the present study.

---

[1] TMPD-TCNQ and TMB-TCNQF$_4$ are presented in Chapter 4 and Appendix, Section A.1 for other purposes. The two materials were obtained following the procedures described in the literature, without finding any polymorphs.

# Chapter 4

# TMPD-TCNQ revisited: regular or dimerized stack?

## 4.1 Introduction

Charge transfer crystals based on TCNQ and aromatic diamines were firstly investigated more than 50 years ago. A member of this family, the mixed stack ionic N,N,N',N'-Tetramethylphenylenediamine-TCNQ (TMPD-TCNQ) gave contradictory structural and spectroscopic data: X-ray diffraction found a regular stack while IR revealed the activation of the totally symmetric vibrations, the signature of a dimerized stack [63, 61]. Such disagreement was ascribed to the presence of some kind of disorder affecting the local molecular environment. It is known that the two techniques work on different spatial scales: XRD probes long range order, spectroscopy is sensitive to the molecular surroundings.

The following spectroscopic study extends the previous one performed on powders [61] with temperature dependent IR and Raman spectra measured on single crystals. The selective enhancement of the vibronic bands at low temperature supports that the stack is already dimerized at room temperature and such distortion is amplified on cooling.

## 4.2 Experimental

The TMPD-TCNQ crystal growth from solution presented the same difficulties of the N-TMB-TCNQF$_x$ series, due to precipitation. Good quality crystals were therefore obtained from toluene following the same procedure, described in Section 3.2. The crystals grew in a few days as dark needles or thick platelets, 1-2 mm long (Fig 4.1). In the same experimental conditions, acetonitrile solutions yielded a flaky precipitate of the same material. The identity of the product was confirmed by IR.

The crystals, having flat and good quality faces, were suitable for IR measurements in reflectance mode.

The Raman spectra were obtained exciting at 633 nm, keeping the power below 0.1 mW to reduce sample heating. In both IR and Raman measurements the light was polarized parallel or perpendicular to the stack direction.

The low temperature spectroscopic measurements were performed using a liquid nitrogen cryostat fitted under the IR and Raman microscopes.

## 4.3 Results and discussion

The identity of the product was confirmed by comparing the IR absorption spectrum of powdered crystals with the known spectrum of TMPD-TCNQ 1:1 [61]. The other known TMPD-TCNQ compound, of 1:2 stoichiometry, was never found with the chosen growth method [64]. According to the literature, the TMPD-TCNQ 1:1 complex crystallizes in the $C2/m$ space group, with Z=2. The molecules stack along the $c$ axis and are located on the inversion centers [63].

The crystals display needle or platelet morphology, with a strong tendency to twinning. Due to the crystal thickness, it was not possible to recognize the extinction directions by polarized optical microscopy. Thus, the stack axis $c$ was identified as the direction of maximum intensity of the CT band, occurring above 7000 cm$^{-1}$ . In the case of the needles, the stack axis is parallel to the elongation direction. On the contrary, in the twinned platelets the stack is parallel to the short side of each of the two symmetric parts (Fig 4.1).

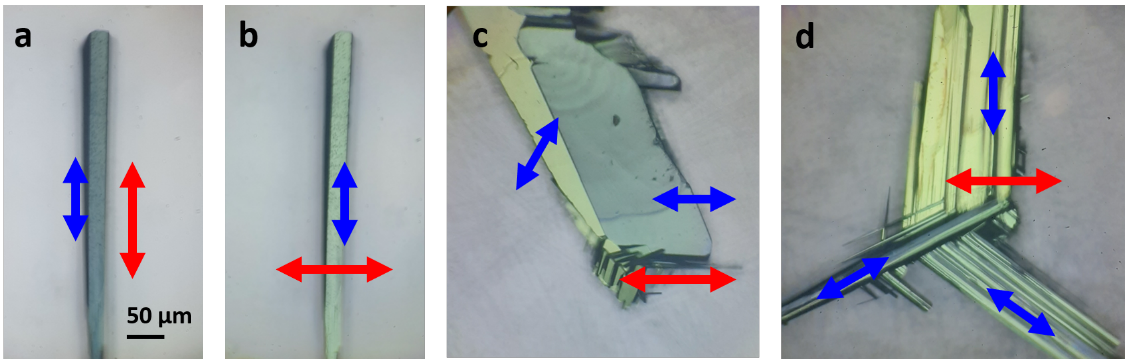

Figure 4.1: *Microscopic images of typical TMPD-TCNQ crystals under polarized light: needles (a and b) and platelets (c and d). The red arrows indicate the polarization of the reflected light, while the blue arrows indicate the stack direction. The platelets are twinned.*

The IR spectra polarized perpendicular to the stack are dominated by the in plane vibrations of TMPD and TCNQ. In the case of the needles, two groups of spectra having different relative band intensities were observed, corresponding to different orientations (Fig 4.2). In the first group only one TCNQ C≡N stretching band ($b_{1u}\nu_{19}$) is observed, while in the other group the C≡N bands are two ($b_{2u}\nu_{33}$ and $b_{1u}\nu_{19}$). According to the relative intensities of the bands, the two faces are parallel to the 010 and 110 planes (Fig 4.3). The platelets always gave spectra corresponding to 010 orientation. Indeed, these faces are predicted to be the most extended ones by BFDH calculations and the previous works found preferred 010 orientation [63, 65].

The ionicity is estimated according to the frequency shift of the TCNQ antysimmetric ring stretching, $b_{1u}\nu_{20}$. This band is found at 1503 cm$^{-1}$ , corresponding to a ionicity value $\rho \simeq 1$. Also the large frequency shifts of the two C≡N stretching modes are consistent, being redshifted to 2186 and 2163 W respect to 2228 cm$^{-1}$ in the neutral TCNQ molecule. The full TMPD-TCNQ ionicity, compared to the small value of N-TMB-TCNQ (Chapter 3), is due to the much lower ionization potential of TMPD [66].

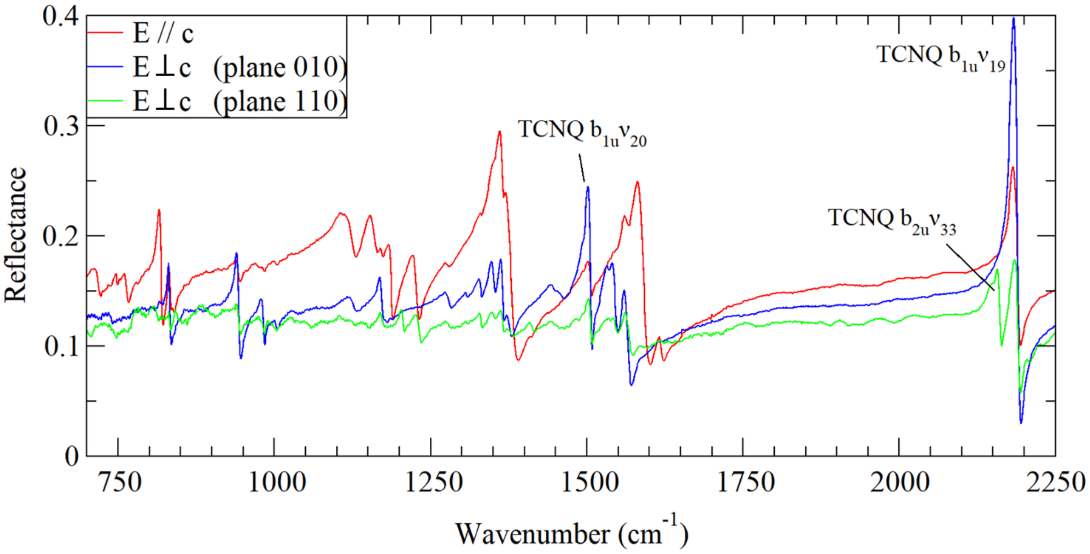

Figure 4.2: *IR reflectance spectra of TMPD-TCNQ needles, recorded on two different faces and polarized parallel or perpendicular to the stack axis c*

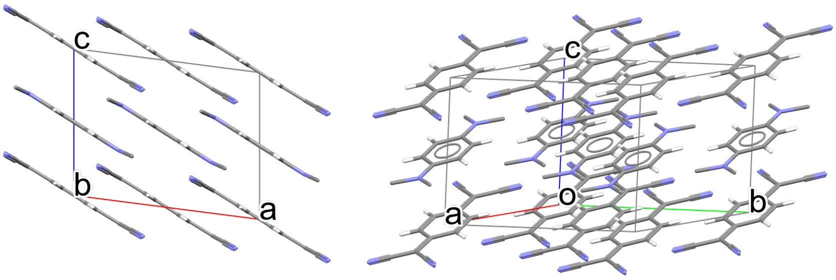

Figure 4.3: *TMPD-TCNQ unit cell viewed along* 010 *(left) and* 110 *(right) directions. The methyl hydrogens were not determined in the reported structure (Ref [63], CCDC refcode QMEPHE).*

The spectra polarized along the stack direction are dominated by many strong bands, at the same frequencies of the totally symmetric vibrations of TMPD and TCNQ, also present in the Raman spectra (Fig 4.4). The IR-Raman coincidence was previously noted in Ref. [61], studying a powdered material. The present polarized spectra confirm that such bands have indeed vibronic origin, being polarized along the stack. This is the signature of inversion symmetry breaking along this direction, due to dimerization or disorder. A likely source of disorder are the N-$(CH_3)_2$ groups, due to their large conformational freedom. Anyway, the strong intensity of the vibronic bands compared to the other IR active modes fits better with a dimerized stack than with a local disorder.

In the same polarization the out-of-plane vibrations of the two molecules are also present around 800 cm$^{-1}$ . Small projections of the $b_{1u}$ bands of TCNQ and the $b_u$ ones of TMPD are also visible due to the inclination of the molecular planes respect to the stack direction.

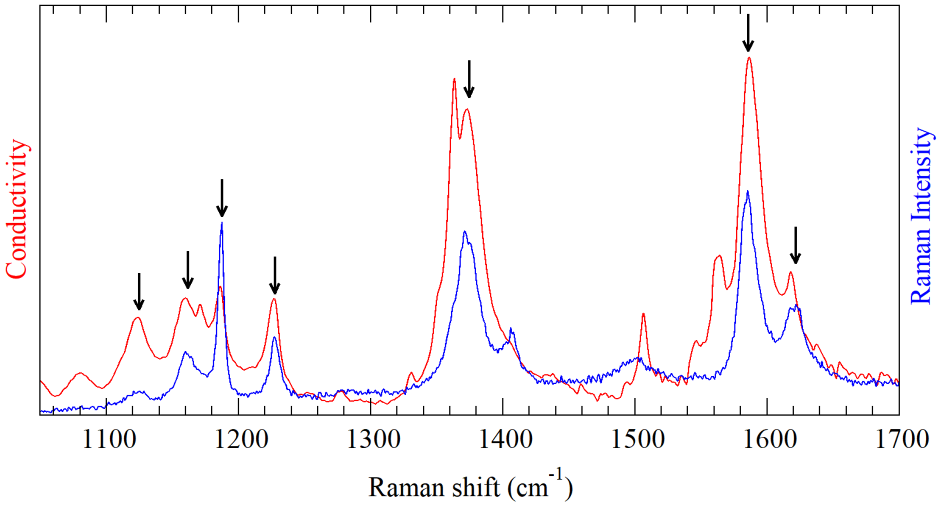

Figure 4.4: *Comparison between the IR spectrum polarized along the stack and the Raman spectrum. The common bands are marked with black arrows. The IR conductivity spectrum was obtained as the Kramers Krönig transformation of the reflectivity data.*

The polarized Raman spectra were also measured on the 100 (*bc*) plane, containing the short molecular axis, to better understand the crystal packing. The intensity is enhanced with the $a^*a^*$ polarization respect to the *bb* one in the 1000-2220 cm$^{-1}$ range (Fig 4.5). Such amplification is clearly a resonance effect, as in the case of N-TMB-TCNQF$_4$ and N-TMB-TCNQF$_4$ (Fig 3.15 and A.3). Indeed, the lowest energy transitions of both radical ions are long axis polarized [65].

At lower frequencies, also the phonon band pattern reflects the anisotropy between the two crystal planes (Fig 4.6). On the 010 (*ac*) plane the bands are very broad in both *cc* and $a^*a^*$ polarizations. On the contrary, the *bb* polarized spectrum displays much narrower phonon bands. This means that some kind of disorder is present along the both the stack direction *c* and along $a^*$, nearly aligned to the long molecular axis. Indeed, the TMPD N-$(CH_3)_2$ groups, suspected of inducing disorder, point towards these two directions. Furthermore, the observed phonons do not match the spectral predictions based on the reported space group, $C2/m$. In that case, six phonon bands would be expected, $2A_g + 4B_g$, corresponding to the librations of the two molecules contained in the primitive unit cell. Differently, 6 phonons with parallel polarization ($A_g$ symmetry) are observed, suggesting that the symmetry is lower than the reported one.

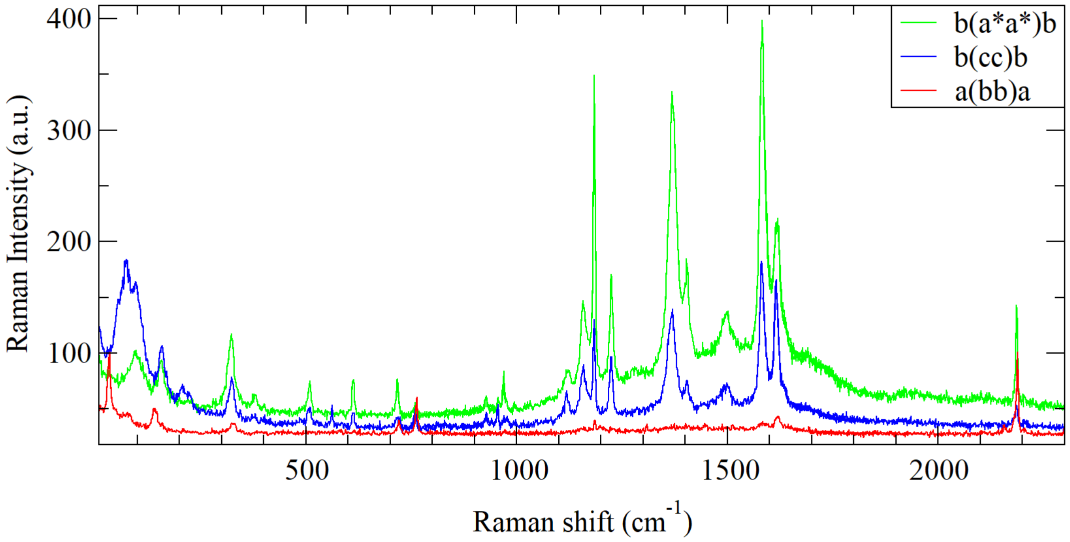

Figure 4.5: *Polarized extended Raman spectra of TMPD-TCNQ.*

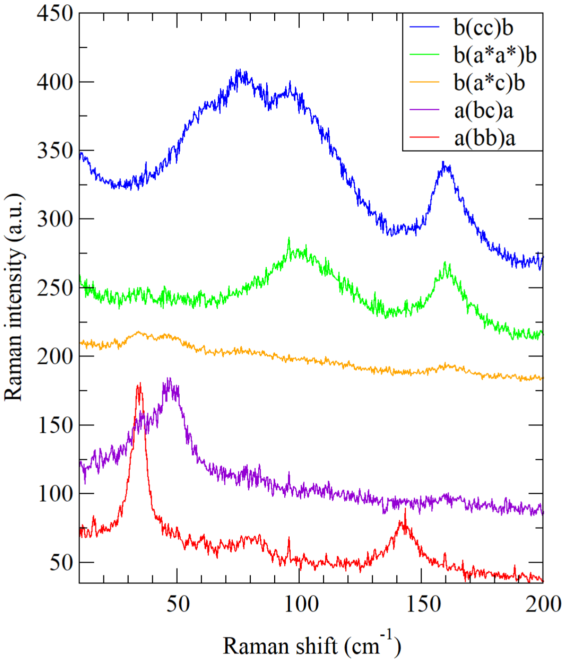

Figure 4.6: *Polarized low frequency Raman spectra of TMPD-TCNQ. The spectra are offset for clarity.*

No apparent phase transition is observed on cooling down the crystals to 80 K. However, the IR spectra polarized along the stack display a large intensity enhancement of the vibronic bands (Fig 4.7). On the contrary, the spectra polarized perpendicular to the stack do not show any change in the intensity or frequency of the bands, indicating that the ionicity remains close to 1. Similarly, the out-of plane ungerade vibrations, intrinsically IR active with polarization along the stack, are not enhanced at low temperature (Fig 4.8, left panel). The CT transition frequency remains constant (Fig 4.8, right panel). Thus, the e-mv coupled vibrations are amplified selectively.

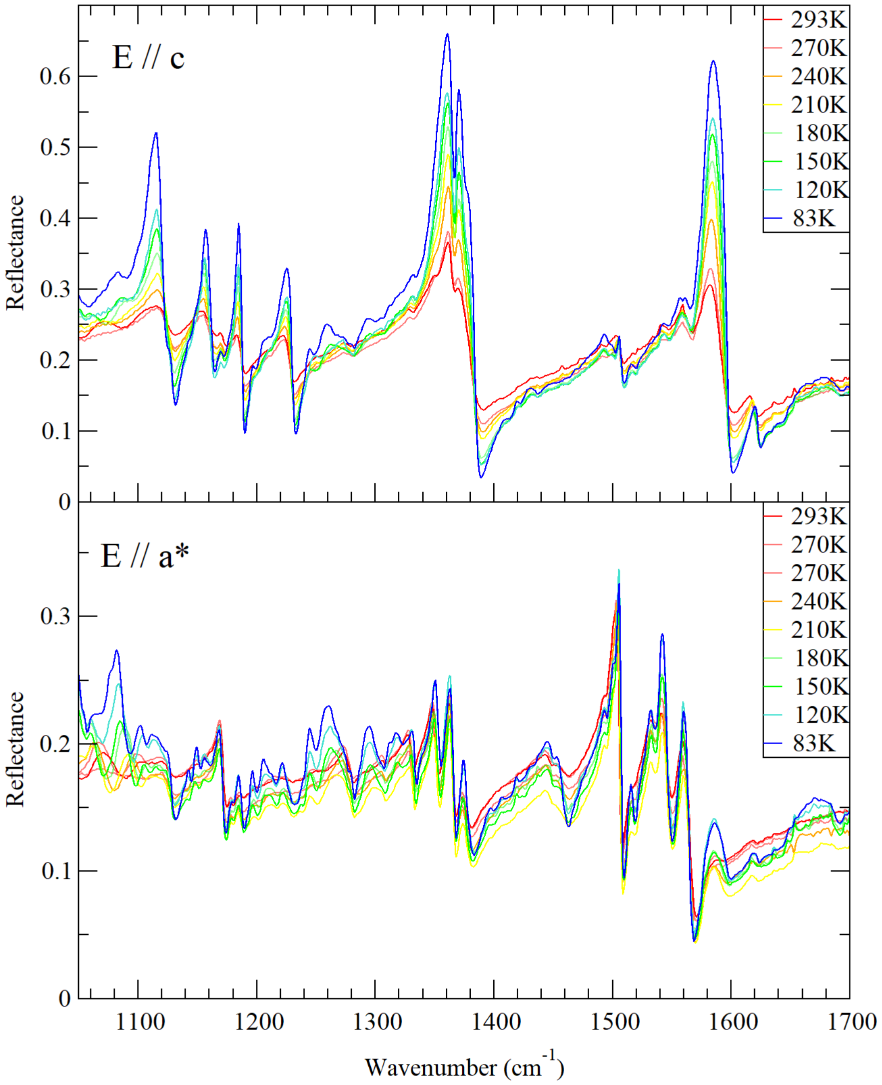

Figure 4.7: *Low temperature IR reflectivity spectra of TMPD-TCNQ.*

The thermal changes of the Raman spectra are very small. At high frequencies, two totally symmetric bands of TCNQ, $a_g\nu_3$ and $\nu_4$, are redshifted while two TMPD bands ($a_g\nu_2$ and $\nu_3$) are slightly blueshifted (Fig 4.9). At low frequency, the strong *cc* polarized bands display a typical frequency hardening and a slight narrowing. Despite the increased resolution, the number of bands is unchanged at 80 K (Fig 4.10). Anyway, their width is always above 10 cm$^{-1}$ , demonstrating residual structural disorder.

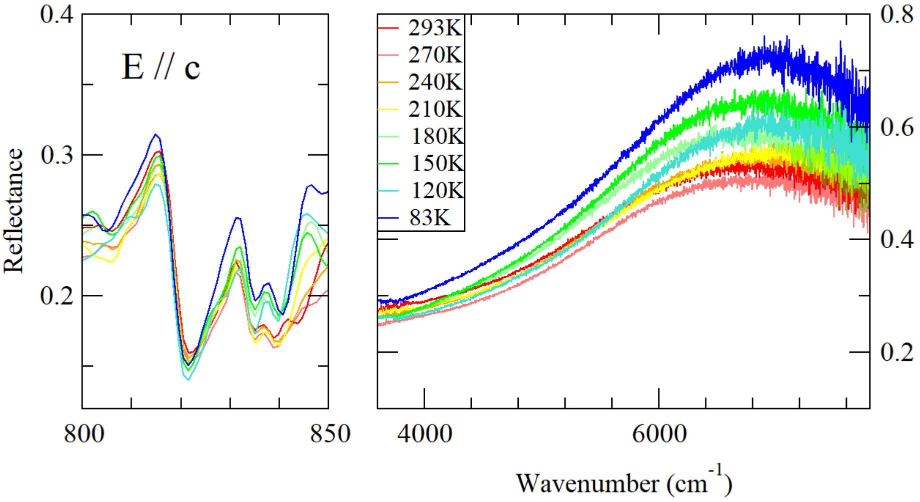

Figure 4.8: *Low temperature IR reflectivity spectra of TMPD-TCNQ: out-of plane modes (left panel) and CT band (right panel).*

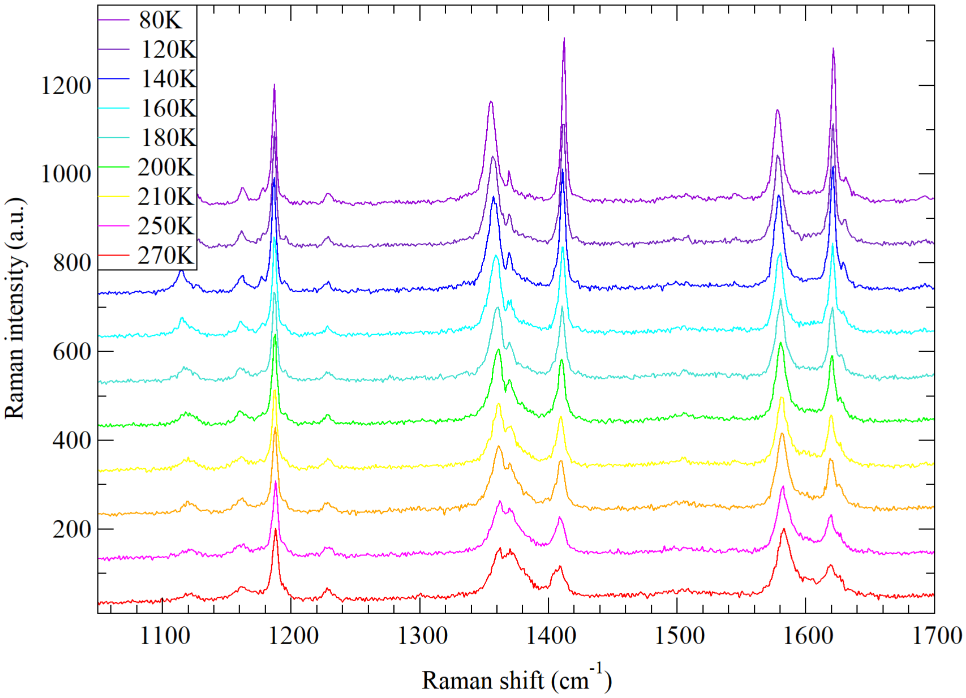

Figure 4.9: *Low temperature Raman spectra of TMPD-TCNQ. The spectra are offset for clarity.*

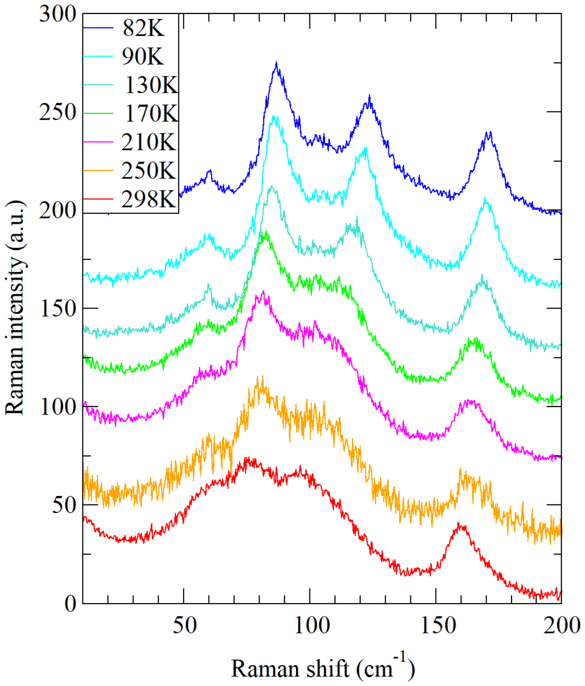

Figure 4.10: *Low temperature Raman spectra of TMPD-TCNQ, in the low frequency range. Polarization: cc. The spectra are offset for clarity.*

The presence of vibronic bands always indicates the absence of inversion symmetry along the stack, at least at a local scale. This might be either long-range dimerization or local disorder. In the latter case, vibrational spectroscopy and XRD might give inconsistent results, as spectroscopy probes the molecular environment while XRD probes long range order.

For instance, the mixed regular stack crystal ClMePD-DMDCNQI displays weak vibronic bands in the neutral phase at room temperature, that continuously increase in intensity on cooling [67]. The low temperature XRD analysis did not detect any symmetry breaking along the stack [53]. Thus, the vibronic activation of the totally symmetric modes was ascribed to the disorder induced by the polar donor molecule. Differently, the intensity increase was due to the ionicity increase towards $\rho$=0.5. But this is clearly not the case of TMPD-TCNQ, as the ionicity is unchanged.

Another interesting comparison can be made between TMPD-TCNQ and the mixed stack system TMB-TCNQF$_4$. Both crystals are almost fully ionic and were found to have regular stack by XRD but show vibronic IR absorptions. TMB-TCNQF$_4$ structure was recently revisited, finding a dimerized stack and an order-disorder transition [62]. The local stack distortion changed into a long range antiferroelectric arrangement of dimerized stacks, but with just a slightly larger dimerization amplitude. Such structural rearrangement resulted in much narrower phonon bands and unchanged IR vibronic intensity. On the contrary, in TMPD-TCNQ the phonon bandwidth changes slightly on cooling, while the vibronic intensities increase.

It is known that the vibronic intensity increases with the degree of dimerization, keeping all the other microscopic parameters constant, i. e. ionicity, CT transition energy... [26]. Thus, only a larger local structural distortion can explain the observed TMPD-TCNQ behavior. The two crystals start from the same condition but evolve in different ways. TMB-TCNQ$F_4$ is both dimerized and affected by long range disorder, that disappears on cooling. Also TMPD-TCNQ is disordered and likely dimerized at room temperature, but cooling results in a larger distortion instead, without establishing long range order. A dimerized stack is indeed expected in TMPD-TCNQ: most ionic stacks are distorted or undergo a dimerization transition on cooling, being intrinsically subject to spin-Peierls instability. Also the reported magnetic susceptibility data are not consistent with a regular stack chain [68].

## 4.4 Conclusions

This work completes the previous low temperature studies on TMPD-TCNQ with the polarized vibrational spectra, also in the lattice phonon frequency range. Thus, the temperature evolution of ionicity, stack symmetry and crystal packing were followed separately.

TMPD-TCNQ is fully ionic at all the temperatures and the Raman spectra do not display any significant variation, both in the band frequencies and widths. The only remarkable evolution is the continuous IR intensity increase of the totally symmetric modes, with polarization along the stack.

Combining these data, many possible explanations for such behavior have been excluded. The most plausible hypothesis is the increase of the dimerization amplitude on cooling. A detailed structural analysis would clarify this issue, as done in the case of TMB-TCNQ$F_4$ [62].

# Chapter 5

# Polymorphism and solvate phases of the PCBM organic semiconductor

## 5.1 Introduction

The organic semiconductor [6,6]-phenyl-$C_{61}$-butyric acid methyl ester (PCBM), a chemically modified fullerene, has been widely used as an electron acceptor for organic solar cells. The side chain increases the solubility in organic solvents and processability but makes the crystallization difficult [69].

Since the electronic properties of PCBM strongly depend on the molecular packing, the knowledge of PCBM polymorphism is needed. It is known that PCBM crystallization is influenced by solvents, substrates and temperature. Three different crystal structures are known: two solvate phases [70] and a solvent-free one [71, 72, 73]. Another phase with hexagonal symmetry was also reported, whose structure is unknown [74, 75].

The aim of this work is the characterization of the PCBM crystalline phases grown from chlorobenzene or 1,2-dichlorobenzene solution on silica or Si substrates. Two known phases were identified: the 1,2-dichlorobenzene solvate and a solvent free phase. A third unknown phase was also found, probably solvent free.

## 5.2 Experimental

PCBM crystals grown from dichlorobenzene (DCB) or chlorobenzene (CB) solutions, on Si or quartz glass substrates were provided by Prof. F. Cacialli, from University College of London.

The Raman spectra were recorded with the Horiba Raman microscope, keeping the laser power to 0.1 mW to avoid sample heating. For the low frequency spectra, the 633 nm exciting line and a diffraction grating with 1800 grooves/mm were used. With this configuration the lattice phonons were accessible down to 4 cm$^{-1}$ thanks to the ULF Bragg filter. However, the intermolecular vibrations at higher frequencies were hidden by strong fluorescence with this exciting line. For this reason, the 532 nm line was chosen instead to measure the extended Raman spectra, using a grating with 600 grooves/mm.

The IR spectra were measured on single crystals or powders, depending on the crystal size and adhesion to the substrate. Single crystals of the DCB solvate phase were heated to 360 K in nitrogen atmosphere to remove the solvent. Then, the structural order of the resulting material was investigated by polarized IR and Raman spectroscopy.

## 5.3 Results and discussion

The observed crystal morphologies and sizes were independent of the substrate material and depended only on the solvent chosen for the crystal growth. Using the same solvent, silicon and silica substrates yielded very similar crystals.

### 5.3.1 Phases obtained from DCB solution

The rhombus-shaped platelets obtained from DCB are very similar to the PCBM-DCB 1:1 solvate crystals described in [71], whose extended face is parallel to the $(10\bar{1})$ plane (Fig 5.1). This phase, whose space group is $P2_1/n$, has a layered structure, containing PCBM and solvent rich layers alternating along the $(10\bar{1})$ direction.

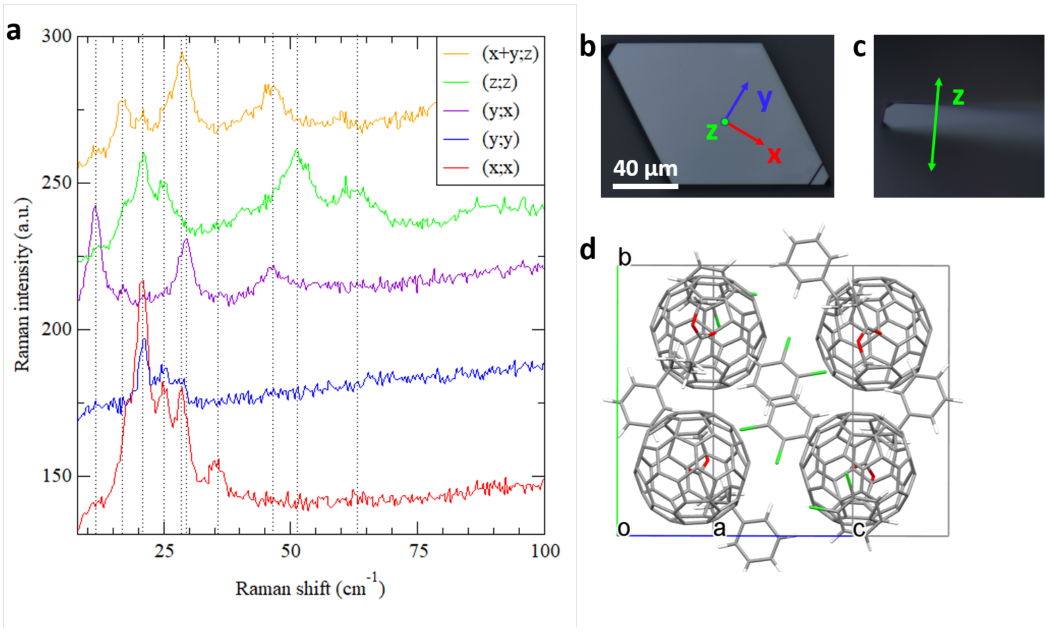

Figure 5.1: *Polarized low frequency Raman spectra of PCBM crystals grown from DCB (a). Microscopic images of crystals laying on the extended face (b), parallel to the* $(10\bar{1})$ *plane, and on a side face (c). Crystal structure of PCBM-DCB viewed along the* $(10\bar{1})$ *direction (CCDC refcode EKOZOT).*

Although most crystals strongly adhered to the substrate, it was possible to remove some of them without damage. Viewing perpendicular to the lamellar plane, the extinction directions, named $x$ and $y$, coincide with the diagonals of the rhombus. The orientation relationship between the in-plane extinction directions and the crystallographic axes could be clarified by polarized IR spectroscopy (Fig 5.2). To do this, the unit cell is viewed along the 1;0;-1 direction, perpendicular to the extended face and parallel to the $z$ axis of the adopted reference system. The only IR active mode with a well defined polarization should be the C=O stretching, found at 1738 cm$^{-1}$ and polarized mainly along the bond axis. Since this band is completely polarized along $y$ and the C=O bond axis is nearly perpendicular to the $b$ direction, $x$ likely coincides with the $b$ axis. Furthermore, all the solvent bands are present in the IR spectra, confirming that the crystals belong to the DCB solvate phase.

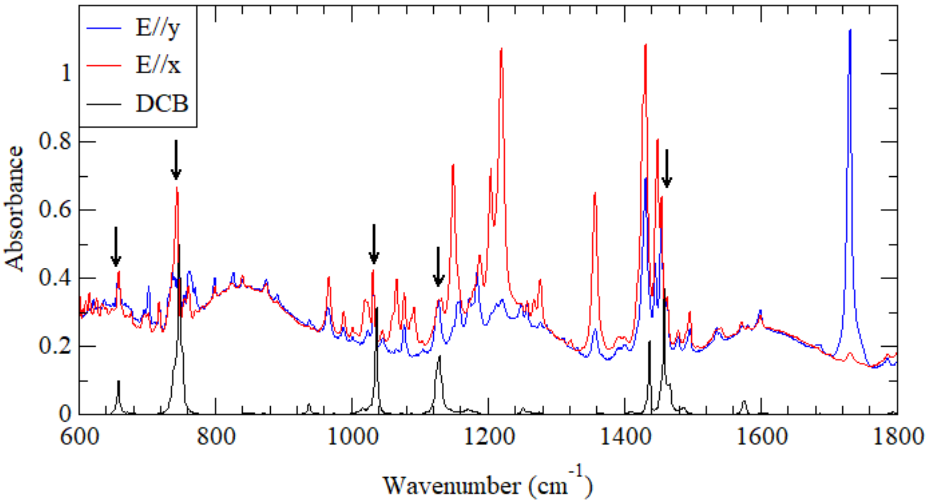

Figure 5.2: *Polarized IR spectra of a PCBM crystal grown from DCB, recorded on the extended face. The IR spectrum of the solvent, reproduced from the NIST database, is also reported and the solvent bands are marked with black arrows.*

The low frequency polarized Raman spectra are consistent with this crystal structure and orientation (Fig 5.1). Firstly, the presence of phonons with crossed polarization agrees with the monoclinic symmetry and the 1;0;-1 orientation, on a plane containing the $b$ axis. More lattice phonons can be detected measuring on the few vertically oriented crystals found on the substrate. Overall, 9 phonon bands can be resolved below 70 cm$^{-1}$ . It is sensible to assume that such low frequency phonons involve motions of the large PCBM molecules rather than the DCB ones. Indeed, in the $P2_1/n$ space group, with $Z$ =4, 12 Raman active phonons due to PCBM motions are expected, whose symmetry species are 6 $A_g$ + 6 $B_g$.

At higher frequencies, using the 633 nm exciting line the Raman spectrum is completely covered by a broad fluorescence band, occurring in the 600-800 nm range [76]. Differently, with 532 nm excitation the Raman spectrum is completely visible, as it occurs at shorter wavelengths (Fig 5.3). Furthermore, some bands are enhanced by resonance, as the exciting wavelength matches the lowest energy absorption of PCBM [77]. The strongest Raman peak, occurring at 1464 cm$^{-1}$ , is assigned to the fullerene pentagonal pinch mode [78]. The solvent bands are not visible, probably due to the small DCB Raman cross section compared to the fullerene one.

PCBM-DCB does not show any phase transition on cooling down to 80 K. Thus, low temperatures can be used to improve the spectral resolution thanks to narrower phonon bands. Also the fluorescence band becomes narrower on cooling, reducing the background with 633 nm excitation. This temperature behavior is common to all the PCBM phases described in this chapter.

The solvent molecules can be removed by heating the solvate crystals to 360 K. The sample shape is maintained during the transformation and on further cooling to room temperature. However, the IR and Raman spectra of the heated material are completely depolarized (Fig 5.4 and 5.5). Moreover, the Raman spectra show a very broad feature at low frequency, without any recognizable phonon band. These facts indicate structural disorder, i. e. amorphization following the solvent removal. Since the heated material was cooled to room temperature without annealing, poor crystallinity is expected. These results agree with the Molecular Dynamics simulations, that predicted a disordered structure after solvent removal [79]. The relative intensities of the bands in the IR spectra are different in the heated material. This fact is probably due to a change in the 3D orientation of the molecules rather than chemical degradation. Indeed, PCBM is known to be stable at least up to 200 °C [80]. Furthermore, both the intramolecular Raman bands and the fluorescence background are unchanged, excluding any decomposition reaction, even on the surface.

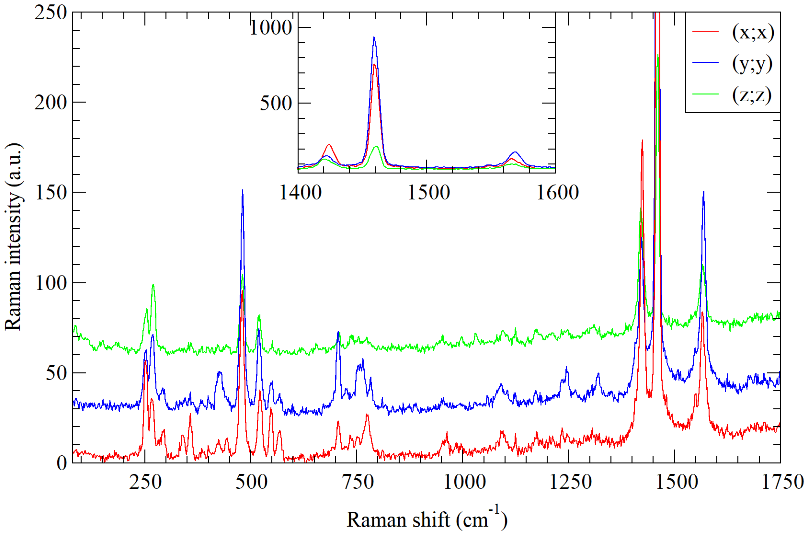

Figure 5.3: *Polarized extended Raman spectra of PCBM crystals grown from DCB. The spectra are offset for clarity. Inset: Fullerene pinch mode*

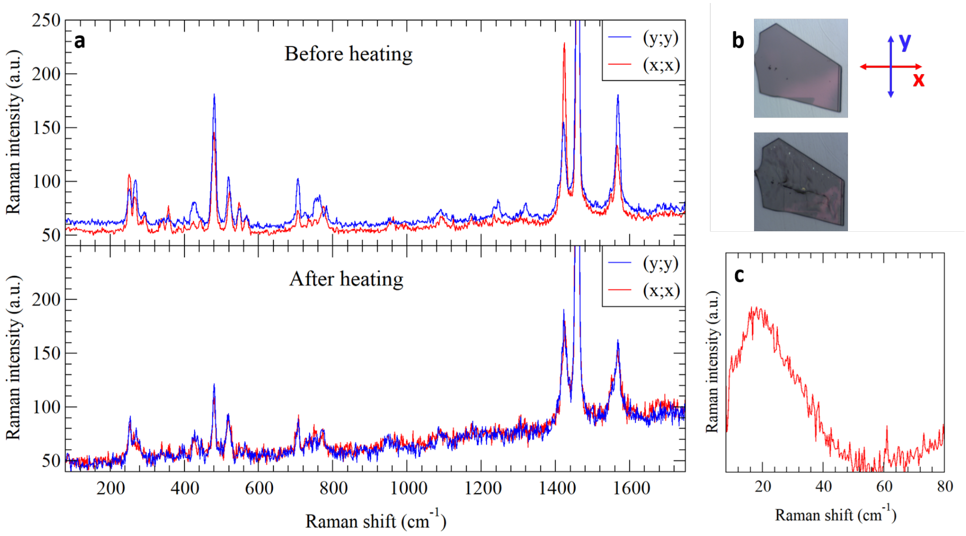

Figure 5.4: *a) Polarized IR of a PCBM crystal grown from DCB, recorded on the extended face, before and after heating. b) Microscopic images of the sample before (upper picture) and after heating (lower picture). c) Low frequency Raman spectrum measured after heating.*

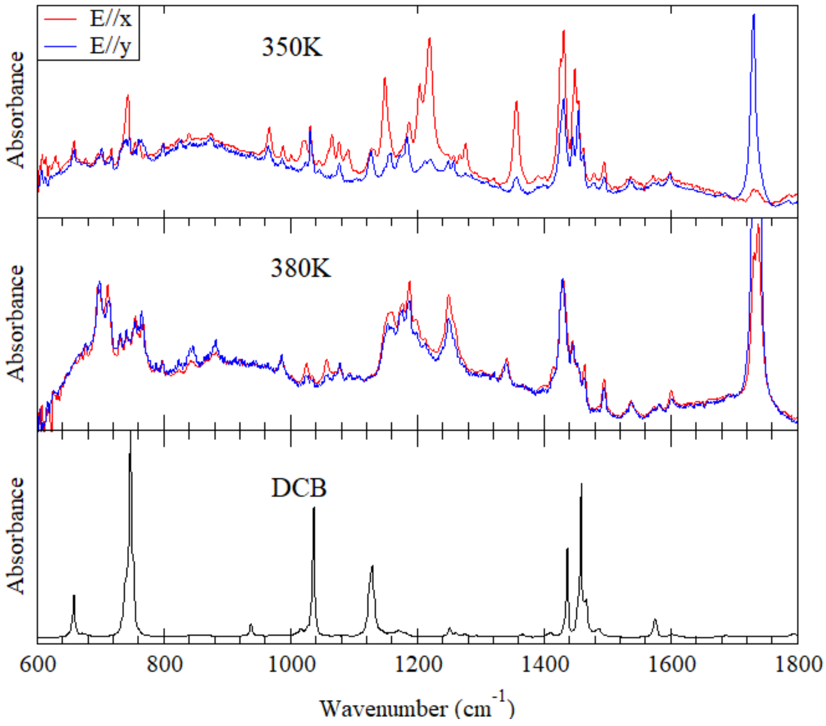

Figure 5.5: *Upper and middle panel: Polarized IR spectra of a PCBM-DCB crystal be below and above the solvent loss temperature. Bottom panel: IR spectrum of DCB.*

### 5.3.2 Phases obtained from CB solution

The PCBM crystals grown from CB present two different morphologies: thin rectangular platelets and thick prisms (Fig 5.6). The latter ones are much more abundant than the former ones. As all the crystals were strongly adhered to the substrate, they could not be removed without damage.

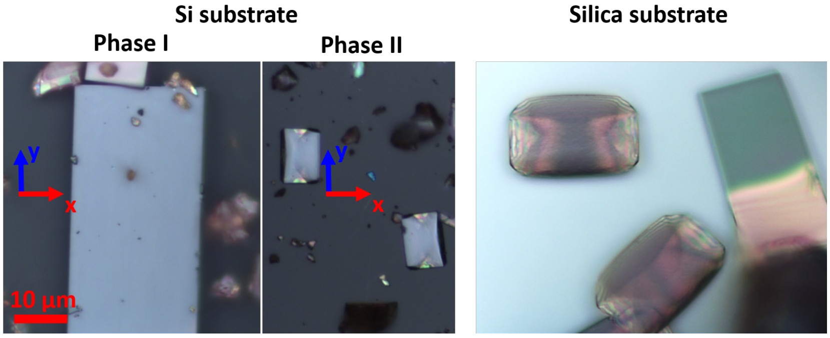

Figure 5.6: *Microscopic images of PCBM crystals grown from CB on Si or silica substrates.*

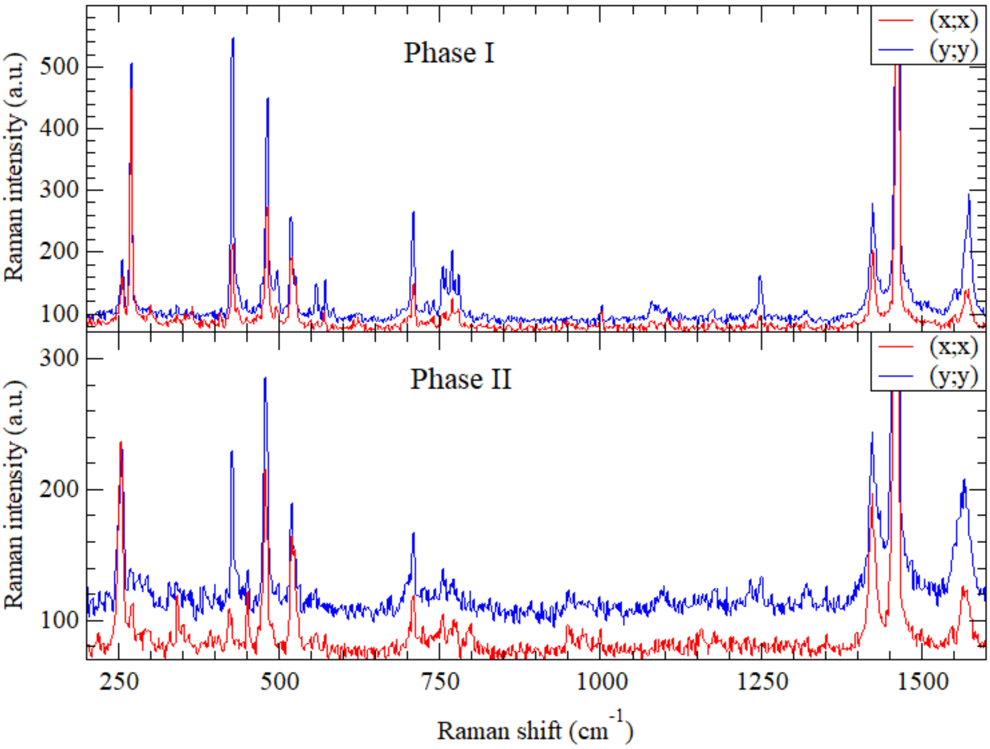

Figure 5.7: *Raman spectra of Phase I (upper panel) and Phase II (lower panel).*

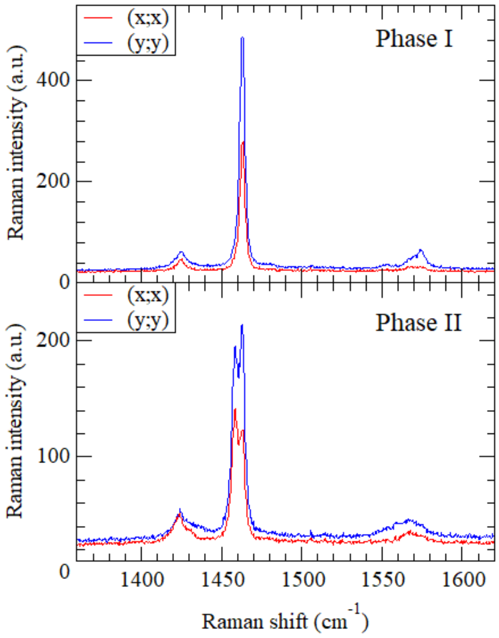

Figure 5.8: *Fullerene pinch mode in the Raman spectra of Phase I (upper panel) and Phase II (lower panel).*

As in the case of PCBM-DCB, we adopt a reference system where the $x$ and $y$ directions are parallel to the two symmetry axes of the extended crystal face. We could not directly recognize the extinction directions by microscopy as the crystals and/or the substrates were not transparent. This reference system is anyway convenient since the Raman spectra are well polarized only if the exciting and scattered light are polarized along these directions (Fig 5.7 and 5.9). This is true for the crystals of both morphologies. The relative band intensities in the polarized Raman spectra measured on different crystals with the same morphology are reproducible. This means that these crystals lay on the same plane.

The Raman spectra clearly demonstrate that the two morphologies correspond to different crystal phases. Thus, the rectangular platelets and the prisms are named Phase I and Phase II, respectively. Although the Raman spectra of both phases share the same bands, Phase I displays narrower features, in the whole spectral range (Fig 5.7 and 5.9). Furthermore, in the Phase II spectra the fullerene pinch mode band is split in two peaks at 1460 and 1464 cm$^{-1}$ , while in Phase I a single band is found at 1464 cm$^{-1}$ (Fig 5.8).

Phase I presents the same morphology described in [72] and [76], that report a solvent free PCBM phase grown from CB. Also the Raman spectra shown in [76], Fig 2b, display a single narrow band peaking at 1464 cm$^{-1}$ , as in the case of Phase I. Thus, Phase I likely corresponds to the known solvent free PCBM phase, having $P2_1/n$ space group and Z=4 [72]. Overall, the low frequency Raman spectra presents 8 phonon bands instead of the 12 ones expected from the unit cell symmetry and multiplicity. However, some bands might be very weak or inaccessible with the only crystal orientation probed.

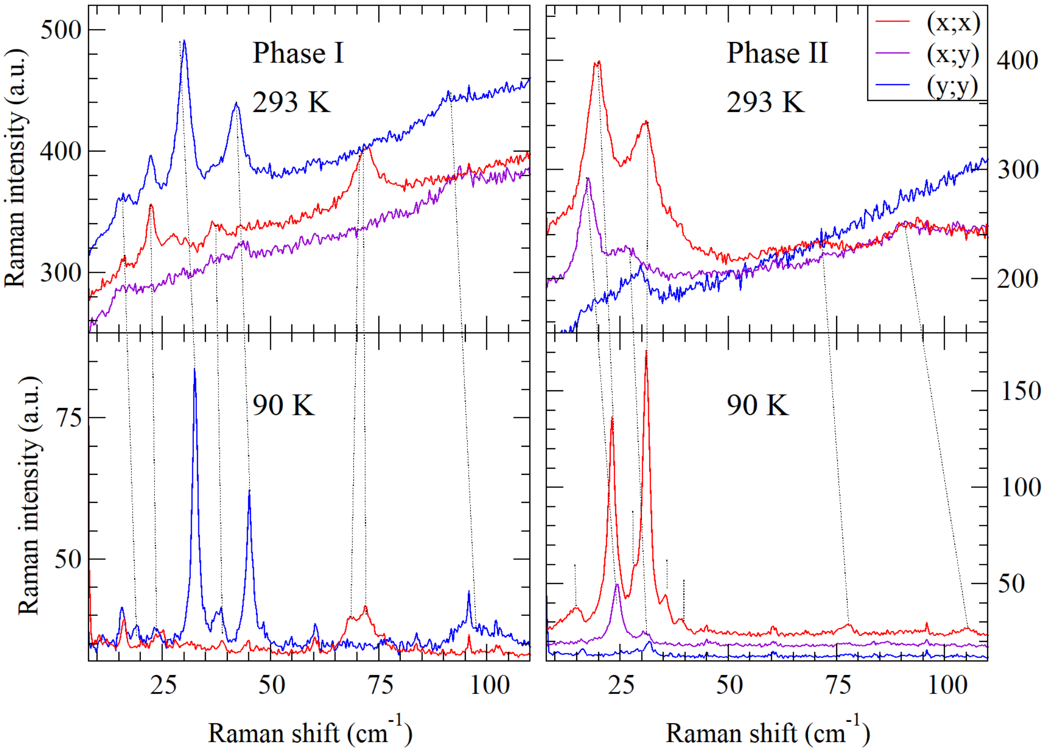

Figure 5.9: *Low frequency Raman spectra of Phase I (left panels) and Phase II (right panels), at 293 (upper panels)and 80 K (lower panels).*

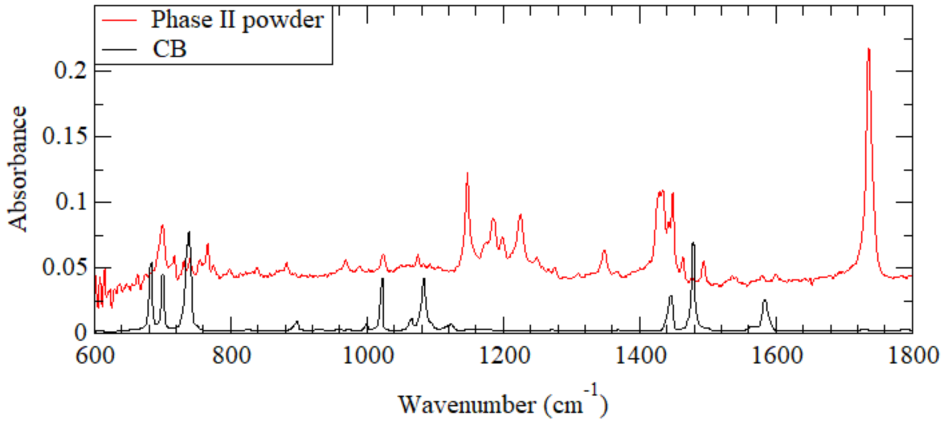

Figure 5.10: *IR spectrum of powdered Phase II crystals. The solvent spectrum, reproduced from the NIST database, is also shown for comparison.*

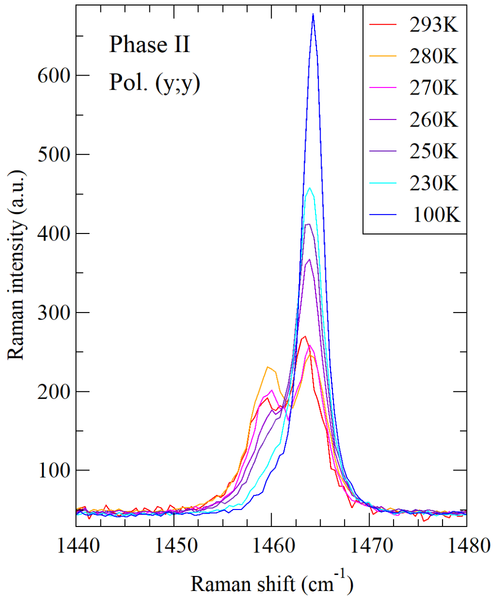

Figure 5.11: *Temperature evolution of the fullerene pentagonal pinch mode in Phase II.*

On the contrary, the Phase II features do not match any of the reported PCBM crystal phases. We measured the IR spectra of powdered crystals removed from the substrate to obtain further chemical information. The absence of the strongest CB solvent bands in the Phase II spectrum suggests that the crystal lattice does not contain solvent molecules (Fig 5.10). In addition, the known PCBM-CB solvate phase is triclinic [70], which is not consistent with the low frequency Raman spectra. Thus, Phase II is likely a new solvent-free phase.

At room temperature the Phase II phonon frequencies are lower than in Phase I, suggesting weaker intermolecular interactions. As Phase I, Phase II does not undergo any phase transitions down to 80 K. The phonon bands display the typical continuous frequency hardening on cooling. 10 phonon bands can be resolved at low temperature thanks to low temperature narrowing (Fig 5.9). Two of them have complete crossed polarization, which is consistent with at least a twofold symmetry element. Thus, the Phase II space group could be either monoclinic or orthorhombic.

Despite the absence of phase transitions, some unexpected spectral changes were observed at low temperature. The lower frequency component of the fullerene pinch mode completely loses its intensity on cooling from 293 to 250 K (Fig 5.11). This evolution is continuous and completely reversible without hysteresis. All the other Raman bands do not show any significant changes in the same temperature range. We do not attempt to explain such behavior, that would be completely speculative without further structural information.

## 5.4 Conclusions

We characterized the PCBM crystal phases grown from CB and DCB solutions on either silicon or silica substrates. In this work the obtained crystal phases depend only on the solvent and not on the substrate nature.

All the crystals obtained from DCB solutions only belong to the known PCBM-DCB 1:1 solvate phase [70, 71], which on heating releases the solvent molecules yielding an amorphous material. Differently, CB solutions yielded two polymorphs. One of them was recognized as the solvent free phase reported in [72] Although the other phase was not identified, the IR spectra suggest that it is solvent free as well. Further structural characterization is needed to confirm this hypothesis and investigate its unexpected thermal spectral changes.

# Chapter 6

# Crystal to Smectic E phase transition of the Ph-BTBT-10 molecular semiconductor

## 6.1 Introduction

The molecular semiconductor 7-decyl- 2-phenyl[1]benzothieno[3,2-b][1]benzothiophene (Ph-BTBT-10) has been widely studied over the last few years for its high charge carrier mobility and chemical stability. The rigid Ph-BTBT core is functionalized with a flexible decyl chain [81]. This structure was designed to achieve both good solubility and ordered liquid crystal phases, as a precursor of uniform thin films with increased 2-D mobility [82, 83].

Liquid crystalline mesophases are characterized by a partial loss of the structural order, given by the positional, orientational and intramolecular degrees of freedom. Calamitic (rod shaped) mesogens, as Ph-BTBT-10, can form nematic or smectic phases. While in the nematic phase the long molecular axes are aligned without positional order, in smectic phases the molecules are also arranged in layers. Smectic phases are classified based on the in-plane positional and orientational order and the tilt angle between the long molecular axis and the layer normal (Fig 6.1).

The Smectic E phase (SmE), also known as Crystal E, is one of the most ordered smectic phases. The unit cell is orthorhombic and the cores form a herringbone arrangement within the same layer. The long molecular axis is perpendicular to the smectic planes.

Ph-BTBT-10 undergoes three first order phase transitions on heating (Fig 6.2): Crystal to SmE at 150 °C; SmE to SmA at 215 °C and SmA to isotropic liquid at 225 °C [81]. Due to the asymmetric substitution, Ph-BTBT-10 crystallizes in bilayers. The monoclinic unit cell, space group $P2_1/a$, contains four molecules, with the long molecular axis nearly parallel to $c$. The rigid aromatic cores, arranged in herringbone packing, are separated from the decyl chains [85].

In the Crystal to SmE transition the structure changes from bilayer to monolayer, as the molecules are arranged head to tail. The transition is reversible with large

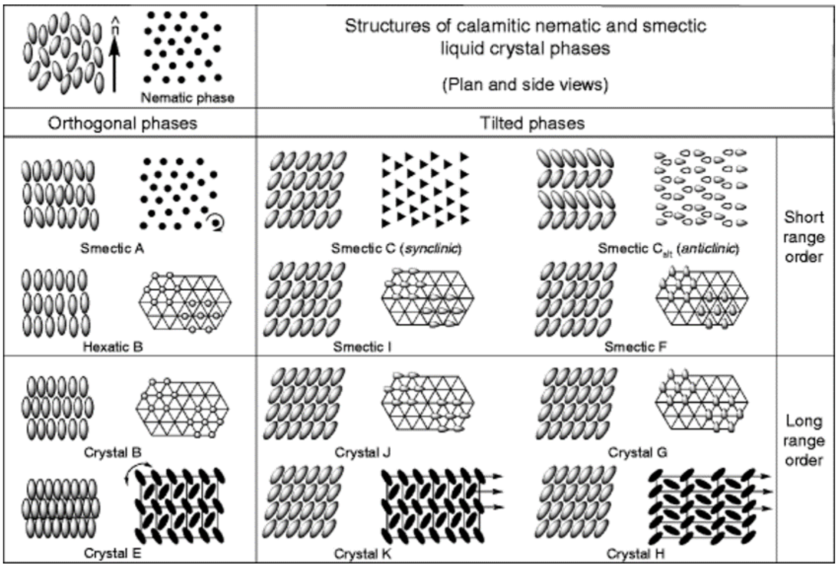

Figure 6.1: *Classification of the calamitic mesophases, on increasing structural order. Reproduced from [84]*

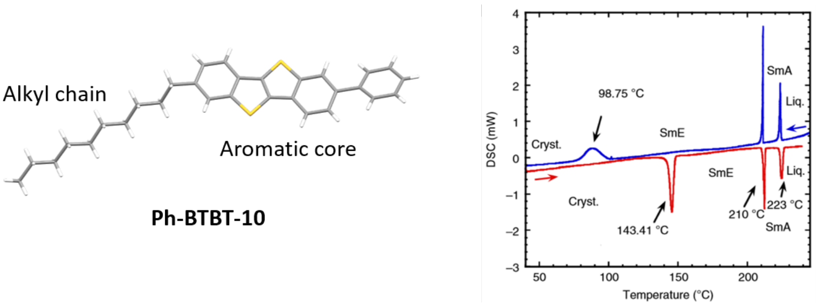

Figure 6.2: *Ph-BTBT-10 molecular structure and DSC curves. Reproduced from [81]*

hysteresis and strongly dependent on the cooling rate. Its mechanism and the detailed structure of the SmE phase are still under debate [86, 87, 88, 89].

To clarify these unanswered questions, we investigated the transition by polarized Raman and IR measurements on oriented single crystals. In the case of Raman, we probed two different crystallographic planes: *ab*, parallel to the molecular layers and *bc*, perpendicular to them. On each plane, the spectra were acquired with both parallel and crossed polarization. Thus, we are able to assign directionality and symmetry to the lattice phonons and follow them separately approaching the transition. Furthermore, we discuss the structural order in the SmE phase. The temperature evolution of the phonons and the orientation relationship between the lattices of the two phases provides a deeper insight into the mechanism of the transition.

## 6.2 Experimental

Ph-BTBT-10 was synthesized at Université Libre de Bruxelles by the group of Prof Y. H. Geerts following the previously reported procedure [81]. Single crystals were grown at Bologna University by Dr L. Pandolfi, by recrystallization of the synthesized powder in 1,2-dichlorobenzene.

The Raman spectra were recorded with the Horiba Lab RAM HR Evolution Raman microscope, exciting with the 633 nm line. The confocal pinhole was closed to 60 $\mu$m to reduce stray light close to the laser line. With this configuration, the phonon bands were completely accessible down to 4 cm$^{-1}$ . The measurements were performed in backscattering geometry on both *bc* and *ab* planes, with the exciting and scattered light polarized parallel or perpendicular to the *b* axis (Fig 6.3). Since the crystals, platelets with typical size 100 x 200 x 5 $\mu$m$^3$, tend to overlap, the samples were chosen checking complete extinction between two crossed polarizers. For the measurements on the *bc* plane, a vertically oriented crystal was fixed between two glass slides.

When comparing spectra recorded at different temperatures, the raw data were converted into the imaginary part of the dynamic susceptibility $\chi''(\nu)$ according to this equation [90, 43]:

$$\chi''(\nu) \propto \frac{1}{(\nu_0 - \nu)^4} \times \frac{I(\nu)}{n(\nu) + 1}$$

where

$$n(\nu) = [exp(\frac{hc\nu}{kT}) - 1]^{-1}$$

The Bose-Einstein thermal factor $n(\nu)$ corrects the intensity enhancement at small wavenumbers due to the thermal excitation of vibrational modes. The factor $(\nu_0 - \nu)^4$, where $\nu_0$ is the wavenumber of the exciting light, accounts for the scattering probability at the absolute wavenumber of the scattered light. While the former factor strongly reduces the intensity at small wavenumbers, the latter one has negligible effects in the same spectral range.

The polarized IR spectra were measured in transmission mode on a single crystal laying on the *ab* plane placed on a ZnSe slide, using a Bruker IFS-66 FT-IR spectrometer coupled to a Hyperion 1000 IR microscope.

The temperature was controlled from 80 to 488 K using a Linkam HFS 91 stage, fitted under the microscopes. To evaluate the effect of the cooling rate on the SmE to Crystal transition, the samples were cooled down to room temperature at a rate of 0.5 K/min or 90 K/min.

## 6.3 Results and discussion

### 6.3.1 Room temperature spectra

The crystals show elongated platelet morphology and the two in-plane symmetry axes coincide with the extinction directions. The observed morphology completely agrees with the prediction based on the Bravais, Friedel, Donnay and Harker (BFDH) method, allowing the assignment of the longer in-plane axis to $a$ and the shorter one to $b$. These two directions are parallel to the molecular layers and nearly perpendicular to the long Ph-BTBT-10 axis. This morphology is due to a faster growth along the $a$ and $b$ directions, driven by the strong in-plane $\pi$ interactions between the aromatic BTBT cores [85].

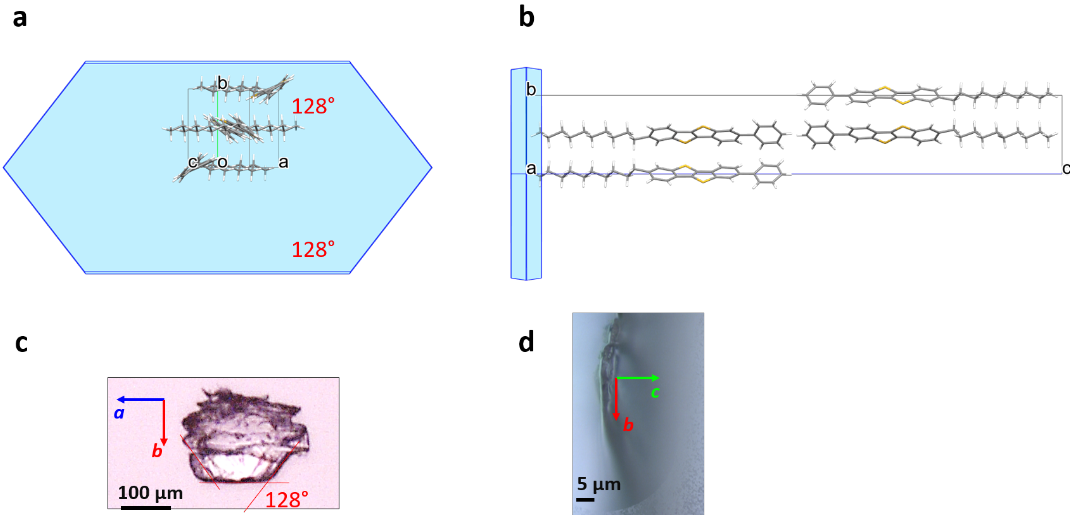

Figure 6.3: *BFDH morphology of Ph-BTBT-10 crystal, viewed along a) $c^*$ and b) $b$ directions together with the unit cell (CCDC refcode ROQSAT). The microscopic images of a crystal viewed along the same directions are shown in c) and d). The crystal shown in d) is about 5 µm thick.*

Table 6.1: *Ph-BTBT-10 phonon frequency and symmetry at 295 K*

| **Frequency** | **Polarization** | **Symmetry** |
|---|---|---|
| 4 s | *bc*, *cc* | $B_g$ |
| 11 s | *cc* | $B_g$ |
| 11 s | *cc* | $A_g$ |
| 16.5 s | *bc*, *ab* | $B_g$ |
| 19 m | *cc*, *bb*, *aa* | $A_g$ |
| 29 w | *aa*, *bb*, *cc* | $A_g$ |
| 35 w | *bc*, *ab* | $B_g$ |
| 43 m | *cc*, *bb* | $A_g$ |
| 53 m | *aa*, *bb* | $A_g$ |
| 62 w | *cc* | $A_g$ |
| 84 m | *aa*, *bb* | $A_g$ |
| 95 m | *ab*, *bc* | $B_g$ |

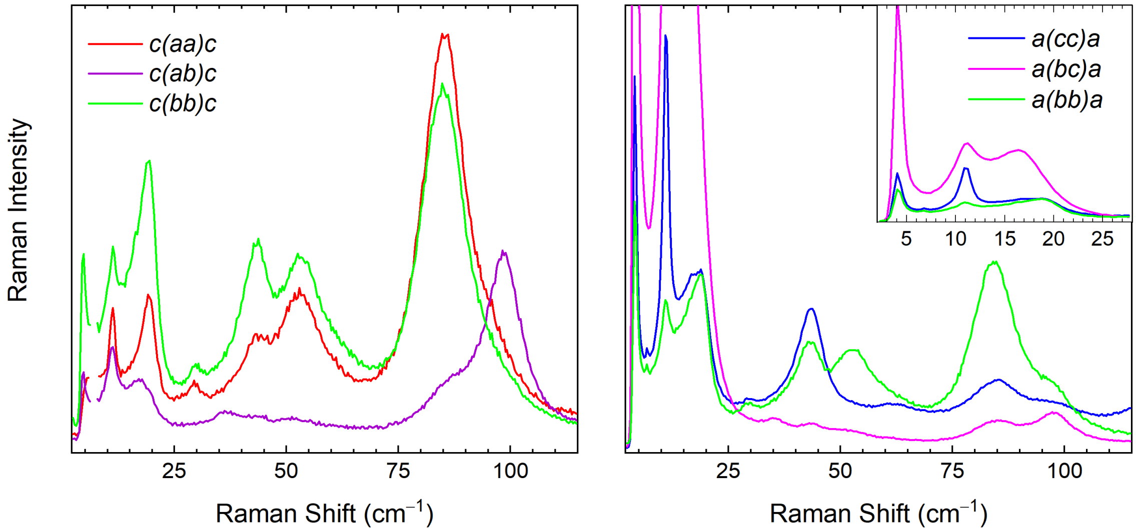

Figure 6.4: *Low frequency polarized Raman spectra of crystalline Ph-BTBT-10, measured on the ab (left panel) and bc planes (left panel). In the latter spectrum the 3-200 cm$^{-1}$ range has been enlarged with a higher intensity scale. In some spectra a plasma line from the laser at 7 cm$^{-1}$ has been removed.*

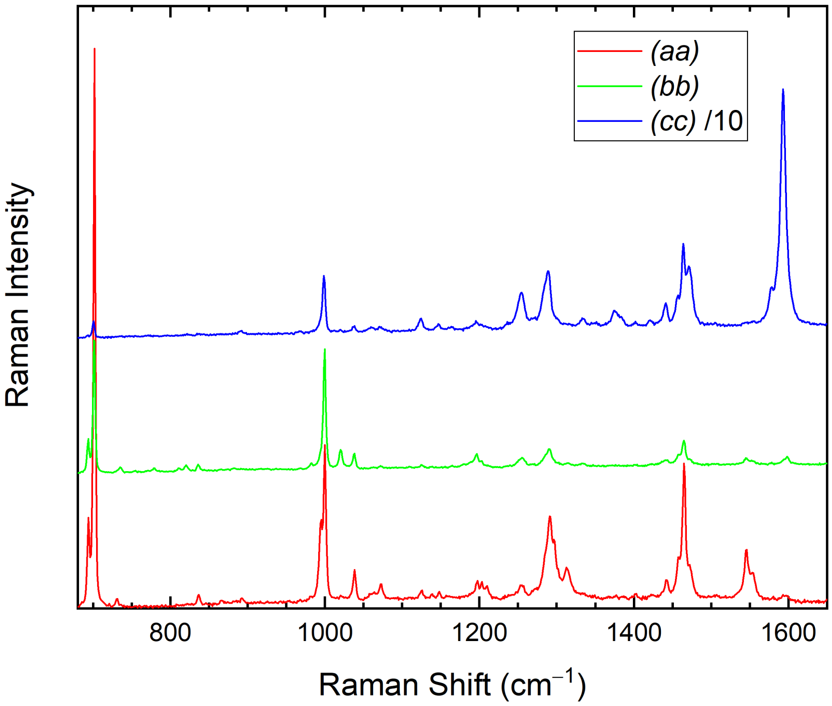

Figure 6.5: *Extended polarized Raman spectra of a Ph-BTBT-10 crystal. The spectra are upshifted and the cc polarized one has been divided by 10 for clarity.*

In the case of the flexible Ph-BTBT-10 molecule it is difficult to single out the number of lattice modes from symmetry and multiplicity of the unit cell, as the inter- and intra-molecular vibrations are strongly mixed. The intermolecular vibrations, having small force constants and large effective masses, are always found at low frequencies. Thus, we can assume that below 120 cm$^{-1}$ most modes have intermolecular character. In the $P2_1/a$ space group the Raman active modes have $A_g$ or $B_g$ symmetry. The former are visible with *aa bb cc* or *ac* polarization, while the latter are *ab* or *bc* polarized. The two letters indicate the polarization direction of the exciting and scattered light, respectively.

As expected, the Raman spectra recorded with both exciting and scattered light polarized parallel to the layers (*aa*, *ab* and *bb*) are very different from the out-of plane polarized ones, *cc* and *bc*, in the whole frequency range. In the low frequency range (4-125 cm$^{-1}$ ) all the in-plane polarized spectra (*aa*, *ab* and *bb*) show medium intensity bands around 90 cm$^{-1}$ while the out-of plane polarized ones, *cc* and *bc*, display very strong bands below 20 cm$^{-1}$ (Fig 6.4 and Table 6.1). The *aa* and *bb* spectra share the same $A_g$ bands, with small differences in the relative intensities. The *ab* spectrum has a similar pattern, but with different bands, having $B_g$ symmetry. More interestingly, in the *bc* spectra very low frequency $B_g$ bands are present with a huge intensity, almost an order of magnitude more intense (see Fig. 6.4).

Due to the strong anisotropy of the Ph-BTBT-10 arrangement, the modes polarized in the *ab* plane probably correspond to in-plane translations or rotations about the long axis of the molecules. Differently, the out-of-plane polarized modes involve translations along the long molecular axis. Such interpretation is consistent with the calculated spectra of the analogue system C8O-BTBT-OC8 [91]. The assignment is further confirmed comparing the polarized spectra of Ph-BTBT-10 and unsubstituded BTBT, that also crystallyzes in a layered structure ( see Appendix B.1). Thus, the in-plane polarized spectra mainly reflect the molecular packing in the layers while the out-of-plane polarized ones are more affected by interlayer interactions. The lower frequencies of the interlayer polarized phonons indicate weaker intermolecular interactions between adjacent layers. This also agrees with the thin platelet morphology of the crystals.

At higher frequencies, where the modes have complete intramolecular character, the *aa* and *bb* polarized spectra are very weak (Fig 6.5). The intensity is instead enhanced almost an order of magnitude in the *cc* polarization, as expected from the molecular orientation respect to the crystallographic axes. Indeed, the molecular Raman cross section is higher with exciting and scattered light polarized parallel to the long axis of the BTBT cores. The high frequency Raman spectra will be discussed further in Section 6.3.3, together with the IR spectra. The following section is focused on the temperature evolution of the lattice phonons approaching the transition.

### 6.3.2 Towards the transition: the soft mode

On approaching the Crystal to SmE phase transition, two phonons with soft behavior are evident in the *bc* polarized spectra (Fig 6.6, left panel, and 6.7). The $B_g$ band centered at 23 cm$^{-1}$ at 83 K strongly redshifts on increasing temperature, becoming very broad. Around 300 K it gets closer to the phonon at 12 cm$^{-1}$ without crossing it. The two modes get strongly mixed, as the spectral weight is redistributed between them. Also the soft behavior is transferred to the lower frequency phonon, that moves to zero frequency close to the transition. The higher frequency band is weakened and appears only as a broad shoulder close to the transition temperature.

In the same spectrum, the strong narrow band at 5 cm$^{-1}$ is no more accessible above 320 K, cut below the ULF filter limit and we can't investigate its behavior near the transition. However, its temperature evolution in the available temperature range, from 83 K to 320 K, is characterized by the absence of sizeable broadening and seems to exclude any role in the soft mode. Being visible in many polarizations, it might also be assigned to an intramolecular chain mode. Indeed, such low frequency phonons have been predicted in alkylated BTBT derivatives [92].

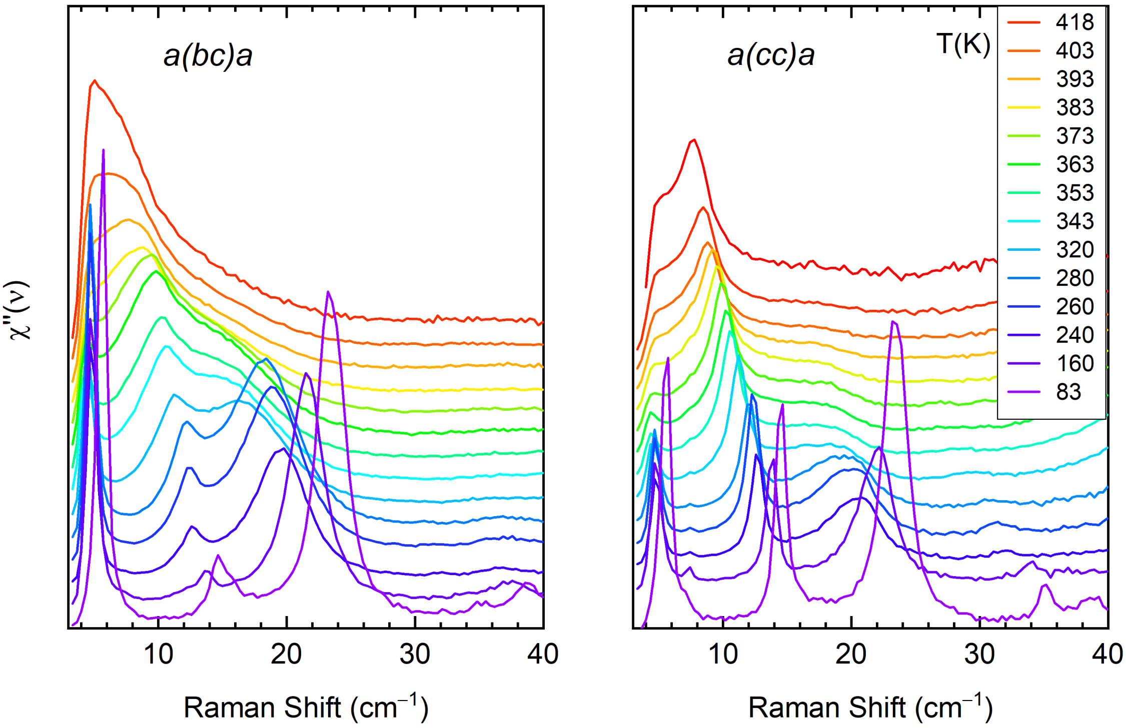

Figure 6.6: *Low frequency Raman spectra with bc (left panel) and cc (right panel) polarization on heating from 83 K to 418, close to the transition. These spectra are the imaginary part of the susceptibility calculated from the raw Raman data. The spectra are upshifted for clarity.*

The $A_g$ phonons show a typical temperature evolution, as can be seen comparing the *cc* and the *bc* spectra (Figs 6.6, right panel, and 6.7). The two lowest frequency bands, initially superimposed to the two $B_g$ ones with soft behavior, do not shift to zero frequency. Furthermore, these bands are narrower than the $B_g$ counterparts at all the temperatures. Also the higher frequency phonons, visible in the in-plane polarized spectra, do not display any effect anticipating the transition (Fig 6.9) .

Thus, the bilayer to monolayer phase transition is driven by a soft mode of $B_g$ symmetry, strongly out-of-plane polarized. It is probably an effective soft mode, due to the combination of two phonons. Before proposing a description of the mode leading the transition, we remark that, being it Raman active, must have $k$=0, i. e., all the unit cells move in phase. A sensible description would be the opposite translation

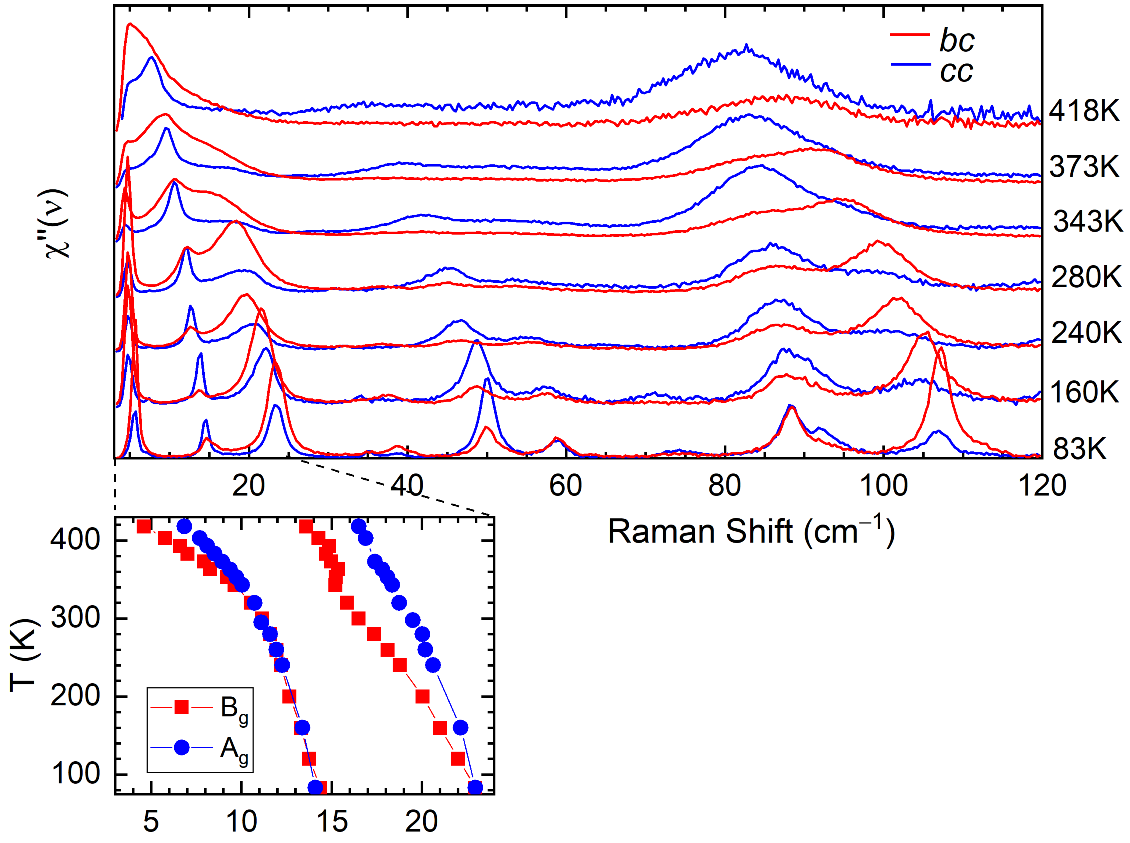

Figure 6.7: *Upper panel: comparison between the bc and cc polarized spectra on increasing temperature. Lower panel: temperature dependent frequency shifts of the bands found at 14 and 23 cm$^{-1}$ at 83 K in the two polarizations. The $A_g$ and $B_g$ modes initially superimposed, behave differently on increasing temperature*

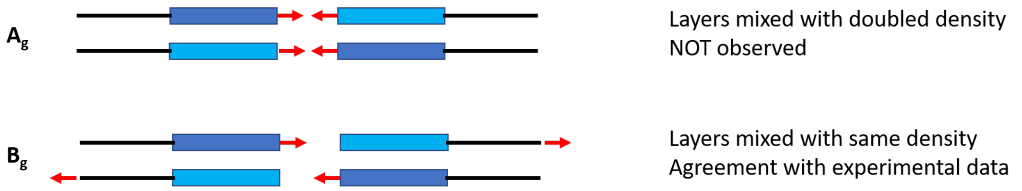

Figure 6.8: *Possible $A_g$ and $B_g$ modes involving the translation of the molecules along their long axis, perpendicular to the layers.*

along the $c$ axis of two adjacent molecules belonging to the same layer. If the two opposite layers in the unit cell move out of phase, the resulting phonon would have $B_g$ symmetry. Indeed, the interpenetration of the two opposite layers by translation of the molecules along the $c$ axis is thought to be the most likely mechanism of the transition [93, 88]. This mode would mix the adjacent layers maintaining the same molecular density. Following these displacements, two head-to-tail layers can be obtained from two head-to-head ones with opposite orientation. On the contrary, the $A_g$ counterpart would collapse two layers in one, also changing the macroscopic

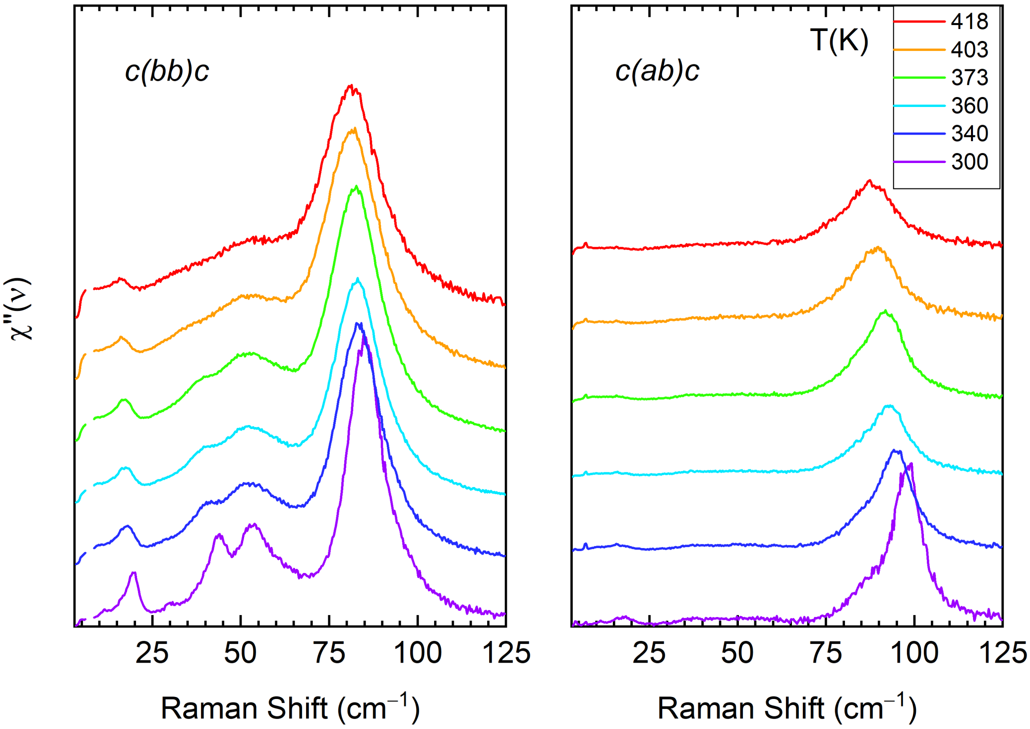

Figure 6.9: *Low frequency Raman spectra with bb (left panel) and ab (right panel) polarization on heating from 300 K to 418, close to the transition. The spectra are upshifted for clarity.*

dimensions of the sample and contradicting the experimental observation (Fig 6.8). As will be shown in the following sections, the sample shape is unchanged during the transition.

### 6.3.3 The SmE phase

Despite the soft mode, the transition is discontinuous: the *bb* polarized phonon bands are suddenly replaced by a single broad one around 70 cm$^{-1}$ . The *aa* spectrum is superimposable to the *bb* one. The *ab* polarized spectrum behaves similarly, but is never superimposable to the other two. As in the crystal phase, the *ab* polarized band peaks at a higher frequency (Fig 6.10, left panel), while a strong peak around 6 cm$^{-1}$ is present in the *bc* and *cc* polarizations (Fig 6.10, right panel). This low frequency band is absent in all the in-plane polarized spectra. Due to the complete interlayer polarization, this band is more likely a lattice phonon than an intramolecular mode, with a strong translational component along the *c* axis. Indeed, low frequency pseudo-lattice vibrations have been reported in smectic phases containing polar molecules with antiparallel alignment. These bands were assigned to the opposite translation of two antiparallel molecules along their long axis [90, 94]. Thus, the occurrence of such phonon in Ph-BTBT-10 SmE phase is consistent with a monolayer structure. Overall, the relative intensity pattern of the in-plane and out of plane polarized spectra is the same of the crystal phase. These facts give evidence that the layer structure is maintained with the same orientation during the Crystal to SmE transition. In addition, being the *ab* and *bb* polarized spectra different, some kind of in-plane order must be present.

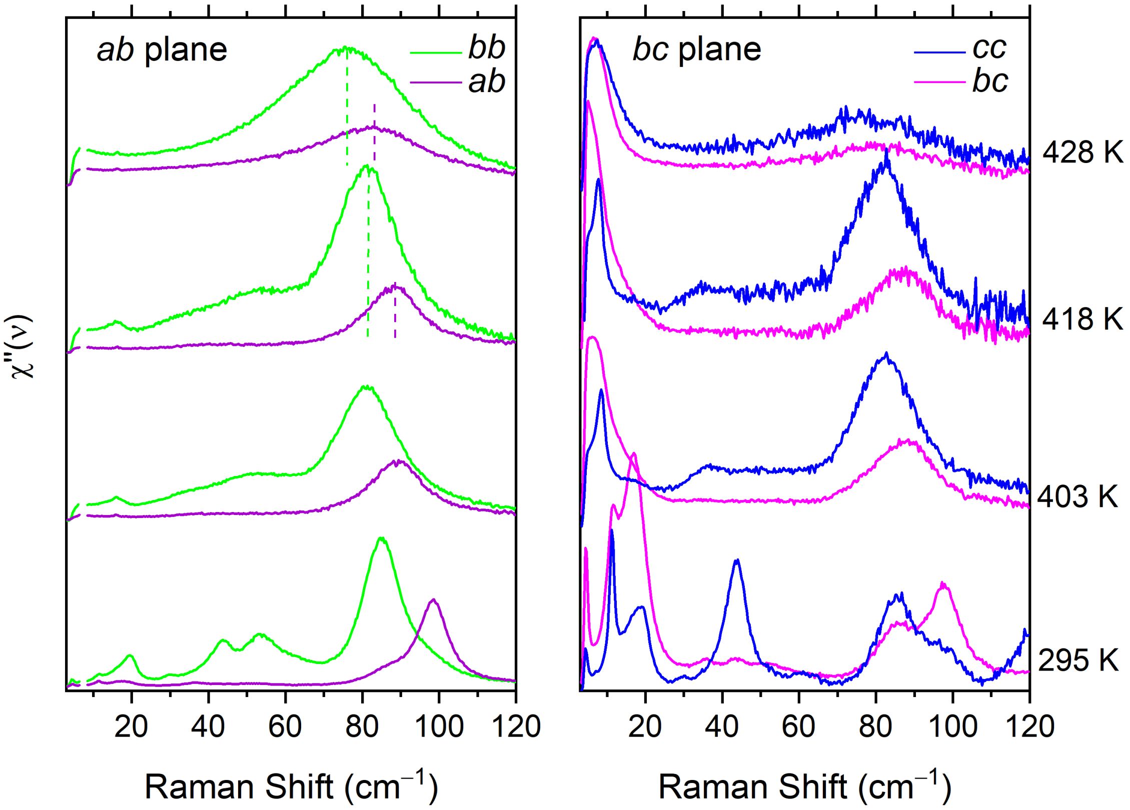

Figure 6.10: *Polarized Raman spectra of Ph-BTBT-10 on crossing the transition: ab plane (left panel) and bc plane (right panel). The dashed lines correspond to the center of the band of the same color.*

The in-plane orientational order can be conveniently assessed following the intramolecular vibrational modes, found at higher frequencies. The relative intensities of these bands depend on the molecular orientation. But the in-plane polarized Raman spectra are very weak (see Fig 6.5) and require long exposure times under the laser beam. This may damage the sample surface at high temperatures.

For this reason, the intramolecular modes were investigated mainly by IR. Thanks to the limited sample heating, also the SmE to SmA transition at 488 K was accessible. However, the SmA to isotropic liquid transition was not, as the thin samples easily sublimate at these temperatures.

Differently from Raman, the IR measurements in transmission mode probe the whole crystal volume. Depending on the diffraction limit and the optics of the microscopes, the spot size is around 500 nm in Raman and 50-100 $\mu$m in IR. For this reason, the IR measurements on single crystals were possible on the *ab* plane only.

With this sample orientation both the in-plane orientational order of the aromatic cores and the conformational order of the chains can be followed on heating. These two kinds of order can be assessed separately by observing the internal vibrations of the cores (700-1500 cm$^{-1}$ ) or the aliphatic C-H stretching modes of the chain (2800-3000 cm$^{-1}$ ). These parts of the molecule have different flexibility, conformational freedom and type of possible interactions. Thus, their behavior can be different in the various mesophases.

In the crystal phase the aromatic core vibrations show different relative intensities in the spectra recorded with the light polarized along $a$ or $b$ (Fig 6.11). The intensity ratio of these modes reflects the orientation of the aromatic cores respect to the two in-plane axes. Also the C-H stretching modes are well polarized, being stronger in the $b$ polarization (Fig 6.12). As these modes are the most sensitive to crystal packing, the splitting between the $A_u$ ($b$ polarized) and $B_u$ ($a$ polarized) modes is clearly visible.

Below the Crystal to SmE transition the spectral changes on increasing temperature are negligible, except for a small broadening of the bands. Crossing the transition, the C-H stretching modes completely depolarize. The core vibrations are instead still polarized, in the same way of the crystal phase. This means that in the SmE phase the chains are conformationally disordered, as observed in other mesogens undergoing crystal to SmE transition [95, 96]. On the contrary, the planes of the aromatic cores maintain the same orientation of the crystal phase. This orientational order must have long range character, as the IR measurements probe the whole crystal volume.

The in-plane orientational order is consistent with the nanosegregation between molten aliphatic chains and in-plane ordered aromatic cores, proposed in [86]. Assuming a mixed layer arrangement instead, it would be difficult to explain the in-plane order. It is known that in SmE phases the cores assume a herringbone arrangement [97], due to the $\pi$ interactions between them. The presence of disordered chains between the cores would weaken these interactions.

Also the Raman spectra of the SmE phase in the 700-1500 cm$^{-1}$ frequency range, with $aa$ and $bb$ polarization, show the same intensity pattern of the starting crystal phase. Thus, the Raman spectra confirm the IR ones, but on a smaller spatial scale. Furthermore, the absence of the band around 1600 cm$^{-1}$ , very strong in the $cc$ polarization (Fig 6.13), demonstrates that in the SmE phase the long molecular axes are still normal to the layers.

The IR spectra of the SmE phase do not depolarize over time even at 480 K, demonstrating that the in-plane order is stable. But at the SmE to SmA transition, occurring at 488 K, the core vibrational bands suddenly depolarize. The relative intensities of these bands are an average of the two polarized spectra of the SmE phase. This means that the long molecular axes maintain the vertical alignment, but the in-plane orientational order is lost. This is typical of SmA phases, where the molecules freely rotate about their long axes. The C-H stretching bands are unchanged respect to the SmE phase. Thus, in Ph-BTBT-10 the structural order is lost step by step through the two smectic phases.

So, what are the structure and the source of disorder in the SmE phase? And what motions are possible? Hofer et al. [86] reported that the unit cell of Ph-BTBT-10 SmE phase contains two molecules and antiparallel molecules are mixed in the

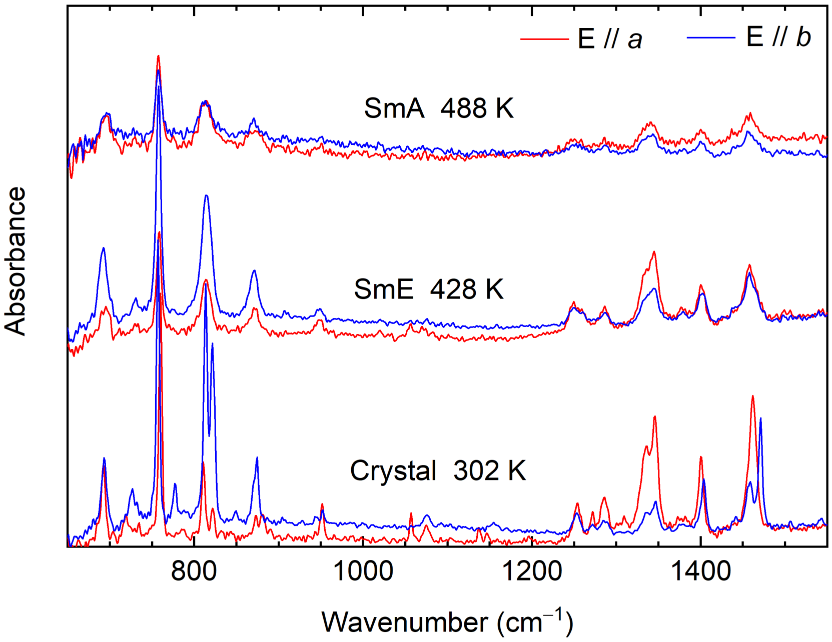

Figure 6.11: *Polarized IR spectra of three phases of Ph-BTBT-10 in the spectral range of the core vibrations: Crystal (302 K), SmE (428 K), SmA (488 K).*

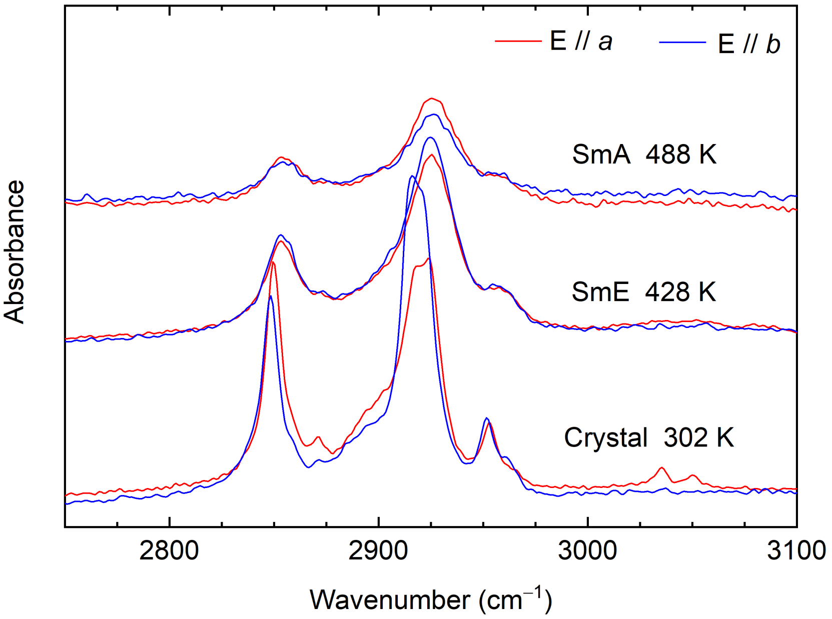

Figure 6.12: *Polarized IR spectra of three phases of Ph-BTBT-10 in the spectral range of the C-H stretching modes: Crystal (302 K), SmE (428 K), SmA (488 K).*

same layer with herringbone arrangement of the cores. Thus, in this picture four distinct molecular orientations would be still possible, i. e. two alignments of the long axis and two in-plane core orientations, as in the crystal phase. For this reason, the parallel or antiparallel alignment of the long molecular axis must lack periodicity between the adjacent layers and/or within the same layer. In addition, the correlation

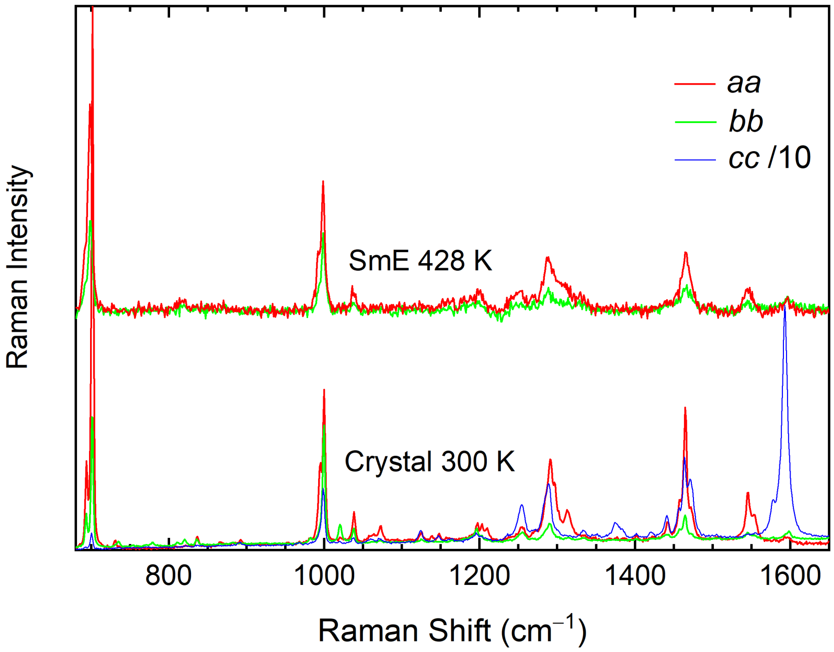

Figure 6.13: *Polarized Raman spectra of the Crystal and SmE phase.*

in the interlayer direction is likely short range, being the layers separated by fluid layers of disordered chains. A molecular motion compatible with both the in-plane orientational order and the head-to-tail disorder is the in-plane diffusion described in Ref [98].

These hypotheses explain the monolayer structure without introducing the upside-down flipping of the molecules about the short axes. Although it has been described in other mesogens with SmE phases [99, 100], such motion would be difficult in a closely packed phase, with a stable in-plane orientational order. For this reason flipping is unlikely in the case of Ph-BTBT-10.

### 6.3.4 Cooling the SmE phase

The crystal to SmE phase is reversible with a large thermal hysteresis, depending on the cooling rate. Fast cooling (rate >> 20 K/min) suppresses the recrystallization, yielding a glassy solid, metastable at room temperature [81]. The vitrification of the SmE phase is not apparent under the microscope: the shape of the starting crystal is unchanged and no cracks appear on cooling (Fig 6.14, panels a-c). Surprisingly, the glassy sample shows complete extinction along the same directions of the starting crystal (Fig 6.14, panels d-e). If the cristal is randomly oriented, extinction does not occur (Fig 6.14, panel f).

The same phonons observed at 430 K are still present, narrower and blueshifted. The bands are always broader than in the crystal phase at the same temperature, consistently with a more disordered structure. The interlayer polarized peak is blueshifted from 6 to 8 cm$^{-1}$ and is now completely accessible (Fig 6.15). Also the in-plane polarized spectra show minor changes and maintain the same polarization pattern observed at 430 K. This means that the glassy solid has the same symmetry and 3D order of the SmE phase. However, most thermal motions present in the SmE phase are hindered: the dynamic disorder is frozen into static disorder.

Slow cooling results in recrystallization, occurring at around 115 °C, with a cooling rate $< 2$K/min [81, 101, 93]. The SmE to crystal transition involves the sudden cracking along the (110) and $(1\bar{1}0)$ directions of the starting crystal. These cracks on the surface separate different domains. If the sample is rotated between two crossed polarizers, extinction occurs at different angles in each domain (Fig 6.16). This fact demonstrates the rotation of the crystallographic axes with respect to the starting crystal, opposite to the fast cooling behavior.

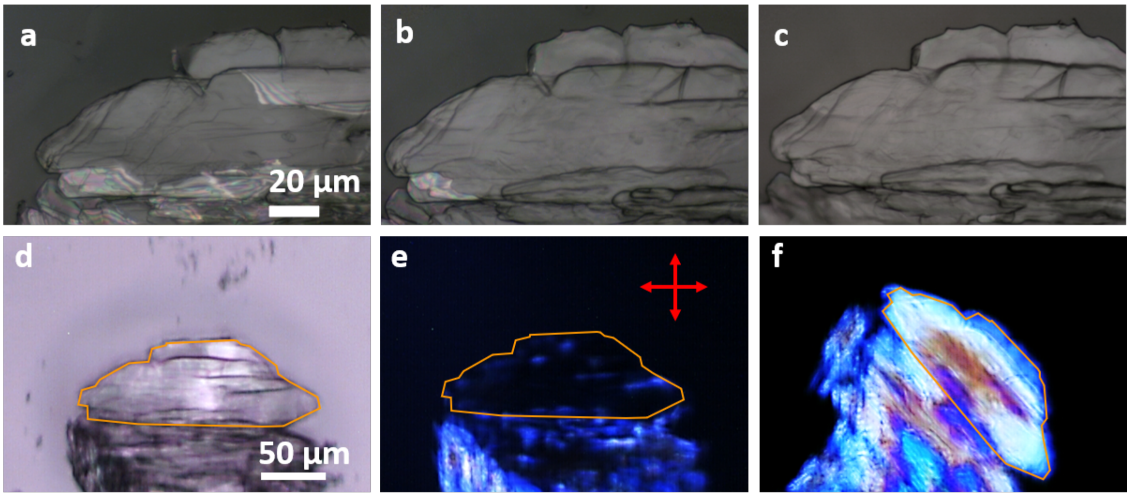

Figure 6.14: *a, b, c: Microscopic images of an oriented Ph-BTBT-10 sample, before heating (a); at 430 K (b) and after cooling at 90 K/min (c). d, e, f: frozen SmE phase, observed in reflection mode (d) and in transmission mode between two crossed polarizers (e and f), whose polarization axes correspond to the red arrows. In the reference single crystal domain, delimited with orange line, the a axis is the elongation direction.*

The rotation of the crystal axes with respect to the pristine ones were estimated measuring the polarized Raman spectra in few domains. The sample was rotated while the polarization directions of the exciting and scattered light were fixed (Fig 6.17). The spectra indicate an in-plane rotation of the $a$ and $b$ axes, demonstrating that the layer orientation is maintained also in the reverse transition. These results are further confirmed measuring on the $bc$ plane: the $cc$ polarized spectra are always recovered on cycling the transition and never mix with the $aa$ and $bb$ ones (Fig 6.15, middle panel).

In the recrystallized sample the bands are always broader than in the pristine crystal at room temperature. Besides, the extinction in the recrystallized sample is incomplete. These facts indicate a residual structural disorder, probably due to the misalignment of some molecules along the $c$ axis [101]. At the same time, the non-random cracking pattern and rotation angles of the domains reflect the ordered herringbone arrangement of the starting SmE phase.

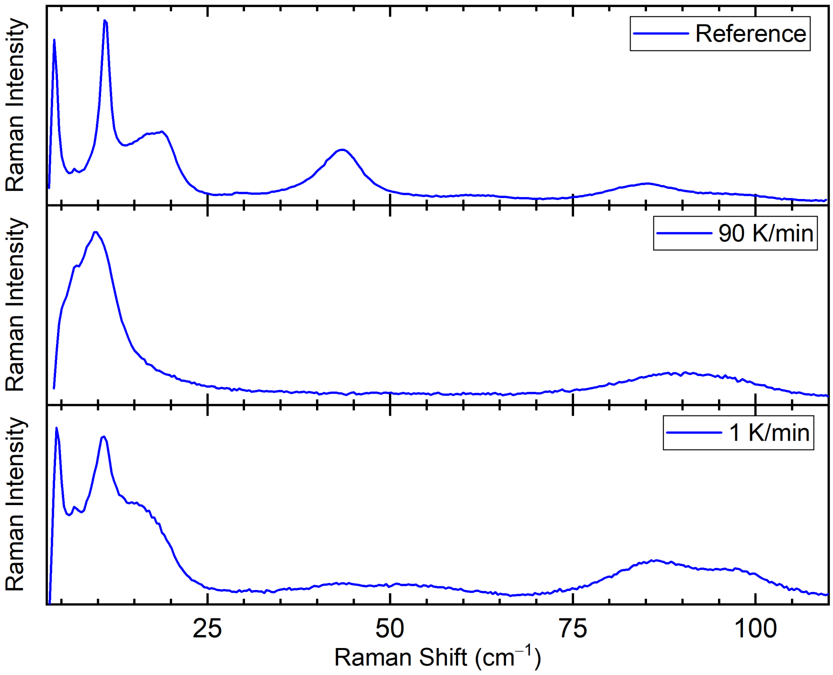

Figure 6.15: *cc polarized Raman spectra of Ph-BTBT-10 crystals: before heating (upper panel) and cooled from the transition temperature to 295 K at 1 K/min (middle panel) and 20 K/min (lower panel).*

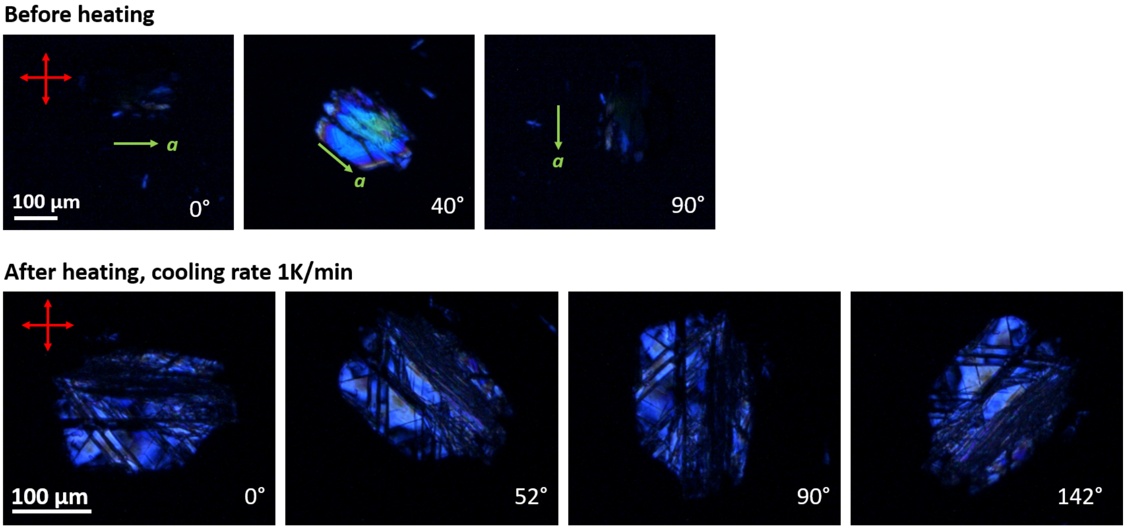

Figure 6.16: *Microscopic images of an oriented Ph-BTBT-10 sample obtained by slow cooling, between two crossed polarizers, whose polarization axes correspond to the red arrows. The rotation angle is indicated in each image.*

Since the layer structure is maintained, the rotations about the short axes (upside-down flipping) must be impossible during the phase transitions. The rotation of the domains about the (001) direction gives evidence of molecular rotation about the long axis at the SmE to Crystal transition. Such rearrangement follows the

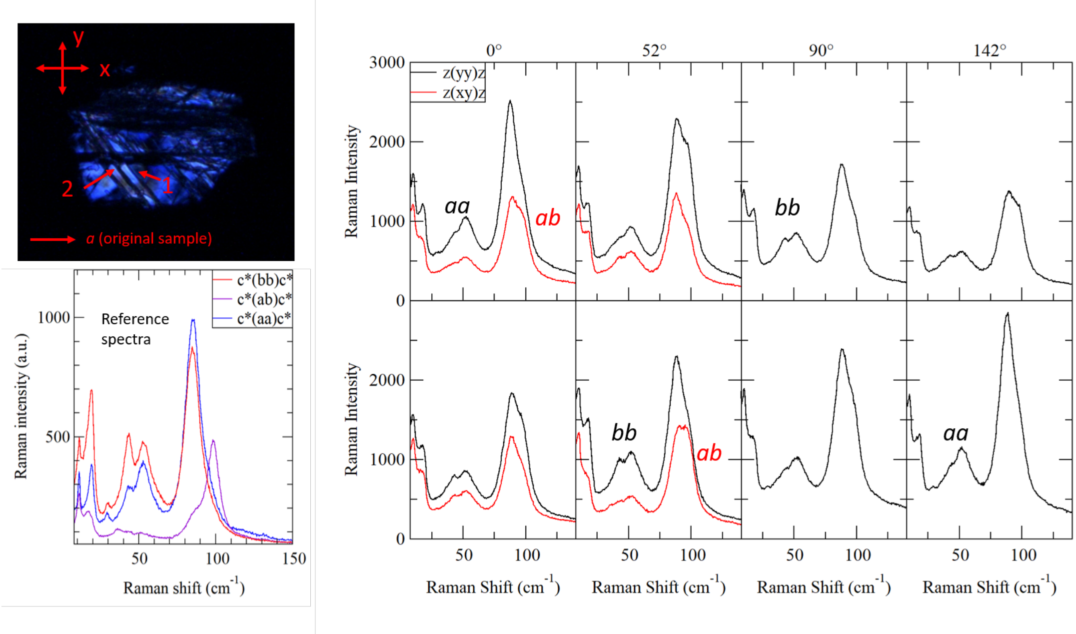

Figure 6.17: *15 Right panel: polarized Raman spectra recorded in two domains (indicated in the image on the left) at 295 K on a slowly cooled sample. The exciting and scattered light are polarized along x or y and rotation angles are the same as in Fig 6.16. The crystal orientation of the domains is recognized comparing the observed spectra with the in-plane polarized spectra of a single crystal (lower panel on the left). The a and b axes are rotated by 90° in domain 1 and 52° in domain 2.*

interpenetration of the layers due to the interlayer translations, as in the case of the Crystal to SmE transition. The mechanism is therefore similar in both transitions, but the partial disorder in the SmE phase results in a polycrystalline recrystallized sample.

## 6.4 Conclusions

We investigated the bilayer to monolayer phase transition of Ph-BTBT-10 by polarized Raman and IR spectroscopy on oriented single crystals. Based on the temperature evolution of the lattice phonons and the 3D order of the SmE phase we propose a possible mechanism for the transition.

The transition is anticipated by an interlayer polarized soft phonon and associated with a discontinuous broadening of the in-plane polarized bands. The spectra of the resulting SmE phase demonstrate long range in-plane orientational order of the cores. Finally, the optical axes and the layer orientation are the same of the starting crystal phase.

Based on these findings, we are able to propose the following mechanism. As described in Section 6.3.2, the phase transition involves the interpenetration of the layers, driven by the soft phonon. Such phonon, having $B_g$ symmetry, maintains the inversion center of the cell, pairing two molecules with antiparallel alignment and parallel cores. But it is known that in SmE phases the cores assume a herringbone arrangement [97]. Moreover, the displacements associated with the soft mode would yield a bilayer structure again, instead of a monolayer one.

These issues can be solved introducing a rotation about the long molecular axes at the transition. Such rotation, induced by the $\pi$ interactions between the adjacent cores, can arrange them in a herringbone packing and could also explain the discontinuous evolution of the in-plane polarized spectra. In addition, such molecular rotation must be interlayer correlated to achieve a herringbone packing with the same core orientation of the starting crystal.

The proposed mechanism, involving the interpenetration of the layers driven by the soft mode followed by in-plane rearrangement of the cores, is consistent with the results found in previous works on Ph-BTBT-10. XRD measurements on oriented thin films demonstrated that the layers maintain the same orientation through the Crystal to SmE transition and herringbone packing is present in the SmE phase [86]. This ordered molecular arrangement in the SmE phase is fully consistent with the mechanism proposed above. Another study proposed a similar mechanism by Molecular Dynamics simulations: the first step of the transition was the interlayer translation of the molecules [88]. Furthermore, a vibration described by the corresponding molecular displacements would have $B_g$ symmetry, as the soft mode.

The present Raman investigation provides experimental evidence of this, through the direct observation of the soft mode anticipating the phase transition. Low frequency phonons with soft behavior close to transitions from crystal to smectic phases have already been reported [102, 103]. However, these works investigated polycrystalline materials, losing the directional information accessible using single crystals. In this study, the combination of polarized spectra measured on different crystal planes allowed us to observe the soft mode selectively, together with its directionality and symmetry, and thus suggest a likely description for the involved molecular displacements.

# Appendix 1

## A.1 N-TMB-TCNQF$_4$ and TMB-TCNQF$_4$

To better understand the crystal packing of the two N,N,N',N'-Tetramethylbenzidine-TCNQF$_4$ (N-TMB-TCNQF$_4$) polymorphs, their polarized IR and Raman spectra were compared with the corresponding spectra of the ionic analogue 3,3',5,5'-Tetramethylbenzidine-TCNQF$_4$ (TMB-TCNQF$_4$), whose structure is known [62]. The ionicity is similar ($\simeq$0.9) in the three compounds, since the two donors, TMB and N-TMB, have similar ionization potential [66]. The charge sensitive bands of the common acceptor TCNQF$_4$ occur at almost the same frequencies (Fig A.1).

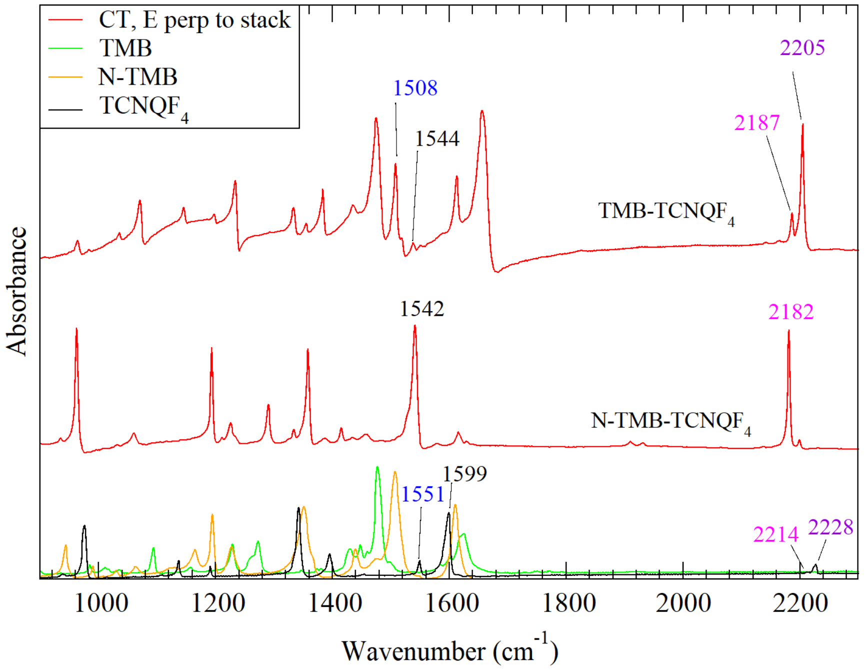

Figure A.1: *Comparison between the IR spectra of TMB-TCNQF$_4$ and N-TMB-TCNQF$_4$ (Phase II) polarized perpendicular to the stack direction. The TCNQF$_4$ charge sensitive bands are marked with different colors. Their different relative intensities in the two crystals are an orientational effect. The spectra of the pure reagents are also reported for clarity.*

In TMB-TCNQF$_4$ all the long molecular axes are parallel to the $b$ direction, as shown in Fig A.2, panels a) and b). For this reason, the orientation of the long molecular axes respect to the crystal faces can be easily recognized based on the resonance enhancement of the Raman spectra in the 900-1700 cm$^{-1}$ range (Fig A.3). Indeed, the 633 nm excitation matches an electronic absorption band of the donor and is close to the acceptor bands (Fig A.4), Ref [54]. The lowest energy absorptions of the two radical ions are long axis polarized. In the case of the crystal shown in Fig A.2, the maximum and the minimum Raman intensity are found with the light polarized along the two diagonals of the hollow section in panel d), that are therefore assigned to the $b$ and $c$ axes respectively.

The same holds also for both N-TMB-TCNQF$_4$ polymorphs, as the N-TMB$^+$ has the same electronic structure of TMB$^+$. Indeed, the Raman spectra of both phases are strongly enhanced when the exciting and scattered light are polarized along a specific direction, as shown in Fig 3.15. This demonstrates that the long molecular axes are aligned with such direction.

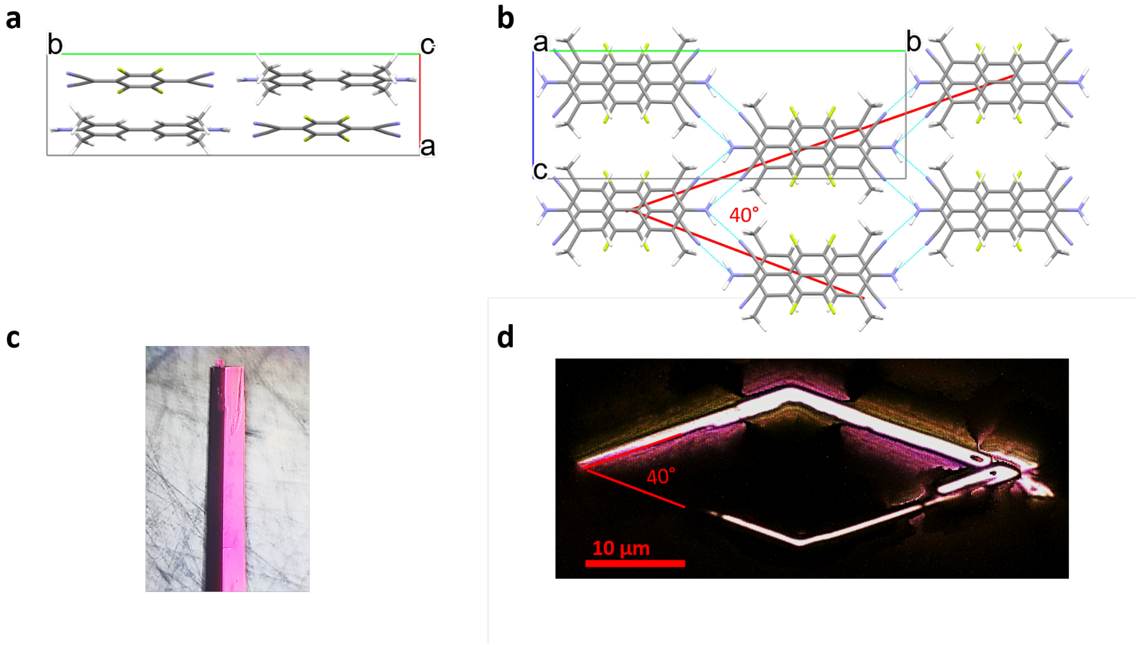

Figure A.2: *TMB-TCNQF$_4$ crystal packing, viewed perpendicular to the ab (a) and bc (b) planes. The microscopic images of a crystal viewed along the same directions are shown in c) and d). The crystal structure is reported from Ref [62]. The needle-like crystals are frequently hollow, as shown in (d). Their sides extend along the* 011 *and* $01\bar{1}$ *directions, following the H bond chain.*

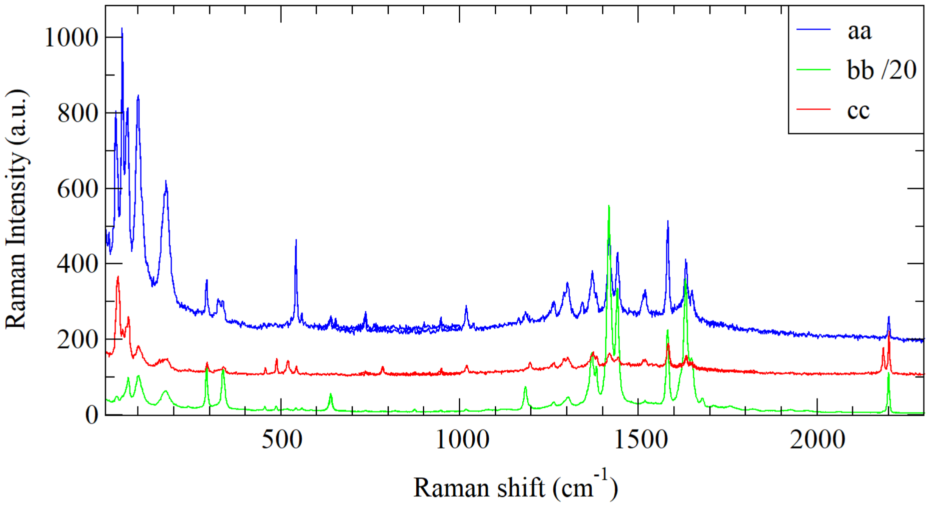

Figure A.3: *Polarized extended Raman spectra of TMB-TCNQF$_4$. For the sake of clarity, the three polarizations are offset and the bb one, enhanced by resonance, has been divided by 20.*

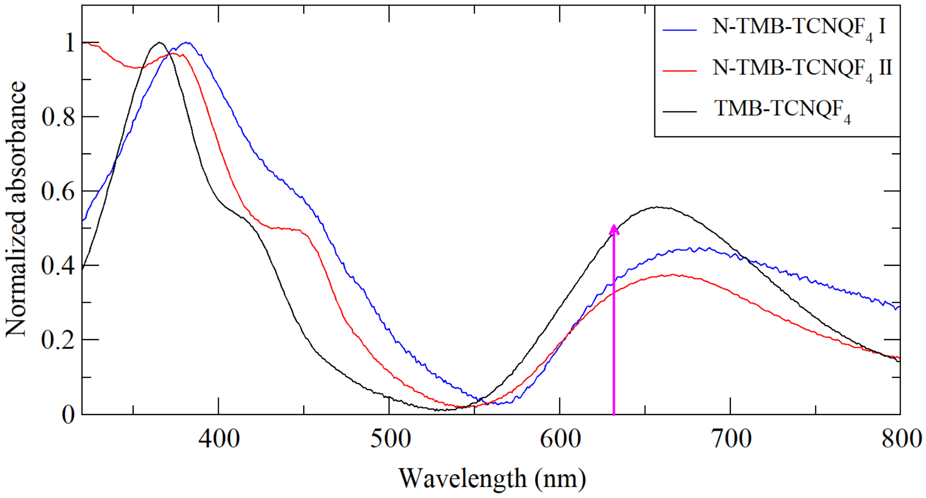

Figure A.4: *Comparison between the visible absorption spectra of the two N-TMB-TCNQF$_4$ polymorphs and of TMB-TCNQF$_4$. The spectra were measured on thin films. The 633 nm exciting line used for the Raman measurements is marked.*

# Appendix 2

## B.1 BTBT Raman spectra

The polarized Raman spectra of a BTBT single crystal were recorded to help in the interpretation of the low frequency spectra of Ph-BTBT-10. Since the two molecules arrange in similar crystal structures, the spectra were measured following the same approach.

Due to the $\pi$-interactions between the molecules, BTBT also crystallizes in a layered structure with an in-plane herringbone arrangement (CCDC refcode PODKEA, space group $P2_1/c$). The layers are parallel to the $bc$ plane, nearly perpendicular to the long molecular axis (Fig B.1). Indeed, the interlayer polarized extended spectra (Fig B.2) are an order of magnitude more intense than the in-plane polarized ones, as in the case of Ph-BTBT-10.

While the asymmetric Ph-BTBT-10 crystallizes in a unit cell with Z=4, the BTBT unit cell has Z=2, with the two molecules located on the inversion centers. Thus, in BTBT the only active Raman phonons are the 6 librations of gerade symmetry, being the translations all of ungerade symmetry and not active. The BTBT spectra were therefore useful to distinguish rotational and translational phonons in the more complex Ph-BTBT-10 spectra.

The BTBT low frequency Raman spectra are shown in Fig B.3. The low frequency modes, found at 45 $\text{cm}^{-1}$ and the weak band at 62 $\text{cm}^{-1}$ , have the same intensity in the in-plane and out-of-plane polarized spectra, while the higher frequency mode, occuring at 85 $\text{cm}^{-1}$ is completely in-plane polarized. According to the calculations reported in Ref [104], the latter vibration corresponds to the rotation about the long axis of the molecule, and the lowest frequency modes are assigned to rotations about the axis perpendicular to the molecular plane.

Thus, the Ph-BTBT-10 low-frequency phonons, occuring below 30 $\text{cm}^{-1}$ , completely interlayer polarized, can be safely assigned to translations along the long axis or wagging of the decyl chains. Furthermore, the in-plane polarized modes around 90-100 $\text{cm}^{-1}$ correspond to rotations about the long axes.

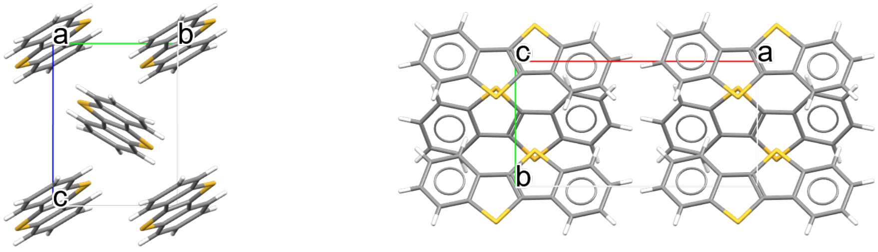

Figure B.1: *BTBT unit cell, view perpendicular to the bc (left) and ab (right) planes.*

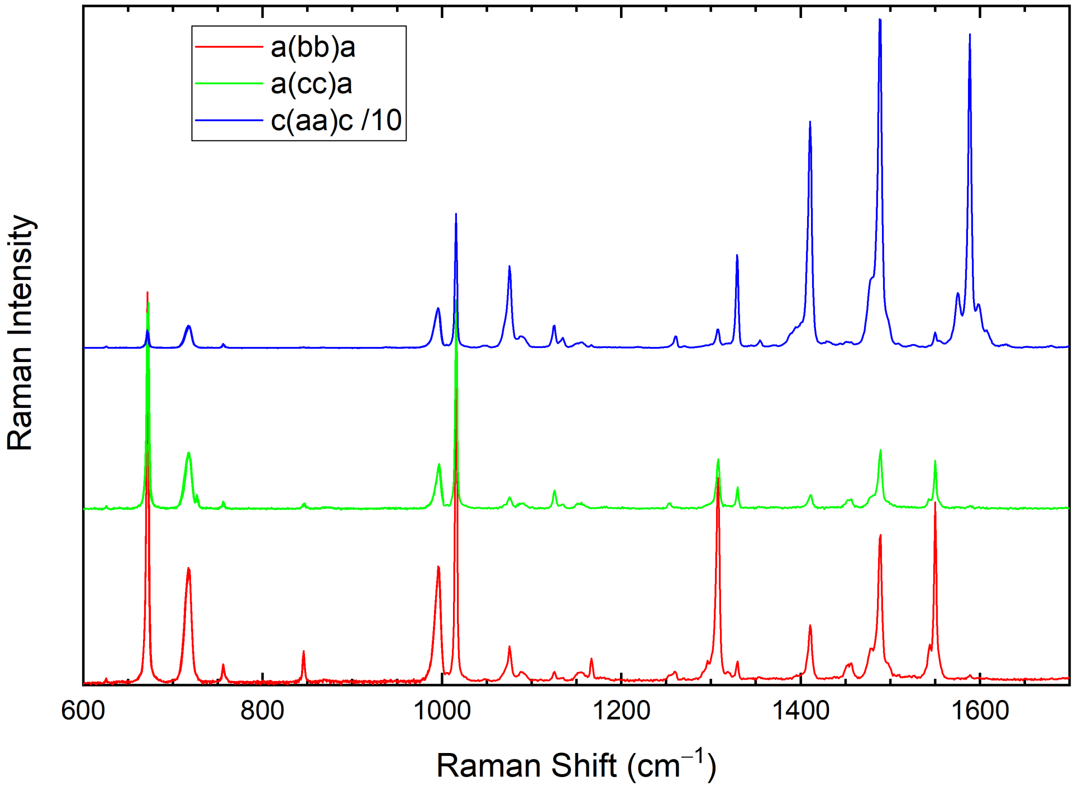

Figure B.2: *Polarized extended Raman spectra of a BTBT single crystal.*

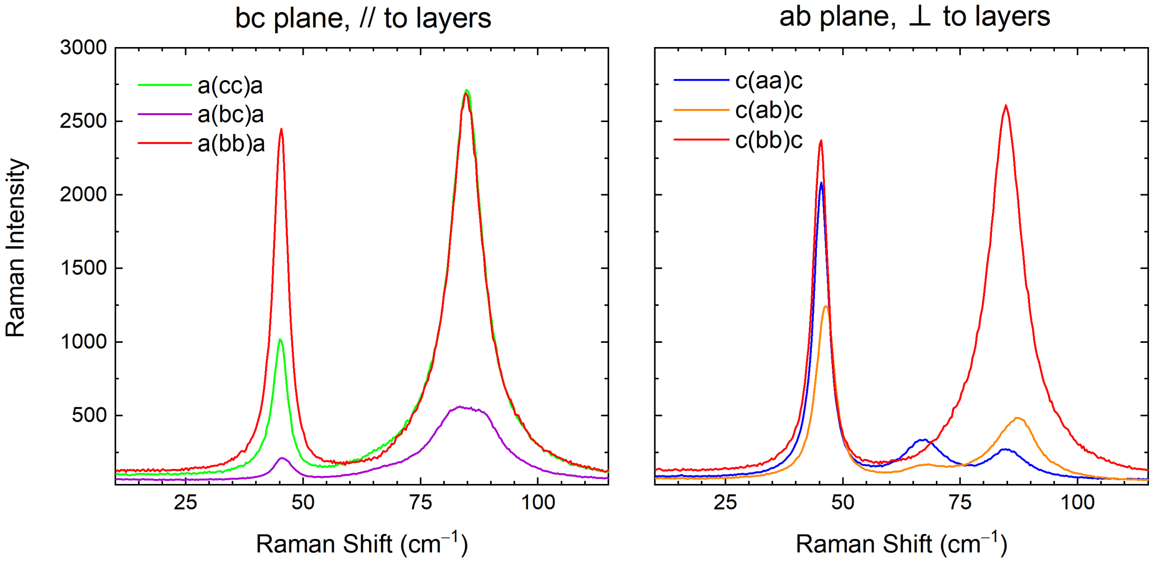

Figure B.3: *Polarized low frequency Raman spectra of a BTBT single crystal, measured on the bc and ac planes.*

# Conclusions

The present Thesis is dedicated to the spectroscopic study of molecular crystals and their phase transitions induced by temperature or pressure. IR and Raman spectroscopies were widely exploited to achieve both relevant microscopic parameters and structural information.

Spectroscopy became also a structural tool when measuring with polarized light on single crystals with known orientation. For instance, it was possible to find the crystallographic orientation relationship between the lattices of the two phases following a phase transition, to understand the mechanism. Another important achievement was the directionality assignment to the lattice phonons, aimed at recognizing lattice dynamics occurring along specific directions. The latter issue is rarely investigated in molecular materials, for two reasons. Firstly, the lattice phonons occur in the THz frequency range, located very close to the laser line in Raman measurements. Secondly, organic crystals usually present very anisotropic morphologies and are often very small.

These difficulties were overcome thanks to the Raman microspectrometer recently acquired in our laboratory, that made accessible lattice phonons at very low frequencies with high spectral resolution. In addition, the high magnification objectives gave the spatial resolution required to characterize micron sized crystals with any orientation, even on the thinnest faces.

The first part of the work dealt with the growth and the spectroscopic characterization of charge transfer cocrystals, containing electron donor and acceptor molecules. Firstly, we expanded the widely studied TTF-haloquinone series with two newly synthesized fluoranil based crystals, TTF-FA and DMTTF-FA (Chapters 1 and 2). Thanks to a rapid growth method, we obtained these two materials as single crystals, avoiding the side reactions that have prevented the characterization of these sistems so far. Both CT systems are neutral and their stack motif is mixed and regular.

TTF-FA undergoes a strongly first order Neutral to Ionic phase Transition, induced by both low temperature and high pressure. Despite the extensive crystal cracking at the transition we were able to resolve the low temperature structure, having two dimerized stacks arranged antiferroelectrically in a doubled unit cell. The spectra proved the high pressure phase to be the same ionic phase observed at low temperature.

Also DMTTF-FA displays a similar first order phase transition. Unexpectedly, the transition does not occur at low temperature despite the low critical pressure. The most likely explanation is that the transition involves a high activation barrier that cannot be overcome at low temperature. Furthermore, XRD analysis found structural disorder, probably due to the inclusion of a different DMTTF isomer, very hard to remove from the reagent used for the synthesis. Whether the DMTTF-FA behavior is intrinsic or due to disorder is still an open issue.

In Chapter 3 we explored another well known CT crystal family, whose constituents are chemically modified benzidine and TCNQ molecules. This work was aimed at understanding the effects of chemical substitution on the crystal packing and the relevant microscopic parameters. Surprisingly, in the case of N-TMB-TCNQF$_4$ we found two polymorph phases, both ionic and sharing many spectral features. Although the XRD analysis is still in progress, a detailed analysis of the spectra indicates that their stack motifs are both dimerized, but one is mixed and the other segregated. Chapter 4 deals with a close CT system, TMPD-TCNQ, that presents inconsistent structural and spectroscopic data. The present spectroscopic investigation on single crystals extended the previous study on powders. The combination between the temperature evolution of different vibrational spectra suggests an increase of the stack dimerization amplitude on lowering temperature, but without establishing long range 3D order.

The second part of the work was dedicated to single component molecular semiconductor crystals presenting polymorphism or phase transitions. The first one, presented in Chapter 5 is PCBM, a fullerene derivative widely used as an electron acceptor in organic photovoltaics. However, many polymorph and solvate PCBM phases have been reported and the crystal packing strongly impacts the charge carrier mobility. Our purpose was the characterization of the crystal phases that could be grown from solution deposition on different substrates. Among the three phases found, two were identified. The third phase is likely a new polymorph, as its features do not match any known PCBM phase. Interestingly, the IR spectra suggest that it does not include solvent molecules and might therefore show improved charge transport properties.

Chapter 6 is a detailed spectroscopic study of the bilayer crystal to monolayer Smectic E phase transition of the molecular semiconductor Ph-BTBT-10. The transition mechanism is currently under investigation as the ordered liquid crystal phase is thought to be a precursor of the crystal phase during the deposition of ordered thin films. The present work was focused on the lattice dynamics anticipating the transition and on the 3D order in the resulting Smectic E phase. Polarized THz Raman measurements on oriented single crystals detected an interlayer polarized soft phonon anticipating the first order transition. We thus proposed that the transition is firstly driven by the soft mode through interpenetration of adjacent layers, followed by a discontinuous in-plane rearrangement of the cores. A similar approach could also be extended to other organic semiconductors with a layered 2D structure to probe selectively the low frequency interlayer translational phonons, that have a crucial effect on the carrier mobility.

# Acknowledgements

As a premise, I think that only having been able to dedicate myself to research allowed me to overcome such a difficult historical moment. I am proud that science made it possible to see the light again.

First of all, I feel deeply grateful to my supervisor Prof Matteo Masino for sharing with me his knowledge and teaching me the spectroscopic techniques, giving me the tools and the freedom to design and perform a variety of experiments. I thank him for the patience and willingness shown while training me and discussing the results for a long time.

I also thank Prof Alberto Girlando and Prof Anna Painelli for the fruitful discussions inspiring new ideas that enriched the work, especially from the theoretical point of view.

I thank the whole Physical Chemistry research group of the University of Parma for the friendly company and the continuous cooperation on different research topics.

I thank Dr Lorenzo Pandolfi, Dr Tommaso Salzillo, Prof Elisabetta Venuti and the group of Prof Yves H. Geerts for the nice collaboration on liquid crystals, that captured my interest, driving my curiosity towards a topic that had been completely unknown to me before.

I thank Prof Francesco Mezzadri for the XRD structure determination of the charge transfer crystals synthesized in this thesis work, that was sometimes a challenging task.

I thank Prof Franco Cacialli for providing the PCBM crystals.

My deepest gratitude goes to my family and friends, especially Aurora and Nicola, for the constant encouragement and help while facing difficult moments. Last but not least, I thank my parents for imparting to me the passion for science.

# Bibliography

[1] J. Ferraris, D. Cowan, V. t. Walatka, and J. Perlstein, “Electron transfer in a new highly conducting donor-acceptor complex,” *Journal of the American Chemical Society*, vol. 95, no. 3, pp. 948–949, 1973.

[2] J. J. Mayerle, J. B. Torrance, and J. I. Crowley, “Mixed-stack complexes of tetrathiafulvalene. The structures of the charge-transfer complexes of TTF with chloranil and fluoranil,” *Acta Crystallographica Section B*, vol. 35, pp. 2988–2995, Dec 1979.

[3] J. B. Torrance, J. E. Vazquez, J. J. Mayerle, and V. Y. Lee, “Discovery of a Neutral-to-Ionic Phase Transition in Organic Materials,” *Phys. Rev. Lett.*, vol. 46, no. 4, pp. 253–257, 1981.

[4] J. Torrance, A. Girlando, J. Mayerle, J. Crowley, V. Lee, P. Batail, and S. LaPlaca, “Anomalous nature of neutral-to-ionic phase transition in tetrathiafulvalene-chloranil,” *Phys. Rev. Lett.*, vol. 47, pp. 1747–1750, 1981.

[5] M. Masino, N. Castagnetti, and A. Girlando, “Phenomenology of the Neutral-Ionic Valence Instability in Mixed Stack Charge-Transfer Crystals,” *Crystals*, vol. 7, no. 4, 2017.

[6] A. Painelli and A. Girlando, “Zero-temperature phase diagram of mixed-stack charge-transfer crystals,” *Phys. Rev. B*, vol. 37, pp. 5748–5760, Apr 1988.

[7] A. Girlando and A. Painelli, “Regular-dimerized stack and neutral-ionic interfaces in mixed-stack organic charge-transfer crystals,” *Phys. Rev. B*, vol. 34, pp. 2131–2139, Aug 1986.

[8] K. Kobayashi, S. Horiuchi, R. Kumai, F. Kagawa, Y. Murakami, and Y. Tokura, “Electronic Ferroelectricity in a Molecular Crystal with Large Polarization Directing Antiparallel to Ionic Displacement,” *Physical Review Letters*, vol. 108, pp. 1–5, jun 2012.

[9] S. Koshihara, Y. Tokura, T. Mitani, G. Saito, and T. Koda, “Photoinduced valence instability in the organic molecular compound tetrathiafulvalene-p-chloranil (TTF-CA),” *Phys. Rev. B*, vol. 42, pp. 6853–6856, Oct 1990.

[10] S.-y. Koshihara, Y. Takahashi, H. Sakai, Y. Tokura, and T. Luty, "Photoinduced Cooperative Charge Transfer in Low-Dimensional Organic Crystals," *The Journal of Physical Chemistry B*, vol. 103, no. 14, pp. 2592–2600, 1999.

[11] E. Collet, M.-H. Lemée-Cailleau, M. B.-L. Cointe, H. Cailleau, M. Wulff, T. Luty, S.-Y. Koshihara, M. Meyer, L. Toupet, P. Rabiller, and S. Techert, "Laser-Induced Ferroelectric Structural Order in an Organic Charge-Transfer Crystal," *Science*, vol. 300, no. 5619, pp. 612–615, 2003.

[12] T. Mitani, G. Saito, Y. Tokura, and T. Koda, "Soliton Formation at the Neutral-to-Ionic Phase Transition in the Mixed-Stack Charge-Transfer Crystal Tetrathiafulvalene -*p*- Chloranil," *Phys. Rev. Lett.*, vol. 53, pp. 842–845, Aug 1984.

[13] T. Mitani, Y. Kaneko, S. Tanuma, Y. Tokura, T. Koda, and G. Saito, "Electric conductivity and phase diagram of a mixed-stack charge-transfer crystal: Tetrathiafulvalene-p-chloranil," *Phys. Rev. B*, vol. 35, pp. 427–429, Jan 1987.

[14] H. Okamoto, T. Mitani, Y. Tokura, S. Koshihara, T. Komatsu, Y. Iwasa, T. Koda, and G. Saito, "Anomalous dielectric response in tetrathiafulvalene-p-chloranil as observed in temperature- and pressure-induced neutral-to-ionic phase transition," *Phys. Rev. B*, vol. 43, pp. 8224–8232, Apr 1991.

[15] M. Masino, A. Girlando, and Z. G. Soos, "Evidence for a soft mode in the temperature induced neutral-ionic transition of TTF-CA," *Chemical Physics Letters*, vol. 369, no. 3, pp. 428–433, 2003.

[16] A. Girlando, M. Masino, A. Painelli, N. Drichko, M. Dressel, A. Brillante, R. G. Della Valle, and E. Venuti, "Direct evidence of overdamped Peierls-coupled modes in the temperature-induced phase transition in tetrathiafulvalene-chloranil," *Phys. Rev. B*, vol. 78, p. 045103, Jul 2008.

[17] S. Horiuchi, Y. Okimoto, R. Kumai, and Y. Tokura, "Quantum Phase Transition in Organic Charge-Transfer Complexes," *Science*, vol. 299, no. 5604, pp. 229–232, 2003.

[18] F. Kagawa, S. Horiuchi, and Y. Tokura, "Quantum Phenomena Emerging Near a Ferroelectric Critical Point in a Donor–Acceptor Organic Charge-Transfer Complex," *Crystals*, vol. 7, no. 4, 2017.

[19] A. Girlando and A. Painelli, "Regular-dimerized stack vs neutral-ionic instability in mixed stack CT crystals," *Physica B+ C*, vol. 143, no. 1-3, pp. 559–561, 1986.

[20] P. Ranzieri, M. Masino, A. Girlando, and M.-H. Lemée-Cailleau, "Temperature-induced valence and structural instability in DMTTF-CA: Single-crystal Raman and infrared measurements," *Phys. Rev. B*, vol. 76, p. 134115, Oct 2007.

[21] F. Delchiaro, A. Girlando, A. Painelli, A. Bandyopadhyay, S. K. Pati, and G. D'Avino, "Towards first-principles prediction of valence instabilities in mixed stack charge-transfer crystals," *Phys. Rev. B*, vol. 95, p. 155125, Apr 2017.

[22] A. Girlando, I. Zanon, R. Bozio, and C. Pecile, "Raman and infrared frequency shifts proceeding from ionization of perhalo-p-benzoquinones to radical anions," *The Journal of Chemical Physics*, vol. 68, no. 1, pp. 22–31, 1978.

[23] P. Ranzieri, M. Masino, and A. Girlando, "Charge-Sensitive Vibrations in p-Chloranil: The Strange Case of the CC Antisymmetric Stretching," *The Journal of Physical Chemistry B*, vol. 111, no. 44, pp. 12844–12848, 2007.

[24] A. Girlando, F. Marzola, C. Pecile, and J. B. Torrance, "Vibrational spectroscopy of mixed stack organic semiconductors: Neutral and ionic phases of tetrathiafulvalene-chloranil (TTF-CA) charge transfer complex," *The Journal of Chemical Physics*, vol. 79, no. 2, pp. 1075–1085, 1983.

[25] A. Girlando, R. Bozio, C. Pecile, and J. B. Torrance, "Discovery of vibronic effects in the Raman spectra of mixed-stack charge-transfer crystals," *Phys. Rev. B*, vol. 26, pp. 2306–2309, Aug 1982.

[26] A. Painelli and A. Girlando, "Electron–molecular vibration (e–mv) coupling in charge-transfer compounds and its consequences on the optical spectra: A theoretical framework," *The Journal of Chemical Physics*, vol. 84, no. 10, pp. 5655–5671, 1986.

[27] C. Pecile, A. Palnelli, and A. Girlando, "Studies of organic semiconductors for 40 years—V," *Molecular Crystals and Liquid Crystals*, vol. 171, no. 1, pp. 69–87, 1989.

[28] S. Horiuchi, Y. Okimoto, R. Kumai, and Y. Tokura, "Ferroelectric Valence Transition and Phase Diagram of a Series of Charge-Transfer Complexes of 4,4'-Dimethyltetrathiafulvalene and Tetrahalo-p-benzoquinones," *Journal of the American Chemical Society*, vol. 123, no. 4, pp. 665–670, 2001.

[29] S. Horiuchi, R. Kumai, Y. Okimoto, and Y. Tokura, "Chemical approach to neutral-ionic valence instability, quantum phase transition, and relaxor ferroelectricity in organic charge-transfer complexes," *Chemical Physics*, vol. 325, pp. 78–91, 06 2006.

[30] E. Ferrari, F. Mezzadri, and M. Masino, "Temperature-induced neutral-to-ionic phase transition of the charge-transfer crystal tetrathiafulvalene-fluoranil," *Physical Review B*, vol. 105, no. 5, p. 054106, 2022.

[31] G. M. Sheldrick, "Crystal structure refinement with *SHELXL*," *Acta Crystallographica Section C*, vol. 71, pp. 3–8, Jan 2015.

[32] Bruker, *APEX2, SAINT and SADABS.* Bruker AXS Inc., Madison, Wisconsin, USA, 2008.

[33] H. Mao, J.-A. Xu, and P. Bell, “Calibration of the ruby pressure gauge to 800 kbar under quasi-hydrostatic conditions,” *Journal of Geophysical Research: Solid Earth*, vol. 91, no. B5, pp. 4673–4676, 1986.

[34] M. J. Frisch, G. W. Trucks, H. B. Schlegel, G. E. Scuseria, M. A. Robb, J. R. Cheeseman, G. Scalmani, V. Barone, G. A. Petersson, H. Nakatsuji, X. Li, M. Caricato, A. V. Marenich, J. Bloino, B. G. Janesko, R. Gomperts, B. Mennucci, H. P. Hratchian, J. V. Ortiz, A. F. Izmaylov, J. L. Sonnenberg, D. Williams-Young, F. Ding, F. Lipparini, F. Egidi, J. Goings, B. Peng, A. Petrone, T. Henderson, D. Ranasinghe, V. G. Zakrzewski, J. Gao, N. Rega, G. Zheng, W. Liang, M. Hada, M. Ehara, K. Toyota, R. Fukuda, J. Hasegawa, M. Ishida, T. Nakajima, Y. Honda, O. Kitao, H. Nakai, T. Vreven, K. Throssell, J. A. Montgomery, Jr., J. E. Peralta, F. Ogliaro, M. J. Bearpark, J. J. Heyd, E. N. Brothers, K. N. Kudin, V. N. Staroverov, T. A. Keith, R. Kobayashi, J. Normand, K. Raghavachari, A. P. Rendell, J. C. Burant, S. S. Iyengar, J. Tomasi, M. Cossi, J. M. Millam, M. Klene, C. Adamo, R. Cammi, J. W. Ochterski, R. L. Martin, K. Morokuma, O. Farkas, J. B. Foresman, and D. J. Fox, “Gaussian˜16 Revision C.01,” 2016. Gaussian Inc. Wallingford CT.

[35] J. P. Merrick, D. Moran, and L. Radom, “An Evaluation of Harmonic Vibrational Frequency Scale Factors,” *The Journal of Physical Chemistry A*, vol. 111, no. 45, pp. 11683–11700, 2007.

[36] M. B.-L. Cointe, M. H. Lemée-Cailleau, H. Cailleau, B. Toudic, A. Moréac, F. Moussa, C. Ayache, and N. Karl, “Thermal hysteresis phenomena and mesoscopic phase coexistence around the neutral-ionic phase transition in TTF-CA and TMB-TCNQ,” *Phys. Rev. B*, vol. 68, p. 064103, Aug 2003.

[37] A. Girlando and C. Pecile, “Vibrational spectra of fluoranil. (2, 3, 5, 6-Tetrafluoro-p-benzoquinone),” *J. Chem. Soc., Faraday Trans. 2*, vol. 71, pp. 689–698, 1975.

[38] R. Bozio, I. Zanon, A. Girlando, and C. Pecile, “Vibrational spectroscopy of molecular constituents of one-dimensional organic conductors. Tetrathiofulvalene (TTF), TTF+, and (TTF+)2 dimer,” *The Journal of Chemical Physics*, vol. 71, no. 5, pp. 2282–2293, 1979.

[39] F. Mezzadri, N. Castagnetti, M. Masino, and A. Girlando, “Solvated and ferroelectric phases of the charge transfer co-crystal tmb-tcnq,” *Crystal Growth & Design*, vol. 18, no. 9, pp. 5592–5599, 2018.

[40] M. Le Cointe, M. H. Lemée-Cailleau, H. Cailleau, B. Toudic, L. Toupet, G. Heger, F. Moussa, P. Schweiss, K. H. Kraft, and N. Karl, “Symmetry breaking and structural changes at the neutral-to-ionic transition in tetrathiafulvalene-p-chloranil,” *Phys. Rev. B*, vol. 51, pp. 3374–3386, Feb 1995.

[41] G. D'Avino and M. J. Verstraete, "Are Hydrogen-Bonded Charge Transfer Crystals Room Temperature Ferroelectrics?," *Phys. Rev. Lett.*, vol. 113, p. 237602, Dec 2014.

[42] G. D'Avino, A. Painelli, and Z. G. Soos, "Modeling the Neutral-Ionic Transition with Correlated Electrons Coupled to Soft Lattices and Molecules," *Crystals*, vol. 7, no. 5, 2017.

[43] H. Nakayama, S. Yajima, T. Yoshida, and K. Ishii, "Relaxational Molecular Motions in Simple Organic Liquids: Studies with Low-Wavenumber Depolarized Raman Spectroscopy," *Journal of Raman Spectroscopy*, vol. 28, no. 1, pp. 15–22, 1997.

[44] M. Kaźmierczak, E. Patyk-Kaźmierczak, and A. Katrusiak, "Compression and Thermal Expansion in Organic and Metal–Organic Crystals: The Pressure–Temperature Correspondence Rule," *Crystal Growth & Design*, vol. 21, no. 4, pp. 2196–2204, 2021.

[45] K. Sunami, F. Iwase, K. Miyagawa, S. Horiuchi, K. Kobayashi, R. Kumai, and K. Kanoda, "Variation in the nature of the neutral-ionic transition in DMTTF-QCl 4 under pressure probed by NQR and NMR," *Physical Review B*, vol. 99, no. 12, p. 125133, 2019.

[46] N. Castagnetti, M. Masino, C. Rizzoli, A. Girlando, and C. Rovira, "Mixed stack charge transfer crystals: Crossing the neutral-ionic borderline by chemical substitution," *Phys. Rev. Materials*, vol. 2, p. 024602, Feb 2018.

[47] N. Castagnetti, "Organic Molecular Materials: Crystal Growth and Spectroscopic Characterization," 2018.

[48] R. Bozio, I. Zanon, A. Girlando, and C. Pecile, "Influence of the intermolecular charge transfer interaction on the solution and solid state infrared spectra of 7, 7, 8, 8-tetracyanoquinodimethane (TCNQ) alkaline salts," *Journal of the Chemical Society, Faraday Transactions 2: Molecular and Chemical Physics*, vol. 74, pp. 235–248, 1978.

[49] M. Meneghetti and C. Pecile, "Charge–transfer organic crystals: Molecular vibrations and spectroscopic effects of electron–molecular vibration coupling of the strong electron acceptor TCNQF4," *The Journal of chemical physics*, vol. 84, no. 8, pp. 4149–4162, 1986.

[50] N. Castagnetti, G. Kociok-Köhn, E. D. Como, and A. Girlando, "Temperature-induced valence instability in the charge-transfer crystal TMB-TCNQ," *Physical Review B*, vol. 95, jan 2017.

[51] Y. Iwasa, T. Koda, Y. Tokura, A. Kobayashi, N. Iwasawa, and G. Saito, "Temperature-induced neutral-ionic transition in tetramethylbenzidine-tetracyanoquinodimethane (TMB-TCNQ)," *Physical Review B*, vol. 42, no. 4, p. 2374, 1990.

[52] T. Salzillo, M. Masino, G. Kociok-Kohn, D. Di Nuzzo, E. Venuti, R. G. Della Valle, D. Vanossi, C. Fontanesi, A. Girlando, A. Brillante, *et al.*, "Structure, stoichiometry, and charge transfer in cocrystals of Perylene with TCNQ-Fx," *Crystal Growth & Design*, vol. 16, no. 5, pp. 3028–3036, 2016.

[53] S. A. Bewick, R. A. Pascal, D. M. Ho, Z. G. Soos, M. Masino, and A. Girlando, "Disorder in organic charge-transfer single crystals: Dipolar disorder in ClMePD-DMeDCNQI," *Journal of Chemical Physics*, vol. 122, no. 2, pp. 1–8, 2005.

[54] J. Torrance, J. Mayerle, K. Bechgaard, B. Silverman, and Y. Tomkiewicz, "Comparison of two isostructural organic compounds, one metallic and the other insulating," *Physical Review B*, vol. 22, no. 10, p. 4960, 1980.

[55] M. Meneghetti, R. Bozio, C. Bellitto, and C. Pecile, "Electronic and structural characterization of a charge transfer crystal with strong electronic correlations through infrared and Raman spectroscopy: TMPD–TCNQF4," *The Journal of Chemical Physics*, vol. 89, no. 5, pp. 2704–2711, 1988.

[56] T. J. Kistenmacher, T. J. Emge, A. Bloch, and D. Cowan, "Structure of the red, semiconducting form of 4, 4', 5, 5'-tetramethyl-Δ2, 2'-bi-1, 3-diselenole-7, 7, 8, 8-tetracyano-p-quinodimethane, TMTSF-TCNQ," *Acta Crystallographica Section B: Structural Crystallography and Crystal Chemistry*, vol. 38, no. 4, pp. 1193–1199, 1982.

[57] K. Bechgaard, T. J. Kistenmacher, A. N. Bloch, and D. O. Cowan, "The crystal and molecular structure of an organic conductor from 4, 4', 5, 5'-tetramethyl-Δ2, 2'-bis-1, 3-diselenole and 7, 7, 8, 8-tetracyano-p-quinodimethane [TMTSF-TCNQ]," *Acta Crystallographica Section B: Structural Crystallography and Crystal Chemistry*, vol. 33, no. 2, pp. 417–422, 1977.

[58] T. Mori and H. Inokuchi, "Crystal structure of the mixed-stacked salt of bis (ethylenedithio) tetrathiafulvalene (BEDT-TTF) and tetracyanoquinodimethane (TCNQ)," *Bulletin of the Chemical Society of Japan*, vol. 60, no. 1, pp. 402–404, 1987.

[59] H. M. Yamamoto, M. Hagiwara, and R. Kato, "New phase of (BEDT-TTF)(TCNQ)," *Synthetic metals*, vol. 133, pp. 449–451, 2003.

[60] S. H. Lapidus, A. Naik, A. Wixtrom, N. E. Massa, V. Ta Phuoc, L. del Campo, S. Lebègue, J. G. Angyàn, T. Abdel-Fattah, and S. Pagola, "The black polymorph of TTF-CA: TTF polymorphism and solvent effects in mechanochemical and vapor digestion syntheses, FT-IR, crystal packing, and electronic structure," *Crystal growth & design*, vol. 14, no. 1, pp. 91–100, 2014.

[61] A. Girlando, A. Painelli, and C. Pecile, "Molecular Vibration Analysis of Ionicity and Phase Transition in TMPD-TCNQ (1:1) Charge Transfer Salt," *Molecular Crystals and Liquid Crystals*, vol. 112, pp. 325–343, dec 1984.

[62] S. Canossa, E. Ferrari, P. Sippel, J. K. Fischer, R. Pfattner, R. Frison, M. Masino, M. Mas-Torrent, P. Lunkenheimer, C. Rovira, *et al.*, "Tetramethylbenzidine-tetrafluoroTCNQ (TMB-TCNQF4): a narrow-gap semiconducting salt with room-temperature relaxor ferroelectric behavior," *The Journal of Physical Chemistry C*, vol. 125, no. 46, pp. 25816–25824, 2021.

[63] A. Hanson, "The crystal structure of the 1:1 complex of 7, 7, 8, 8-tetracyanoquinodimethan, and N, N, N', N'-tetramethyl-p-phenylenediamine," *Acta Crystallographica*, vol. 19, no. 4, pp. 610–613, 1965.

[64] R. Somoano, V. Hadek, S. Yen, A. Rembaum, and R. Deck, "The synthesis and transport properties of the complex salt (TMPD)(TCNQ) 2," *The Journal of Chemical Physics*, vol. 62, no. 3, pp. 1061–1067, 1975.

[65] H. Kuroda, S. Hiroma, and H. Akamatu, "Polarized absorption spectra of single crystals of ion radical salts. I. Molecular compounds of 7, 7, 8, 8-Tetracyano-p-quinodimethane with N, N, N', N'-tetramethyl-p-phenylenediamine and N, N-dimethyl-p-phenylenediamine," *Bulletin of the Chemical Society of Japan*, vol. 41, no. 12, pp. 2855–2858, 1968.

[66] H. Awano, H. Murakami, T. Yamashita, H. Ohigashi, and T. Ogata, "Electrodeposition of the cationic radical salts of some aromatic diamines from acetonitrile solution," *Synthetic metals*, vol. 39, no. 3, pp. 327–341, 1991.

[67] M. Masino, A. Girlando, L. Farina, and A. Brillante, "A new type of neutral–ionic interface in mixed stack organic charge transfer crystals: Temperature induced ionicity change in ClMePD–DMeDCNQI," *Physical Chemistry Chemical Physics*, vol. 3, no. 10, pp. 1904–1910, 2001.

[68] S. Etemad and E. Ehrenfreund, "Delocalized Triplet Excitations in an Antiferromagnetically Coupled Uniform 1-D System," in *AIP Conference Proceedings*, pp. 1499–1503, American Institute of Physics, 1973.

[69] J. C. Hummelen, B. W. Knight, F. Le Peq, F. Wudl, J. Yao, and C. L. Wilkins, "Preparation and characterization of fulleroid and methanofullerene derivatives," *The Journal of Organic Chemistry*, vol. 60, no. 3, pp. 532–538, 1995.

[70] M. T. Rispens, A. Meetsma, R. Rittberger, C. J. Brabec, N. S. Sariciftci, and J. C. Hummelen, "Influence of the solvent on the crystal structure of PCBM and the efficiency of MDMO-PPV: PCBM 'plastic'solar cells," *Chemical Communications*, no. 17, pp. 2116–2118, 2003.

[71] M. Casalegno, S. Zanardi, F. Frigerio, R. Po, C. Carbonera, G. Marra, T. Nicolini, G. Raos, and S. V. Meille, "Solvent-free phenyl-C61-butyric acid methyl ester (PCBM) from clathrates: insights for organic photovoltaics from crystal structures and molecular dynamics," *Chemical communications*, vol. 49, no. 40, pp. 4525–4527, 2013.

[72] G. Paternò, A. J. Warren, J. Spencer, G. Evans, V. G. Sakai, J. Blumberger, and F. Cacialli, "Micro-focused X-ray diffraction characterization of high-quality [6, 6]-phenyl-C 61-butyric acid methyl ester single crystals without solvent impurities," *Journal of Materials Chemistry C*, vol. 1, no. 36, pp. 5619–5623, 2013.

[73] X. Zhao, T. Liu, X. Hou, Z. Liu, W. Shi, and T. J. S. Dennis, "[60] PCBM single crystals: remarkably enhanced band-like charge transport, broadband UV-visible-NIR photo-responsivity and improved long-term air-stability," *Journal of Materials Chemistry C*, vol. 6, no. 20, pp. 5489–5496, 2018.

[74] R. Dabirian, X. Feng, L. Ortolani, A. Liscio, V. Morandi, K. Müllen, P. Samorì, and V. Palermo, "Micron-sized [6, 6]-phenyl C61 butyric acid methyl ester crystals grown by dip coating in solvent vapour atmosphere: interfaces for organic photovoltaics," *Physical Chemistry Chemical Physics*, vol. 12, no. 17, pp. 4473–4480, 2010.

[75] L. Zheng and Y. Han, "Solvated crystals based on [6, 6]-phenyl-C61-butyric acid methyl ester (PCBM) with the hexagonal structure and their phase transformation," *The Journal of Physical Chemistry B*, vol. 116, no. 5, pp. 1598–1604, 2012.

[76] G. Tregnago, M. Wykes, G. M. Paternò, D. Beljonne, and F. Cacialli, "Low-temperature photoluminescence spectroscopy of solvent-free PCBM single-crystals," *The Journal of Physical Chemistry C*, vol. 119, no. 21, pp. 11846–11851, 2015.

[77] T. J. Savenije, J. E. Kroeze, M. M. Wienk, J. M. Kroon, and J. M. Warman, "Mobility and decay kinetics of charge carriers in photoexcited PCBM/PPV blends," *Physical Review B*, vol. 69, no. 15, p. 155205, 2004.

[78] S. Falke, P. Eravuchira, A. Materny, and C. Lienau, "Raman spectroscopic identification of fullerene inclusions in polymer/fullerene blends," *Journal of Raman Spectroscopy*, vol. 42, no. 10, pp. 1897–1900, 2011.

[79] F. Frigerio, M. Casalegno, C. Carbonera, T. Nicolini, S. V. Meille, and G. Raos, "Molecular dynamics simulations of the solvent-and thermal history-dependent structure of the PCBM fullerene derivative," *Journal of Materials Chemistry*, vol. 22, no. 12, pp. 5434–5443, 2012.

[80] B. W. Larson, J. B. Whitaker, A. A. Popov, N. Kopidakis, G. Rumbles, O. V. Boltalina, and S. H. Strauss, "Thermal [6, 6]→[6, 6] isomerization and decomposition of PCBM (phenyl-C61-butyric acid methyl ester)," *Chemistry of Materials*, vol. 26, no. 7, pp. 2361–2367, 2014.

[81] H. Iino, T. Usui, and J.-i. Hanna, "Liquid crystals for organic thin-film transistors," *Nature Communications*, vol. 6, p. 6828, Apr 2015.

[82] H. Iino and J.-i. Hanna, "Liquid crystalline thin films as a precursor for polycrystalline thin films aimed at field effect transistors," *Journal of Applied Physics*, vol. 109, no. 7, p. 074505, 2011.

[83] H. Iino, T. Kobori, and J.-i. Hanna, "Improved thermal stability in organic FET fabricated with a soluble BTBT derivative," *Journal of non-crystalline solids*, vol. 358, no. 17, pp. 2516–2519, 2012.

[84] J. W. Goodby, R. J. Mandle, E. J. Davis, T. Zhong, and S. J. Cowling, "What makes a liquid crystal? The effect of free volume on soft matter," *Liquid Crystals*, vol. 42, no. 5-6, pp. 593–622, 2015.

[85] H. Minemawari, J. Tsutsumi, S. Inoue, T. Yamada, R. Kumai, and T. Hasegawa, "Crystal structure of asymmetric organic semiconductor 7-Decyl-2-phenyl[1]benzothieno$[3, 2 - b]$[1]benzothiophene," *Applied Physics Express*, vol. 7, p. 091601, sep 2014.

[86] S. Hofer, W. Bodlos, J. Novák, A. Sanzone, L. Beverina, and R. Resel, "Molecular packing analysis of the crystal smectic E phase of a benzothienobenzothiophene derivative by a combined experimental / computational approach," *Liquid Crystals*, vol. 48, no. 13, pp. 1888–1896, 2021.

[87] H. Iino and J.-I. Hanna, "Liquid crystal and crystal structures of a phenylbenzothienobenzothiophene derivative," *Molecular Crystals and Liquid Crystals*, vol. 647, no. 1, pp. 37–43, 2017.

[88] M. Yoneya, "Monolayer Crystal Structure of the Organic Semiconductor 7-Decyl-2-phenyl[1]benzothieno$[3, 2-b]$[1]benzothiophene," *The Journal of Physical Chemistry C*, vol. 122, no. 39, pp. 22225–22231, 2018.

[89] M. Yoneya, "Monolayer crystal structure of the organic semiconductor 7-Decyl-2-phenyl[1]benzothieno$[3, 2-b]$[1]benzothiophene, revisited," *Japanese Journal of Applied Physics*, vol. 59, no. 9, p. 090909, 2020.

[90] H. Nakayama, Y. Minagawa, C. Abematsu, S. Yajima, and K. Ishii, "Pseudo-lattice vibrations in smectic phase of liquid crystals: studies on small wave number Raman spectra of 4-alkyl-4'-cyanobiphenyl," *Chemical Physics*, vol. 253, no. 2, pp. 331–337, 2000.

[91] N. Bedoya-Martínez, B. Schrode, A. O. F. Jones, T. Salzillo, C. Ruzié, N. Demitri, Y. H. Geerts, E. Venuti, R. G. Della Valle, E. Zojer, and R. Resel, "Dft-assisted polymorph identification from lattice raman fingerprinting," *The Journal of Physical Chemistry Letters*, vol. 8, no. 15, pp. 3690–3695, 2017. PMID: 28731723.

[92] G. Schweicher, G. d'Avino, M. T. Ruggiero, D. J. Harkin, K. Broch, D. Venkateshvaran, G. Liu, A. Richard, C. Ruzié, J. Armstrong, *et al.*, "Chasing the "killer" phonon mode for the rational design of low-disorder, high-mobility

molecular semiconductors," *Advanced Materials*, vol. 31, no. 43, p. 1902407, 2019.

[93] A. Baggioli, M. Casalegno, G. Raos, L. Muccioli, S. Orlandi, and C. Zannoni, "Atomistic Simulation of Phase Transitions and Charge Mobility for the Organic Semiconductor Ph-BTBT-C10," *Chemistry of Materials*, vol. 31, no. 17, pp. 7092–7103, 2019.

[94] B.-R. Hyun and E. L. Quitevis, "Low-frequency spectrum of homeotropically aligned liquid crystals: optical heterodyne-detected Raman-induced Kerr effect spectroscopy of 4-octyl-4'-cyanobiphenyl," *Chemical physics letters*, vol. 370, no. 5-6, pp. 725–732, 2003.

[95] S. Inoue, H. Minemawari, J. Tsutsumi, M. Chikamatsu, T. Yamada, S. Horiuchi, M. Tanaka, R. Kumai, M. Yoneya, and T. Hasegawa, "Effects of Substituted Alkyl Chain Length on Solution-Processable Layered Organic Semiconductor Crystals," *Chemistry of Materials*, vol. 27, pp. 3809–3812, Jun 2015.

[96] Y. Yamamura, T. Adachi, T. Miyazawa, K. Horiuchi, M. Sumita, M. Massalska-Arodź, S. Urban, and K. Saito, "Calorimetric and Spectroscopic Evidence of Chain-Melting in Smectic E and Smectic A Phases of 4-Alkyl-4'-isothiocyanatobiphenyl (nTCB)," *The Journal of Physical Chemistry B*, vol. 116, no. 30, pp. 9255–9260, 2012. PMID: 22765025.

[97] K. Saito, T. Miyazawa, A. Fujiwara, M. Hishida, H. Saitoh, M. Massalska-Arodź, and Y. Yamamura, "Reassessment of structure of smectic phases: Nano-segregation in smectic E phase in 4-n-alkyl-4'-isothiocyanato-1, 1'-biphenyls," *The journal of chemical physics*, vol. 139, no. 11, p. 114902, 2013.

[98] N. A. Vaz, M. J. Vaz, and J. W. Doane, "Molecular ordering and motion within the smectic-e phase: H 2 nmr study," *Physical Review A*, vol. 30, no. 2, p. 1008, 1984.

[99] M. Jasiurkowska, A. Budziak, J. Czub, M. Massalska-Arodź, and S. Urban, "X-ray studies on the crystalline E phase of the 4-n-alkyl-4'-isothiocyanatobiphenyl homologous series (nBT, n = 2–10)," *Liquid Crystals*, vol. 35, no. 4, pp. 513–518, 2008.

[100] M. Jasiurkowska, A. Budziak, J. Czub, and S. Urban, "Dielectric and X-ray studies of eleventh and twelfth members of two isothiocyanato mesogenic compounds," *ACTA PHYSICA POLONICA SERIES A*, vol. 110, no. 6, p. 795, 2006.

[101] S. Hofer, J. Unterkofler, M. Kaltenegger, G. Schweicher, C. Ruzié, A. Tamayo, T. Salzillo, M. Mas-Torrent, A. Sanzone, L. Beverina, Y. H. Geerts, and R. Resel, "Molecular Disorder in Crystalline Thin Films of an Asymmetric BTBT Derivative," *Chemistry of Materials*, vol. 33, no. 4, pp. 1455–1461, 2021. PMID: 33642680.

[102] D. Dvorjetski, V. Volterra, and E. Wiener-Avnear, “Raman study on several smectic phases in terephtal-bis-butylaniline (TBBA),” *Physical Review A*, vol. 12, no. 2, p. 681, 1975.

[103] N. M. Amer and Y. Shen, “Low frequency Raman mode in smectic liquid crystals near the phase transitions,” *Solid State Communications*, vol. 12, no. 4, pp. 263–265, 1973.

[104] A. Y. Sosorev, O. D. Parashchuk, N. V. Tukachev, D. R. Maslennikov, D. I. Dominskiy, O. V. Borshchev, M. S. Polinskaya, M. S. Skorotetcky, O. G. Kharlanov, and D. Y. Paraschuk, “Suppression of dynamic disorder by electrostatic interactions in structurally close organic semiconductors,” *Physical Chemistry Chemical Physics*, vol. 23, no. 29, pp. 15485–15491, 2021.